International Journal of Comprehensive Engineering

ISSN 2186-2680
Volume 2, Number 4, December 2013

IJCE

Published by
International Association of Comprehensive Engineering (IACE)

http://www.iace-journal.org/

IJCE

Printed by
Diagnosis Engineering & Technology Corp., Japan

========== International Journal of Comprehensive Engineering (IJCE) ==========

International Journal of Comprehensive Engineering (IJCE) is an international interdisciplinary journal that integrates publication from aspects of research on engineering science. This journal provides a medium of communication among engineers and scientists who have engaged in research and development concerning the fields of comprehensive engineering, while maintaining a healthy balance between fundamental and experimental topics. Now, the journal has three separate fields, the scopes of which are Part A: Maintenance Engineering; Part B: Intelligent Engineering; Part C: Engineering in Agriculture, Ocean and Light Industry shown in flows, and other specialized fields will also be updated in the near future.

Part A: Maintenance Engineering

Topics of interest for submission on the field of maintenance engineering include, but are not limited to:
Condition Diagnosis Engineering and Technology; Sensing Technology; Maintenance Management; Fault Tolerant System; Fault Self-Recovery Engineering; E-Maintenance; Signal Processing; Risk, Health and Safety Management; Structural Health Monitoring; Information and Communication Technology; Data and Information Fusion; Reliability/Quality; Maintenance Robot; Data Quality and Acquisition; Human Factors; Education and Training; Risk Based Engineering; Others on Maintenance.

Part B: Intelligent Engineering

Topics of interest for submission on the field of intelligent engineering include, but are not limited to:
Application of Artificial Intelligence in Engineering; Intelligent Design, Modeling, Planning and Control for Applied Engineering; Intelligent Robot System; Intelligent Fault Diagnosis; Intelligent Signal Processing for Applied Engineering; Others on Intelligent Engineering.

Part C: Engineering in Agriculture, Ocean and Light Industry

Topics of interest for submission on the field of engineering in agriculture, ocean and light industry include, but are not limited to:
Agriculture Engineering: Agricultural Equipment and Mechanical Engineering; Agricultural Bioenvironmental Engineering; Agricultural Renewable Energy Engineering; Agricultural Produce Processing Engineering; Agricultural Information and Electrical Technologies; Others on Agricultural Engineering.
Ocean Engineering: New Ocean Energy; Ocean Maintenance Technology; Ocean Monitoring Technology; Ocean Diagnosis Method; Ocean Experimental Development; Professional Sensor Technology; Observational and Computational Tools Others on Ocean Engineering.
Light Industry Engineering: Agri-food Products Processing/Packaging Technology and Equipment; Comprehensive Utilization of Resource; Preservation; Storage and Packaging of Agri-food Products; Innovative IT Applications in Agri-food Chain; Sensing, Testing, Automation and Internet of Things Technologies; Green Environmental Protection; Energy Saving Technologies; Others on Light Industry.

========== Manuscript Submission ==========

Manuscripts should be submitted online at http://www.iace-journal.org/ by registering and logging in to the website of the IJCE. Once you have registered, please click the “Submit Manuscript” to go to the submission from. Please use the MS Word template file to prepare your manuscript. Manuscript prepared in MS Word must be converted into a single file before submission. The Microsoft Word template file can be downloaded from the website of the IJCE.

========== Submission Declaration ==========

The submission, such as articles, reviews, technical report etc., to the IJCE means these facts that the work described has not been published previously, that it is not under consideration for publication elsewhere, that its publication is approved by all authors and tacitly or explicitly by the responsible authorities where the work was carried out, and that, if accepted, it will not be published elsewhere including electronically in the same form, in English or in any other language, without the written consent of the copyright-holder.

========== Copyright ==========

========== Review Policy ==========

The following types of contribution to the IJCE are peer-reviewed: Articles, Reviews and Technical Reports. The articles accepted for publishing in the IJCE include regular paper and letter, which will be decided by editors according the reviewing results. All forms of published correction may also be peer-reviewed at the discretion of the editors. Other contributed types to the IJCE, particularly if they present technical information, may be peer-reviewed at the discretion of the editors. For any general questions and comments about the peer-review process, the journal or its editorial policies that are not mentioned here, please contact us using the email: ijce@nifty.com. Questions about a specific submitted manuscript should be directed to the executive editor who is handling the manuscript.

International Journal of Comprehensive Engineering (IJCE)

Volume 2, Number 4, December 2013 (ISSN 2186-2680)

International Journal of Comprehensive Engineering
Part A, 2(4), 280-286, 2013
Doi: 10.14270/IJCE2013.2.4.a280
Regular paper

ISSN 2186-2680
e-ISSN 2186-2656
www.iace-journal.org

Reliability analysis of a rotary kiln axis-line measuring and management decision-making system with human errors

Guangfu Bin [1,#], Yongyi Gao [1], Xuejun Li [1] and Balbir S. Dhillon [2]

[1] Key Lab of Health Maintenance for Mechanical Equipment of Hunan Province, Hunan University of Science and Technology, Xiangtan, Hu'nan, 411201, China
[2] Department of Mechanical Engineering, University of Ottawa, 161 Louis Pasteur, Ottawa, ON Canada K1B 6N5

[#] Corresponding author: abin811025@163.com; Tel.: +86-731-5829-624; Fax: +86-731-5829-0480

Abstract: Due to lack of knowledge of human factors theory and human reliability technique, operators and analysts usually hard to address the error posed by humans that would lead to unwanted event in the process of using an axis-line measuring and management decision-making system to monitor the running axis-line of rotary kiln. This paper proposes an approach for analyzing the consequences of failures caused by human errors for a testing instrument. Firstly, the configuration and operation principles of the measuring system are presented, then, the human errors analysis of measuring and management subsystem was evaluated by applying method of fault tree analysis. It was focused on the types of human errors so as to prevent or reduce human errors for the improvement of measuring and management performances and safety in the running process of rotary kiln. Finally, according to the human information processing model and actual operational conditions, six measures to reduce or prevent the human errors in system with the aim of ensuring the normal and healthy running of rotary kiln were developed.

Keywords: Rotary Kiln Axis-line, Measuring and Management, Human Errors, Fault Tree Analysis.

Received: Sept. 8,2013 / Accepted: Oct. 8,2013 / Published: Nov. 15,2013

1. Introduction

Rotary kilns are widely used in variety of industries including metallurgy, cement, and chemical process industry [1-2]. The primary functions of a rotary kiln are to supply enough heat to raise the solids to reaction temperature and to promote an efficient mixing of these solids to ensure uniformity of heat transfer. A typical rotary kiln consists of a long and slightly tilted cylinder, rotating about its axis, which usually has weight of kiloton, length of hectometer, and four to nine supporting aprons with burden, large torque, and multi-supporting mechanism [3-4]. Here, the axis-line is a virtual line connected to all cylinder rotating centers of the supporting location of their segments, which can express the deviation between the running axis-line and the first installation axis-line in the vertical and horizontal directions of each supporting location to evaluate the running state of rotary kiln [5-7]. There are often occur with uneven load distribution problems because of the axis variations in the process of running, and even cause a great productivity losses and tragedy. Thus, it is very important to have the instruments that can monitor the running state axis-line of rotary kiln in metallurgy, cement, and chemical process industries for meeting the demands of safety, health, and high efficiency. However, due to a lack of knowledge of human factors theory and human reliability technique, operators and analysts tend not to address the errors posed by human that would lead to the unpredictable event in the process of measuring and management.

Reliability is defined as probability to perform a specified function or mission under given conditions while availability is the probability that the system or component is available when called upon [8]. When

analyzing human reliability it is necessary to identify those human actions or inactions that can affect the reliability of a system. These actions or inactions are defined as human errors. However, there are many human factor-related accidents that make up a significant proportion of all rotary kiln safety accidents. Statistics also show that human factors have played a major role in the occurrence of accidents in such measuring and management decision-making system mentioned above. Actually, human error in process industry is much more complicated to decode than simply blaming the operator. As Reason notes, "… human error is a consequence not a cause. Errors … are shaped and provoked by upstream workplace and organizational factors. Identifying an error is merely the beginning of the search for causes, not the end … Only by understanding the context that provoked the error can we hope to limit its recurrence." [9-10] Several studies have proposed methods and models to reduce the occurrence of human error and improve the poor record of the industry. For example Rasmussen's skills rules-knowledge model of decision-making [11], Wickens and Flach's four stage information processing model [12], O'Hare's wheel of misfortune taxonomy [13], Moray's socio technical model of error [14], and Reason's generic error modeling system [15]. The first two models concentrate on the micro, cognitive mechanisms that explain why an operator has erred, typically through some type of omission, commission, or violation. The latter three models are macro or systems-based, focus on the operator and the contextual upstream factors that set up the operator to err. They are all valid approaches to understanding human factors and how accidents occur. In addition, a number of human error taxonomies have been developed based on these methods and models. These taxonomies provide a theory driven classification system to allow investigators and researchers to categorize operator errors and accidents contributing factors, which in turn enable systematic analyses to be performed. A major benefit of classifying operator errors and contributing factors based on their underlying theoretical nature is in enabling trends to be identified across error forms.

This paper is aimed at the impact of human error, which is known as a major contributing factor in accident causation of rotary kiln axis-line measuring and management decision-making system. Firstly, the configuration and principle of the rotary kiln axis-line measuring and management decision-making system is presented, and then, Fault Tree Analysis method is used to analyze the possible human errors of the measuring and management subsystem. Finally, six measures to reduce or prevent the human errors in system are developed through a better understanding of human errors to ensure the normative operation, normal measuring precision, and good management performances of axis-line measuring system.

2. Rotary kiln axis-line measuring and management system

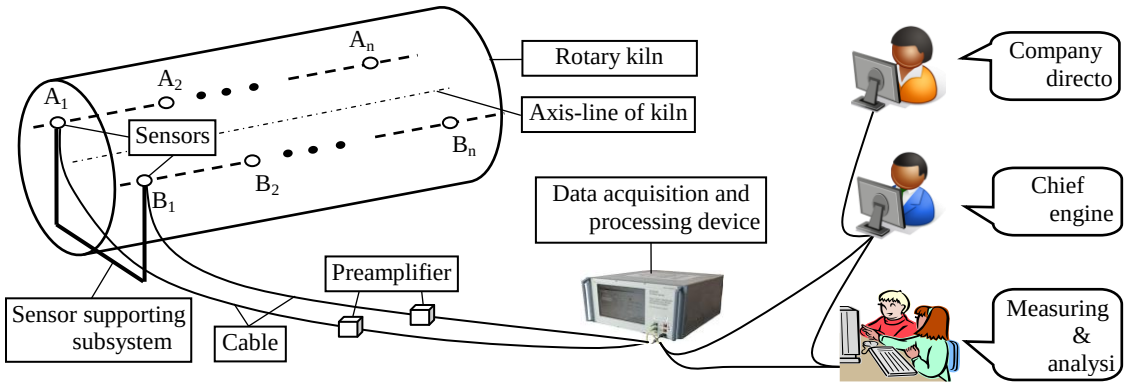

Fig. 1 Portable axis-line measuring and information management decision-making system for rotary kiln health maintenance

The axis-line measuring and management decision-making system for rotary kiln with the functions of sensing, detection, management, and optimization of decision-making that can be quickly carried out the running axis-line measuring and analysis of the working state of rotary kiln [16-17]. It consists of sensor supporting device, integrated signal acquisition device, and portable computer equipment, as shown in **Fig. 1**. The system makes use of the measuring principle of zero displacement direction key and phase to detect the running axis-line. In the system, the sensor supporting device consists of orientation supporting seat installed on each segment of rotary kiln and the mobile bracket. The mobile bracket consists of the magnetic-absorption motherboard and two iron sleeves can be adjusted both in the vertical and horizontal directions to install sensors with the angle of 150 in the vertical direction. This can achieve quite rapidly the orientation and

installation of the mobile bracket by adjusting the magnetic-absorption motherboard after demarcation of the orientation supporting seat, and the mobile bracket to ensure corresponding three-dimensional position of all segments of rotary kiln. The integrated signal acquisition device consists of two eddy current displacement sensors and their preamplifiers, digital display device, sensor power supply, and USB data acquisition card, as shown in Fig. 2. The displacement measuring-range of eddy current displacement sensor is almost 20mm, connected with preamplifier through cable, and the displacement can be obtained from the digital display device. The sensor power supply consists of a high performance lithium-ion rechargeable battery, charging circuit, voltage regulator, and electrical-level show circuit. It can continuously provide power for the integrated signal acquisition device up to 2 hours without external power supply in the actual measurement. Thus, it is very useful to use the system to measure the axis-line of rotary kiln. The portable computer equipment consists of a laptop computer and its measuring and management decision-making software system. When one measures the axis-line of rotary kiln, the analog signal of real-time displacement signal can be obtained from the sensor supporting device, and converted it to data signal through the integrated signal acquisition device, and then, send to the laptop computer for further analysis. The result of measurement and analysis is connected with the office of chief engineer and company director to help the manager to make best optimization of decision-making [7,18].

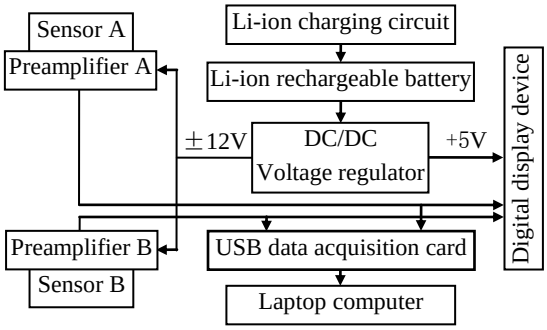

Fig. 2Sketch map of the integrated signal acquisition and detecting device

3.Human error analysis of rotary kiln axis-line measuring and management system

The failure of rotary kiln axis-line measuring and management decision-making system is not only caused by hardware or software malfunctions, but also by human errors. The human factors analysis is necessary and essential approach in order to understand the possible errors caused by humans and optimize operability. It is also critical for ensuring that the risks of a major accident are as low as reasonably practicable. Some of these are discussed below.

3.1 Concepts on human error

Human error is an inappropriate or undesirable human decision or behavior that reduces, or has the potential for reducing, effectiveness, safety or system performance. There are various forms of human error analysis have been widely used in many industry sectors, although the specific tools used for the purpose vary. The human information-processing model proposed by Wickens describes four stages of human information-processing and performance, namely perception, memory, decision-making and action [12]. When performing task, people perceive information about the outside world using all of the senses, and may use this information along with information retrieved from memory to arrive at decisions that are used to determine and execute action [19-20].

A human error can occur as a result of a failure in any of the above four stages, as the following process industry examples illustrate:

(1) Perception error-misperceive a reading on a display;

(2) Memory error-forget to implement a step in a procedure;

(3) Decision error-fail to integrate various pieces of data and information, resulting in misdiagnosis of a process upset;

(4) Action error-inadvertently operates the wrong device.

To find out why these four types of error happen, it is necessary to establish what caused the failure in that part of the human information-processing system, i.e., what were the potential psychological factors? As well as, explaining why an error has occurred. Furthermore, the potential psychological factors also give us strong indications as to what we can do to prevent the occurrence of such errors, or reduce their impact [21].

It is also necessary to be aware of the fact that human performance in general is very heavily influenced by the surrounding conditions. Such conditions are known as performance-shaping factors, and can help to further clarify why an error has occurred, and also provide additional information to help specify a practical solution. Examples of performance-shaping factors, which may increase the possibility of error, include very high workload, poor equipment, and inadequate training.

3.2 Human error analysis of measuring and management system based on FTA

Fault tree analysis (FTA) is widely performed in the industry to evaluate engineering systems during their design and development. A fault tree may simply be described as a logical representation of the relationship of primary events that lead to a specified undesirable event called the "top event" and is depicted using a tree structure with OR, AND, etc. logic gates [22-23]. This method can also be used to perform human error analysis of the measuring instrument and management system.

In this study, an axis-line measuring and management decision-making system for rotary kiln health maintenance used in the Hunan Shaofeng Cement Group Co.,Ltd. is taken as an example. It mainly consists of sensor supporting subsystem, measuring subsystem, and management subsystem. The function of rotary kiln axis-line measuring subsystem mainly consists of sensor supporting and setting unit and data acquisition and processing unit. According to the function principle, the failures of rotary kiln axis-line measuring subsystem performed by humans usually involve sensor supporting and setting function performed incorrectly, data acquisition and processing function performed incorrectly, and errors caused by work conditions and human pressure. A fault tree for the event that rotary kill's axis-line measuring subsystem performed incorrectly by person is shown in Fig.3.

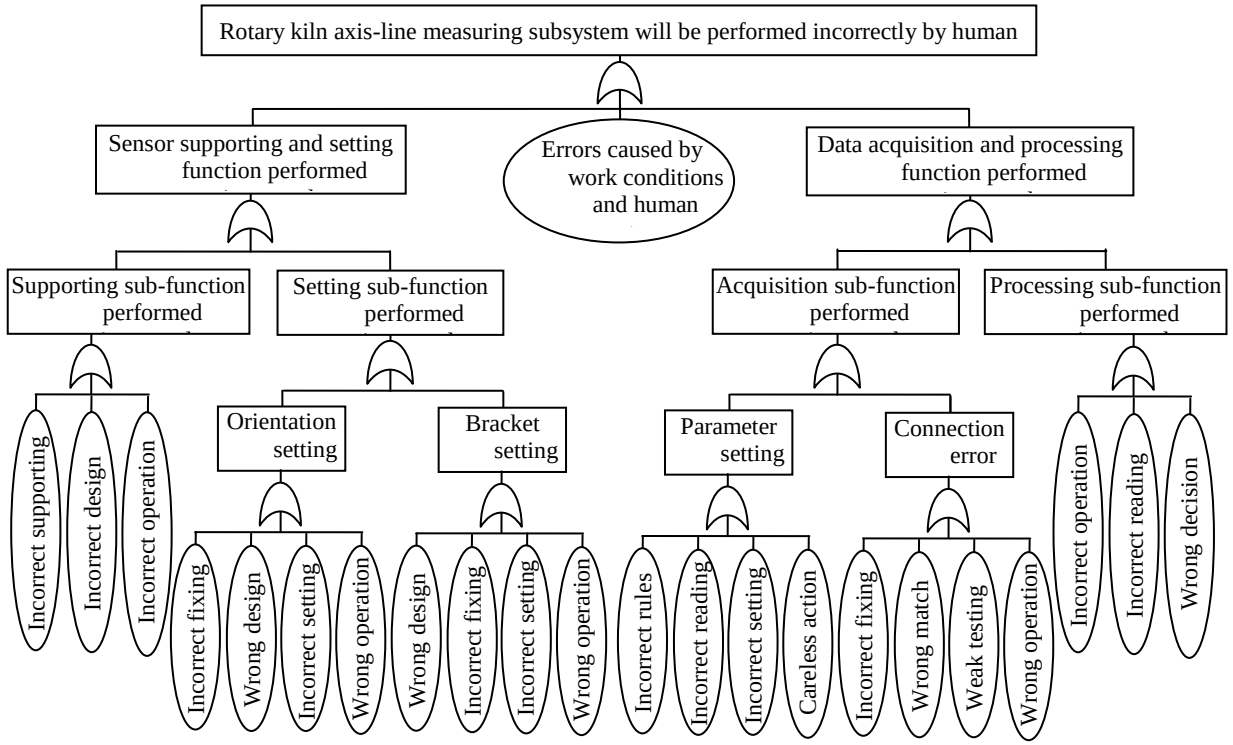

Fig.3. Fault tree for the performance of rotary kiln axis-line measuring subsystem incorrectly

It can be seen from the fault tree that above three functions must be performed correctly for the successful completion of the measuring subsystem. The sensor supporting and setting function is made up of two sub-function sensor supporting and sensor setting. If any one of these two sub-functions is performed correctly, function sensor supporting and setting can be completed successfully. Function data acquisition and processing is composed of sub-function data acquisition and data processing. Both of these two sub-functions

must be performed correctly for the success of function data acquisition and processing. Both sub-functions, sensor supporting and data processing, are composed of three human tasks each, i.e., supporting, design, operation, and operation, reading, decision, respectively. All factors for each of these two sub-functions must be completed correctly for sub-function success. Moreover, both sub-functions, sensor setting and data acquisition, are subjected to two types of human errors each, i.e., orientation setting error, bracket setting error, and parameter setting error, connection error, respectively. These errors can be caused by human tasks including incorrect fixing, wrong design, wrong operation, weak testing, and so on. All errors for each of these two sub-functions may be lead to the failure of sub-function. In addition, the part of errors caused by work conditions and human stress mainly indicates that some factors affected person's performance include high workload, time to work, fatigue, group interaction, repetitive work, inadequate training, big noise, and bad measuring conditions.

Rotary kiln axis-line management decision-making subsystem is an important function part integrated with the measuring subsystem for making-decision, whether the displacement of the corresponding supporting aprons needs to be adjusted for ensuring the running axis-line is consistent with the ideal line, on the basis of data collected from eddy current displacement sensor. The axis-line management decision-making subsystem usually consists of management decision-making software, communication tool, and laptop computer. The common human errors that may occur in the process of using management decision-making function of mentioned instrument above, and other special human errors include inadequate execution for setting measuring parameters of individual operation on different measuring locations. In addition, there are many errors that usually occur in the equipment field-use environment due to operating personnel, when they fail to follow correct procedures, or there is lack of correct procedures. More specifically, some of the factors that can lead to operator errors are task complexity, operator carelessness, heavy mental or physical stress, poor environmental conditions, lack of proper procedures, and departure from following the correct operating procedures [24-25]. Therefore, it is vital to consider human factors during the usage phase of the axis-line management decision-making subsystem to have an effective and low failure rate of human-machine compatible system.

3.3 Human error and measure to be taken

As we all known that it would not be possible to design technological systems to eliminate all human errors during operation because people are involved in: specifying, designing, implementing, installing, commissioning, and maintaining systems as well as operating them. This paper analyzes the incidents caused by human error in the rotary kiln axis-line measuring and management decision-making system and concludes that, it is necessary to focus on behaviors and methods so as to prevent or reduce human error for the improvement of instrument performances and safety in running process of rotary kiln. The best way is to make and find out what to do to prevent or reduce them, based on the comprehension of different types of human errors.

There are several methods and measures to prevent or reduce human errors in the usage of instruments. According to the human information-processing model that describes four stages of human performance, we can develop some countermeasures to reduce or prevent human errors in the rotary kiln axis-line measuring and management decision-making system, as follows:

(1) The more complex the task, the easier to make an error. The rotary kiln axis-line measuring and management decision-making system should be specially designed and optimized for individual industry according to the capabilities of operator.

(2) To reduce the error probability, the time span of testing and measuring may be two times larger than the necessary time to reduce some perception errors and action errors.

(3) The integration and automation of hardware should generally be recommended in the system to reduce operation errors or action errors as much as possible, i.e. incorrect fixing, incorrect setting, wrong operation, and so on.

(4) Human activity should be considered into the system to keep up with his/her concentration and state of training, and therefore reduce the total failures of the system.

(5) The operation rules of measuring system should be provided for the operator, so that he/she can correctly operate the system to reduce memory errors or action errors.

(6) To improve operator reliability and reduce decision errors or action error, working conditions and operator stress characteristics including high noise, high temperature, very short decision-making time, requirement for prolonged monitoring, and more measuring steps. In addition, repetitive measuring and analysis tasks must be considered carefully during the operation phase.

4. Conclusions

In this paper, a method that is analyzed failures caused by human errors for a rotary kiln axis-line measuring and management decision-making system has been developed. As case study, the principle of rotary kiln axis-line measuring and management decision-making system was presented and the human error analysis of measuring and management subsystem was evaluated. It was focused on the types of human errors and the reasons of human errors so as to prevent or reduce the occurrence of human error for the improvement of measuring and management performances and safety in running process of rotary kiln. Finally, according to the human information-processing model that describes four stages of human performance, we developed six measures to reduce or prevent human errors in the process of using rotary kiln axis-line measuring and management decision-making system, with the aim of ensuring the normal and healthy running of rotary kiln. Moreover, the human error analysis method should be useful in the process of fault diagnosis and maintenance for the similar measuring and management decision-making system.

Acknowledgments

This work was supported by the project of National Natural Science Foundation of China (No. 51205121, 51175172), and the project of Natural Science Foundation of Hunan Province (No. 14JJ5011).

References

[1] P.V Barr, J.K Brimacombe, A.P Watkinson. Heat-transfer model for the rotary kiln: Part II. Development of the cross-section model, *Metallurgical Transactions*, 1989,20B(3):403-419.

[2] R. Jauhari, M.R Gray, J.H Masliya. Gas-solid mass transfer in a rotating drum, *Canadian Journal of Chemical Engineering*, 1998,76(2):224-232.

[3] M.A Martins, L.S Oliveira, A.S Franca. Modeling and simulation of petroleum coke calcination in rotary kilns, *Fuel*, 2001, 80(11):1611-22.

[4] A. Meier, E. Bonaldi, G.M Celia, W. Lipinski. Multitube Rotary Kiln for the Industrial Solar Production of Lime, *Transactions of the ASME, Journal of Solar Energy Engineering*, 2005,127(3):386-395.

[5] K. Mizoguchi, K. Hoshino, K. Shirakawa, Y. Tanigawa. Theoretical and Experimental Researches on Strength of A Rotary Kiln. *Bulletin of the JSME*, 1980, 23(185):1753-1762.

[6] Y. Zhang. Increasing Plant Availability by Mechanical Checking of the Cement Rotary Kiln Axis, *Journal Wuhan University of Technology*, 2001,16(3):76-78.

[7] Li X J, Liu Y L, Chen A H. *The theory and technology of health maintenance in the rotary Kiln*, Beijing, China: China Machine Press, 2005.

[8] H. Fazlollahtabar. Reliability-Based Dynamic Programming for E-Learning User Profile Assessment, *International Journal of Information & Communication Technology Education*, 2012, 8(3):13-21.

[9] Reason J. *Managing the Risks of Organizational Accidents*, Ashgate Publishing Ltd., Aldershot,1997.

[10] D. S Alan. Human reliability analysis: Need, status, trends and limitations, *Reliability Engineering & System Safety*, 1990, 29(3):301-313.

[11] Rasmussen J. *Human errors: a taxonomy for describing human malfunction in industrial installations*, J. Occup. Accid. 1982, 4:311-333.

[12] Salvendy G. *Handbook of human factors and ergonomics*, Hoboken, NJ, Wiley, 2012.

[13] D. O'Hare. The "wheel of misfortune": a taxonomic approach to human factors in accident investigation and analysis in aviation and other complex systems. *Ergonomics*, 2000,43(12):2001-2019.

[14] N. Moray. Culture, politics and ergonomics. *Ergonomics*, 2000,43:858-868.

[15] Reason J. *Human Error*, Cambridge University Press, New York ,1990.

[16] X.J Li, K.F He, J.W Zhao. Portable fast measurement and information management decision-making system for rotary kiln health maintenance, *Journal of Electronic Measurement and Instrument*, 2006, 20(4):55-59.

[17] X.J Li, G.F Bin, B.S Dhillon, P.Y Zhu. Reliability Analysis of an Axis-line Measuring and Management Decision-making System for Rotary Kiln, *International Conference on Measuring Technology and Mechatronics Automation(VOL.Ⅲ)*, Zhangjiajie, China, 2009:816-820.

[18]X.J Li, G.F Bin, B.S Dhillon. Reliability Analysis of an Integrated and Multifunctional Vibration Signal Measuring Instrument for Rotary Machine, *the proceedings of 2009 8th International Conference on Reliability, Maintainability and Safety(VOL.II)*, Chengdu, China, 2009:978-981.

[19]A.S Tarcisio, T.F Carlos, B. C Fabricio. Analysis of a safety planning and control model from the human error perspective, *Engineering, Construction and Architectural Management*, 2005,12(3):283-296.

[20]Wickens C D. *Engineering Psychology and Human Performance*, Harper Collins press, New York, USA,1992.

[21]R. Lardner, R. Scaife. Helping Engineers to Analyse and Influence the Human Factors in Accidents at Work, *Trans IChemE, Part B, Process Safety and Environmental Protection*, 2006, 84(B3):179-183.

[22]Dhillon B S, *Human Reliability and Error in Transportation Systems*, Springer London Ltd Press, 2007.

[23]X.J Li, G.F Bin, B.S Dhillon. Model to evaluate the state of mechanical equipment based on health value. *Mechanism and Machine Theory*, 2011, 46(3):305-311.

[24]P.Y Zhu, B.S Dhillon, X.J Li, G.F Bin. Reliability analysis of an interrogation instrument for optical fiber Bragg grating sensing, *Chinese Journal of Scientific Instrument*, 2008,29(4):3-8.

[25]Walker, I R. *Reliability in scientific research: improving the dependability of measurements*, calculations, equipment, and software, Cambridge University Press, New York, 2011.

International Journal of Comprehensive Engineering
Part B, 2(4), 287-293, 2013
Doi: 10.14270/IJCE2013.2.4.b287
Regular paper

ISSN 2186-2680
e-ISSN 2186-2656
www.iace-journal.org

Fault Diagnosis for Roller Bearings Using WPT and ACO

Liuyang Song [1], Huaqing Wang [1,#], Jianfeng Yang [1], Wenbin Liu [1,#] and Peng Chen [2]

[1] School of Mechanical & Electrical Engineering, Beijing University of Chemical Technology, Beijing, 100029, China
[2] Graduate School of Bioresources, Mie University, Tsu, 514-8507 Mie, Japan

[#] Corresponding author: wanghq_buct@hotmail.com, liuwb1437@263.net; Tel.: +86-010-64443037

Abstract: The main point of vibration monitoring and fault diagnosis is feature extracting and classifying. The wavelet packet transform, a perfect tool for the analysis of non-stationary signals and fault features extraction, has excellent time-frequency characteristic. The ant colony optimization, a novel swarm intelligence algorithm, has been researched abroad in recent years. This paper combines the two ways and provides a new approach to intelligent fault diagnosis based on wavelet packet transform and the ant colony optimization. The new method is evaluated using experimental signals. Vibration signal of fan roller bearings was decomposed into sub-frequency bands by wavelet packet transform and then energy of each band was calculated. The best vector is choosing as the symptom parameters reflecting the feature of vibration signals measured. The states identification for machinery diagnosis is converted to clustering problem of different states. Euclidean distance is used to measure distance in clustering algorithm. And the analysis results demonstrate that the proposed method can recognize the faults types effectively.

Keywords: Ant Colony Optimization, Roller Bearings, Fault Diagnosis, Clustering, Wavelet Packet Transform.

Received: Apr. 21,2012 / Accepted: Aug. 12,2013 / Published: Nov. 15,2013

1. Introduction

Throughout the years, a myriad of techniques for classification has been proposed [1], such as decision tree based [2], statistical [3], neural networks [4] and rule based [5].The present paper describes the application of ACO clustering algorithm for fault diagnosis of a roller bearing. The ACO, a kind of intelligent algorithm, mimics the way realyh7 ants find the shortest route between a food source and their nest. Indirect communication features make the system has good scalability. In addition, the method has strong robustness, parallel computing mechanism and easy to combine with certain heuristics.

The ACO has been applied to solve the process optimization problems such as flowshop scheduling [6], feature selection of a pattern recognition system [7], dynamic process control [8], data mining [9], and discovery of classification rules [10], etc. For example: optimize the parameters of the neural network. A random class is given to each unknown parameter. Ants randomly select one from each collection to build neural models and calculate the training error. Then update the pheromone matrix according to the results. When the algorithm is convergent, the global optimization solution gained. The results show that the improved algorithm can get the optimal value more quickly [11].

In the following, the basic idea of ant colony optimization (ACO) is introduced in Section 2. The brief idea of wavelet packet transform (WPT) is introduced in Section 3.The proposed models for fault diagnosis of roller bearing are explained in Section 4. In Section 5, the experimental result is shown. In Section 6, we draw a general conclusion.

2. The Basic Principle and Mathematical Description of ACO

In the early 1990s, ACO was introduced by M. Dorigo and colleagues as a novel nature-inspired metaheuristic for the solution of TSP problems. The TSP problem can be described as the problem of finding a minimal length closed tour that visits each town once. In the following parts, we will simply describe the basic mathematical description about ACO in solving TSP.

The medium used to communicate between ants is pheromone. In the feeding process, the moving ant lays some pheromone on the ground to marking the path. When other ant encountering a previously laid trail, it can detect the pheromone and decide with high probability to follow it, thus increase the trail with its own pheromone. The process is thus characterized by a positive feedback loop, where the probability with which an ant chooses a path increases with the number of ants that chose the same path in the preceding steps [12]. After arrive the food source, ants return to the nest along the same route.

After each round, pheromone should be updated: including the quantity per unit of length evaporated and laid on the edge by the ant. Pheromone evaporation mechanism made the ants ignored the poor path selected before. As a result, avoid the algorithm converging to local optimization early. ρ is an evaporation coefficient. When the evaporation rate is set to 1, there is no pheromone evaporation, and not easy to get convergence. But setting ρ too low is prone to get a local best answer.

The intensity of pheromone on path-ij at time t+1 is given by Eq. (1) [13] :

$$\tau_{ij}(t+1) = \rho \cdot \tau_{ij}(t) + \Delta\tau_{ij}(t, t+1) \tag{1}$$

Define the transition probability for the k-th ant from town i to town j as Eq.(2) [13]:

$$p_{ji}^{k} = \sum_{l=1}^{n} \frac{[\tau_{ij}]^{\alpha}[\eta_{ij}]^{\beta}}{[\tau_{il}]^{\alpha}[\eta_{il}]^{\beta}} \tag{2}$$

The field of algorithms of the ant system (AS) can be divided into three categories determined by the way the trail is updated: ant-cycle, ant-quantity and ant-density algorithms, the formulas are given by Eq. (3-5) [13]. In ant-cycle model each ant lays its trail at the end of the tour, but the other two models updated the trail after each step. Ant-cycle is widely used, and the other two models have been eliminated.

Where $\Delta\tau_{ij}^{k}$ is the quantity per unit of length of pheromone laid on edge (*i,j*) by the *k-th* ant between time *t* and *t+1*; Q is a constant; d_{ij} is the euclidean distance between i and j; L_k is the tour length of the *k-th* ant.

ANT-quantity:

$$\Delta\tau^{k}{}_{ij}(t, t+1) = \begin{cases} \dfrac{Q_1}{d_{ij}}, \\ 0, \end{cases} \tag{3}$$

ANT-density：

$$\Delta\tau^{k}{}_{ij}(t, t+1) = \begin{cases} Q_2, \\ 0, \end{cases} \tag{4}$$

ANT-cycle:

$$\Delta\tau^{k}{}_{ij}(t, t+n) = \begin{cases} \dfrac{Q_3}{L^K}, \\ 0, \end{cases} \tag{5}$$

In cluster analysis, the value of the clustering center is equal to the average of objects belonging to the class. A variety of methods can calculate the distance between the sample and the clustering center, such as euclidean distance, cosine angle distance method, binary angle cosine law, in this paper, we use the euclidean distance. Physical meaning of Euclidean distance is expressed as m-dimensional real space distance of two points, can be expressed as Eq. (6).

$$\rho = [(x_1 - y_1)^2 + (x_2 - y_2)^2 + (x_3 - y_3)^2 + \cdots + (x_{m-1} - y_{m-1})^2 + (x_m - y_m)^2]^{1/2} \tag{6}$$

3. The Brief review of the wavelet packet transforms

Wavelet analysis (WA) is a multi-resolution analysis method that has been widely used and developed for advancement in recent years. The basic idea of multi-resolution analysis is to project the signal into a series of localization wavelet function, which has better resolution in low and high frequency range. It is an effective tool to analyze the unstable vibration. In the field of machinery diagnosis, WA has been used in the diagnosis of rolling bearings, gearbox, and compressors, and the technique has also been used for feature extraction and noise cancellation of the measured signals. Wavelet packet transform (WPT) is a more precise orthonormal decomposition method based on multi-resolution analysis. The difference between WPT and the basic wavelet decomposition algorithm WA is that both details and approximations are split into finer components when using WPT. 2n subspaces are obtained when the signal is decomposed to the number n layer. Fig.1 shows the difference between a wavelet packet decomposition tree of three levels and wavelet tree of three levels (dashed line), and illustrates the wavelet tree is a part of the wavelet packet tree. [14-16]

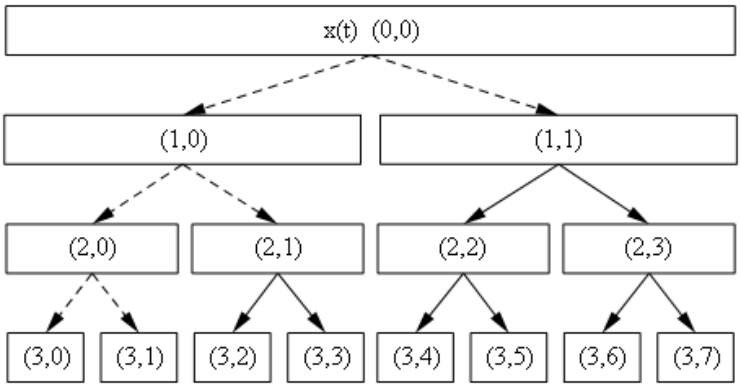

Fig. 1 Wavelet packet tree of three levels.

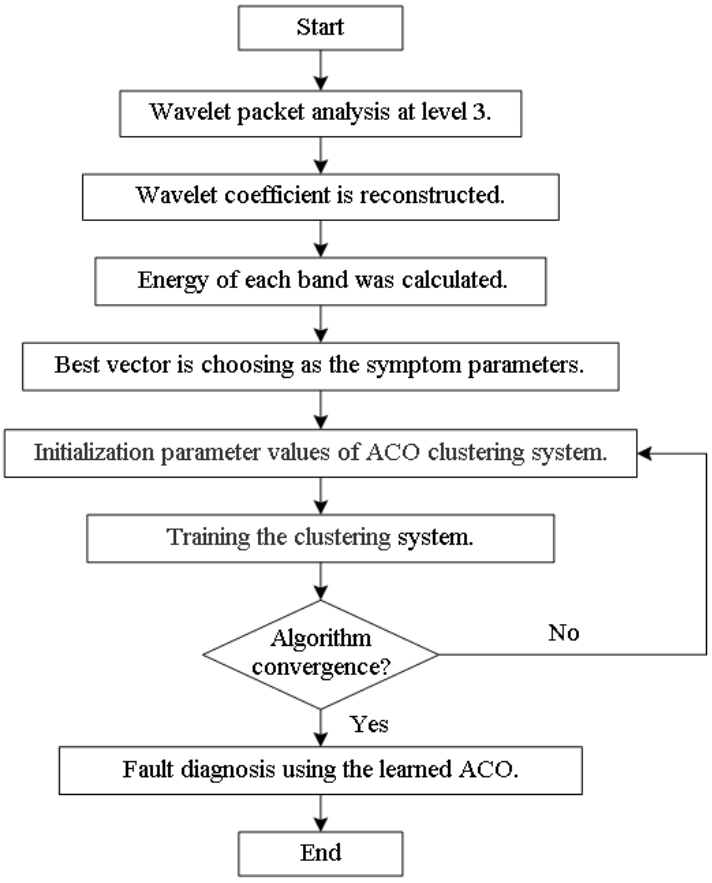

Fig. 2 The flowchart of the propose methods.

4. Bearing Fault Diagnosis Using WPT and ACO

Artificial neural network (ANN), support vector machine (SVM) and Fuzzy classifier are widely used as classification tools and reported in literature [17]. The main aim of fault diagnosis is to find whether the bearing is good or faulty. If faulty, then the objective is to segregate the fault into one of the faults considered above. The paper analyzes the vibrations signals by WPT and ACO clustering algorithm to identify equipment working state.

The experimental collected the field vibration signals by the acceleration sensors. The accelerometer is mounted on the bearing house. The rotating speed of is 800rpm, sampling frequency is 100 KHz, and sampling time is 20 sec. The vibration signal is captured for the conditions: good bearing (N), bearing with inner race fault (IRF), bearing with outer race fault (ORF), and bearing with roller fault (RF). Fig.2 shows the flowchart of the proposed methods.

Firstly, the sensor data was decomposed using wavelet packet at level 3 to achieve the decomposition tree. Then, the wavelet coefficients were reconstructed, the energy of each band was calculated and the vectors with good capability choose as symptom parameters (SPs) using in the following process.

5. Experimental result

When apply the proposed ACO clustering method to identify the working state, we first begin to train the ACO to get the clustering centers and the reasonable number of iterations. The object, P_1, P_2 and P_3, are vectors corresponding to the node (3, 7, and 8) which selected as the best vectors. Put the known state objects into the ACO classifier. When the algorithm is convergent and the clustering result is correct, we can obtain four clustering centers as shown in Table.1.

Table 1 Clustering centers.

Status	Parameters		
	P_1	P_2	P_3
Normal	41.3292	29.6624	11.0312
Inner race fault	117.51	64.4474	28.3522
Outer race fault	1363.98	1538.24	610.578
Roller fault	457.434	384.374	186.998

In order to evaluate the performance of the ACO clustering algorithms, SPs have not been learnt by the ACO are put into learnt ACO. The clustering centers were utilized to identify the fault type. Ants are used to construct solutions. They need to cluster the test samples into groups accroding to the clustering center obtained through training. The solutions is random at first. The sum total of the distance between all samples and their centers is computed to measure the effect of the soultion. Then ants updated the pheromone matrix with the total distance and then construct new solutions using the pheromone matrix information. The algorithm loops until the certain iteration number obtained through training. At the end of the loop, the pheromone matrix shows the clustering result, and reflects the proformance of the clustering situation.

ACO clustering algorithm is proposed to cluster these 20 objects into 4 clusters. Use the ant colony algorithm to cluster these samples. When the algorithm is convergent, we can judge the state by the pheromone matrix. The value of the pheromone in each state represented the probability of the ants putting the object into the class. The largest value is for the class of sample x_i.

The 3D views of the clustering result during the process were shown in Fig. 3. The pheromone matrix after classification was shown in Table. 2.

The pictures described the gradual development process of clustering. Based on the values of pheromone in matrix can judge the category of the test data and the fault type of the device: that samples 1-5 defined as category A, samples 6-10 defined as category B, samples 11-15 defined as category C, samples 16-20 defined as category D, as shown in Table. 2. Because the order of the categories was matched with the order of clustering centers, it is suggested that: samples 1-5 are normal state bearing signals; samples 6-10 are inner race defect signals samples 11-15 are outer race defect signals and samples 16-20 are roller defect signals. The results prove the effectiveness of the method in fault diagnosis.

Table. 2 Pheromone matrix of known state

Samples	States	Pheromone in each state			
		A	B	C	D
1	Normal	7.38E-07	2.01E-20	4.98E-21	6.45E-21
2		7.38E-07	1.45E-20	5.00E-21	4.10E-20
…		7.38E-07	9.91E-21	4.98E-21	5.43E-21
5		7.38E-07	2.16E-20	4.98E-21	6.75E-21
6	IRF	4.05E-20	7.38E-07	5.00E-21	5.47E-20
7		1.52E-19	7.38E-07	4.98E-21	6.15E-21
…		2.20E-20	7.38E-07	4.98E-21	6.01E-20
10		3.77E-19	7.38E-07	4.98E-21	6.32E-21
11	ORF	4.98E-21	4.98E-21	7.38E-07	5.01E-21
12		5.00E-21	4.98E-21	7.38E-07	5.03E-21
…		4.98E-21	4.98E-21	7.38E-07	5.04E-21
15		4.98E-21	4.98E-21	7.38E-07	5.12E-21
16	RF	2.44E-20	6.60E-21	5.00E-21	7.38E-07
17		5.15E-21	8.01E-21	5.08E-21	7.38E-07
…		1.03E-20	6.22E-21	5.00E-21	7.38E-07
20		6.89E-21	6.60E-21	5.04E-21	7.38E-07

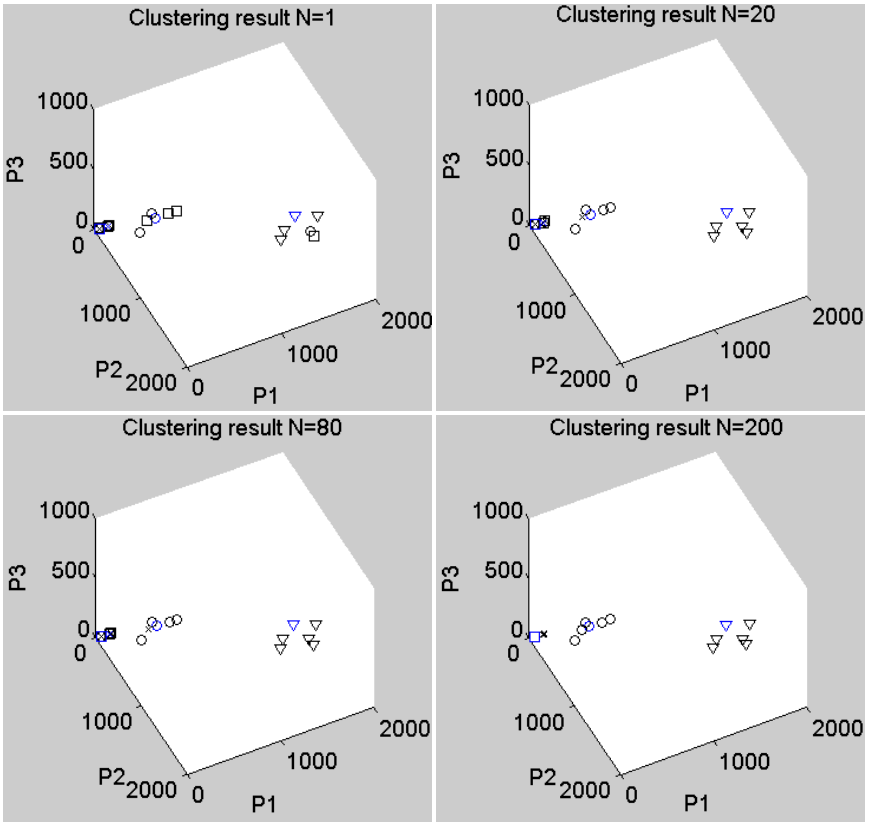

Fig. 3 Clustering result during the process.

6. Conclusion

The experiment prove that the combination of wavelet packet transform (WPT) and the ant colony optimization (ACO) is effective in rolling bearing fault pattern recognition.Three types of faults, such as the inner race fault (IRF), outer race fault (ORF) and roller fault (RF) in a blower machine are considered in this paper, and the states identification for machinery diagnosis is converted to clustering problem of different states. The input vector, which is composed by energy value of the selected reconstructed wavelet coefficient, is putted into ACO classifier to recognize and classify. The result demonstrates this method could better recognize the working state of rolling bearing and require only a small amount of training samples and short computation time.

Acknowledgment

This project is supported by National Natural Science Foundation of China (Grant No. 51075023, 51375037), National Program on Key Basic Research Project (Grant No. 2012CB026000), and Fundamental Research Funds for the Central Universities (Grant No. ZZ1124).

References

[1] D. J. Hand. Pattern detection and discovery, Lecture Notes in Computer Science, *Lecture Notes in Computer Science*, Vol. 2447, pp. 161-173, 2002.

[2] S. Y. Chang, C. R. Lin and C. T. Chang. A Fuzzy Diagnosis Approach Using Dynamic Fault Trees, *Chemical Engineering Science*, Vol. 57, pp. 2971-2985, 2002.

[3] J. T. Hsiung and D. M. Himmelblau. Detection of Leaks in a Liquid–Liquid Heat Exchanger Using Passive Acoustic Noise, *Computers & Chemical Engineering*, Vol. 20, pp. 1101-1111, 1996.

[4] Czeslaw T. Kowalski and Teresa O. K. Neural Networks Application for Induction Motor Faults Diagnosis, *Mathematics and Computers in Simulation*, Vol. 63, pp. 435-448, 2003.

[5] A. H. C. van Kampen and Z. Ramadan. Learning Classification Rules From an Ion Chromatography Database Using a Genetic Based Classifier System, *Analytica Chimica Acta*, Vol. 344, pp. 1-15, 1997.

[6] C. Rajendran and H. Ziegler. Ant-Colony Algorithms for Permutation Flowshop Scheduling to Minimize Makespan/Total Flowtime of Jobs, *European Journal of Operational Research*, Vol. 155, pp. 426-438, 2004.

[7] X. L. Zhang, X. F. Chen and Z. J. He. An Aco-Based Algorithm for Parameter Optimization of Support Vector Machines, *Expert Systems with Applications*, Vol. 37, pp. 6618-6628, 2010.

[8] J. Xiao and Z. K. Zhou. Ant Colony System Algorithm for the Optimization of Beer Fermentation Control, *Zhejiang University Science*, Vol. 5, No. 12, pp. 1597-1603, 2004.

[9] T. Niknam and B. Amiri. An Efficient Hybrid Approach Based on Pso, Aco And K-Means for Cluster Analysis, *Applied Soft Computing*, Vol. 10, pp. 183-197, 2010.

[10] J. Z. Ji, N. Zhang and C. N. Liu. An Ant Colony Optimization Algorithm for Learning Classification Rules, *WI '06 Proceedings of the 2006 IEEE/WIC/ACM International Conference on Web Intelligence*, pp. 1034-1037, IEEE Computer Society, 2006, Washington DC, USA.

[11] K. F. Liu and Z. W. He. Fault Diagnosis of Condensing Equipment Based on Ant Colony Neural Network, *Computer Simulation*, Vol. 5, pp. 214-217, 2008.

[12] A. Colorni, M. Dorigo and V. Maniezzo. Distributed Optimization by Ant Colonies, *European conference on artificial life*, Elsevier publishing, pp. 134-142, 1991.

[13] M. Dorigo, C. Blum. Ant Colony Optimization Theory: a Survey, *Theoretical Computer Science*, Vol. 344, pp. 243-278, 2005.

[14] L. X. Gao, Z. J. Yang, H. Q. Wang and P. Chen. Roller Bearing Fault Diagnosis Based on Nonlinear Redundant Lifting Wavelet Packet Analysis, *Sensors*, Vol. 11, pp. 260-277, 2011.

[15] H. Q Wang and P. Chen. Fuzzy Diagnosis Method for Rotating Machinery in Variable Rotating Speed, *IEEE Sensors Journal*, Vol. 11, No. 1, pp. 23-34, 2011.

[16] M. Li and P. Zhao. The Application of Wavelet Packet and SVM in Rolling Bearing Fault Diagnosis, *IEEE International Conference on Mechatronics and Automation*, pp. 505-508, 2008.

[17] W. Nu, L. F. Xu and S. G. Hu. Fault Diagnosis Method for Power Transformer Based on Ant Colony –SVM Classifier, *Computer and Automation Engineering (ICCAE) The 2nd International Conferenc*e, pp. 629-631, 2010.

International Journal of Comprehensive Engineering
Part B, 2(4), 294-299, 2013
Doi: 10.14270/IJCE2013.2.4.b294
Regular paper

ISSN 2186-2680
e-ISSN 2186-2656
www.iace-journal.org

Adaptive Control of NC Machining Parameters Based on Fuzzy Control Theory

Hengli Liu [1,#], Taiyong Wang [1], Fuxun Lin [1] , Kaifa Wu [1] and Ruoyu Liang [1]

[1] Key Laboratory of Mechanism Theory and Equipment Design of Ministry of Education ,Tianjin university, Tianjin,300072, China

[#] Corresponding author: lhl669@163.com; Tel.: +86-13820698937

Abstract: For the importance of NC machining parameters on the machining process, the adaptive control method of NC machining parameters is elaborated based on fuzzy control theory. According to the established control model and the fuzzy control principle, compiled C + + source procedure, and simulated the experimental data to verify the feasibility of procedures, and finally, embedded the procedures into the existing numerical control system by the VC + + visual software, achieved the dynamic display of adaptive control processing. The results showed that the effectiveness of the adaptive control model and made NC machine maintain the good stability in the whole machining process.

Keywords: NC Machining Parameters, Fuzzy Control Theory, Adaptive Control.

Received: May 24,2012 / Accepted: Aug. 12,2013 / Published: Nov. 15,2013

1. Introduction

NC machining parameter selection directly determines the processing accuracy and the efficiency, thus induces more and more research of optimizing machining parameters and establishing general optimization parameter database. In the 1980s, some domestic scientific research institutes have developed some oriented small database, but so far there is still not universal knowledge base system of metal cutting in China [1].So far, offline cutting parameters optimization technique is the most commonly used. Usually, it chooses the efficiency, costs and quality of one or more as the goal to establish the mathematic model. Then it selects appropriate optimization method for specific parts of a procedure to select a set of optimum parameters, such as feed rate, spindle rotating speed, etc [2]. The offline optimization technique has the strong prediction, can not reflect the true working state. And based on the reviewing literature, the existing NC machining parameter optimization studies are mostly offline optimization, only the different optimization methods. Therefore, in order to improve the performance of NC system, the online optimization of machining parameter is an urgent task to study.

2. Adaptive Control Model of Machining Parameter

2.1 Fuzzy control solutions

The fuzzy set theory was proposed by L.A.Zade, professor of the California University of the United States in 1965. Human judgment and thinking process can be directly expressed as relatively simple mathematical form, so that, the practical and realistic dealing with the problem is possible. The fuzzy logic system based on the fuzzy set provides a powerful tool for the control problem which lacking of accurate control model [3].

For the NC machining process, it is dynamic, the processing parameters changing moments, and it is difficult to accurately control and optimization of processing parameters [4]. Therefore, using the fuzzy control theory can solve this problem and realize the online adaptive control of machining parameters. By detecting the machining variables to adjust the cutting parameters in real time, acquire the optimal cutting efficiency, improve machining quality, and realize the machining process optimization for changing environment through the adaptive adjustment of cutting parameters [5].

For the NC machining parameter, the cutting force is generally believed that it can reflect the machine state and is one of the main parameters affecting the processing performance. And it must to maintain the cutting force smooth, not greater volatility. So the cutting force as the object of study is widely carried out [6]. But in fact, the cutting force and the main motor power have the following relations.

$$P = F_c v/(6\times10^4\times\eta) \tag{1}$$

Where P was main motor power; F_c was cutting force; v was cutting speed and η was efficiency coefficient. Thus, when other parameters remained unchanged, the cutting force and machine power has the linearly relationship, so it select the motor current instead of the cutting force as the monitor signal for state analysis [7] [8].

2.2 Adaptive control model

From the above, intelligent NC expect to achieve the optimal control of NC machining based on the monitoring of the actual machining physical state and make adaptive adjustment to the external changing conditions, return to the desired state [9]. So, it selected the current as the condition monitoring parameters, and according to the analysis of parameters affecting the cutting force, selected the feed rate changes U_{a_f} as system adjustment, and chose the current as the decision to constitute the closed loop feedback control of the machining system[10] [11].

According to the principle of fuzzy control, it chose the current deviation E_1 and deviation change rate EC_1 as the input language variable, chose the feed rate change U_{a_f} as the output variables. And based on the signals monitoring of the main motor current and voltage signals, established the adaptive control model of the NC machining process, shown in Figure 1 [12] [13] [14]. In this, the adaptive adjustment of feed can be achieved by the real-time adjustment of U_{a_f} .

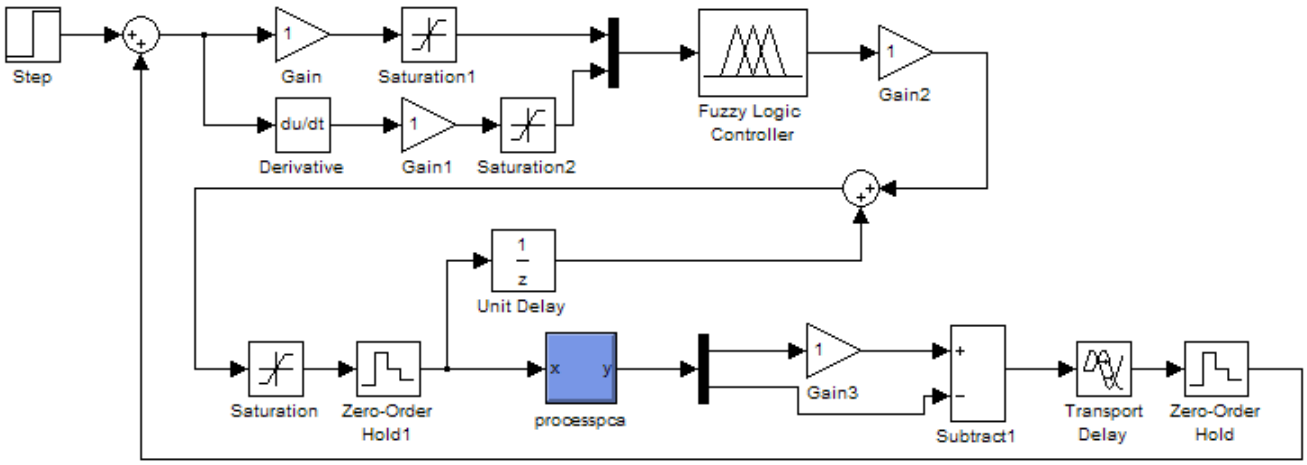

Fig. 1 NC machining adaptive control model based on fuzz theory

3. Machining Parameters Adaptive Control Visualization

3.1 Fuzzy control algorithm

According to the fuzzy control theory, the fuzzy set domain was divided into 3 for the input language variable E_I , EC_I and the output variables U_{a_f} . The values range of the current deviation was E_I = [-e , +e], the values range of the deviation change rate was EC_I = [-$\dot{e}$, $\dot{e}$], quantization factor $k_e = k_{ec} = 3/e$. To reduce the computational complexity, accelerate response speed, it selected the triangle function as the membership functions. Thus, according to the relation of the decision and the target, it established 49 fuzzy control rules. Based on the fuzzy set of input language variable $\tilde{E}$, $\tilde{EC}$ and fuzzy control rules, it received fuzzy set of the output language variable:

$$\tilde{U}_{af} = \left(\tilde{E} \times \tilde{EC} \right) \circ R \tag{2}$$

Where R was fuzzy relation array.

First, according to the 49 fuzzy control rules, it computed the relation array of every rule:

$$R_i = \left(\tilde{E} \times \tilde{EC} \right)^{T_1} \times \tilde{U}_{af} \tag{3}$$

And get the R using the $R = R_1 \vee R_2 \vee \cdots \vee R_{49}$. Second, based on the $\tilde{U}_{af} = \left(\tilde{E} \times \tilde{EC} \right)^{T_2} \circ R$, it supposed the

$\tilde{E} = \frac{1}{-6} + \frac{0.5}{-5}, \tilde{EC} = \frac{0.1}{-1} + \frac{0.5}{2} + \frac{1}{4}$, $R = \begin{bmatrix} 0.5 & 0.5 & 0.5 \\ 0.5 & 1 & 0.5 \\ 0.5 & 0.5 & 0.5 \\ 0.5 & 0.5 & 0.5 \\ 0.5 & 0.5 & 0.5 \\ 0.5 & 0.5 & 0.5 \end{bmatrix}$, And get

$$\tilde{E} \times \tilde{EC} = \begin{bmatrix} 1 \\ 0.5 \end{bmatrix} \begin{bmatrix} 0.1 & 0.5 & 1 \end{bmatrix} = \begin{bmatrix} 0.1 & 0.5 & 1 \\ 0.1 & 0.5 & 0.5 \end{bmatrix} \tag{4}$$

$$\tilde{U}_{af} = \left(\tilde{E} \times \tilde{EC} \right)^{T_2} \circ R = [0.1 \quad 0.5 \quad 1 \quad 0.1 \quad 0.5 \quad 0.5] \circ \begin{bmatrix} 0.5 & 0.5 & 0.5 \\ 0.5 & 1 & 0.5 \\ 0.5 & 0.5 & 0.5 \\ 0.5 & 0.5 & 0.5 \\ 0.5 & 0.5 & 0.5 \\ 0.5 & 0.5 & 0.5 \end{bmatrix} = \begin{bmatrix} 0.5 & 0.5 & 0.5 \end{bmatrix} \tag{5}$$

$$\Delta a_f = \frac{\sum_{i}^{13} x_i \mu_{\tilde{u}_{a_f}^L}(x_i)}{\sum_{i}^{13} \mu_{\tilde{u}_{a_f}^L}(x_i)} \tag{6}$$

Where x_i was the fuzzy set of output language variable and $\mu_{\tilde{u}_{a_f}^L}(x_i)$ was the membership functions of output language variable [15].

3.2 Visualization program realization

To facilitate the programming, based on the algorithm of fuzzy control, the system parameter calculation flow chart is established, shown in Figure 2. According to the test bench parameters, it took the current limit to 18 A, the speed limit for 1500 mm/min. And the actual values range of the current deviation was $E_I = [-18,18]$, the actual values range of the deviation change rate was $EC_I = [-36,36]$. The program running results as shown in Table 1. Which, when the current deviation was -18 A, deviation rate was -36 A, the output to feed rate change value was 1500 $mm/\min$, and in line with the fuzzy rules. Practically analyzing, when the feed rate suddenly decreased, the current became so. And through the fuzzy control, it could create bigger feed rate to compensate the former. So through the adaptive adjustment of feed rate, the adjustment of the current is achieved. When the feed rate in the procedures of system executing changed, through adaptive control, make it

changes to the predetermined value slowly. It can reduce the impact to the machine brought from the mutation, and enhance system stability.

Based on visual C++ programming software and the fuzzy controller embedded the source program into the existing TDNC-H8 system to realize the dynamic display of the adaptive control process [16]. And the validity of fuzzy controller and the intelligent control functions of system are verified. By the relationship between feed rate and current, the load ration F = actual current/ rated current (%) is displayed as the ultimate display parameters. Because the system adaptive control process is dynamic, the screenshots can not display the dynamic effect, only the static results. Nevertheless, it can be seen that when the feed rate F changed suddenly, the system current realized smoothly adaptive adjustment under the action of fuzzy control strategy. And this process only took a few seconds. But it reduced the impact on machine, realized the optimization control of machining process, shown in Figure 3.

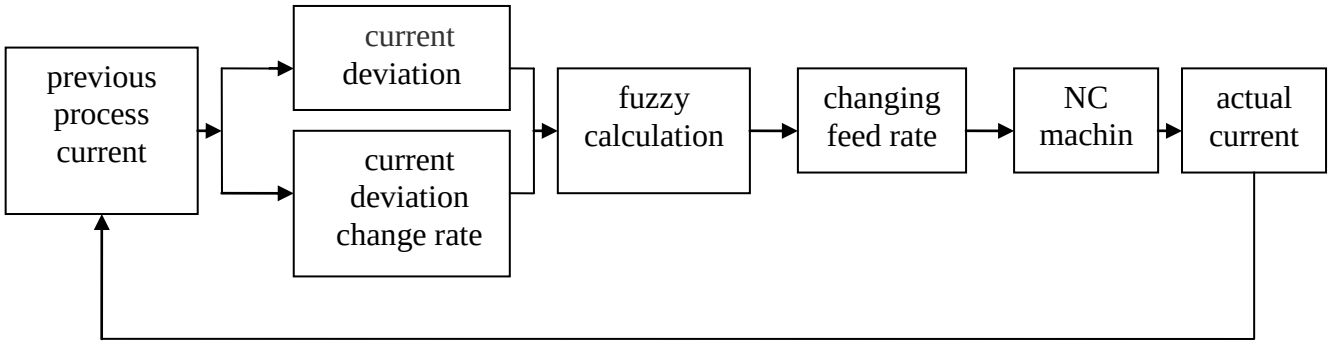

Fig. 2 Parameter calculation process

Table 1 Running results

Δa_f（mm/min） \ EC_I（A）	-36	-24	-12	0	12	24	36
-18	1500	1500	1000	1000	500	0	0
-12	1500	1500	1000	500	500	0	-500
-6	1500	1000	1000	500	0	-500	-500
0	1000	1000	500	0	-500	-1000	-1000
6	500	500	0	-500	-500	-1000	-1500
12	500	0	-500	-1000	-1000	-1000	-1500
18	0	0	-1000	-1000	-1000	-1500	-1500

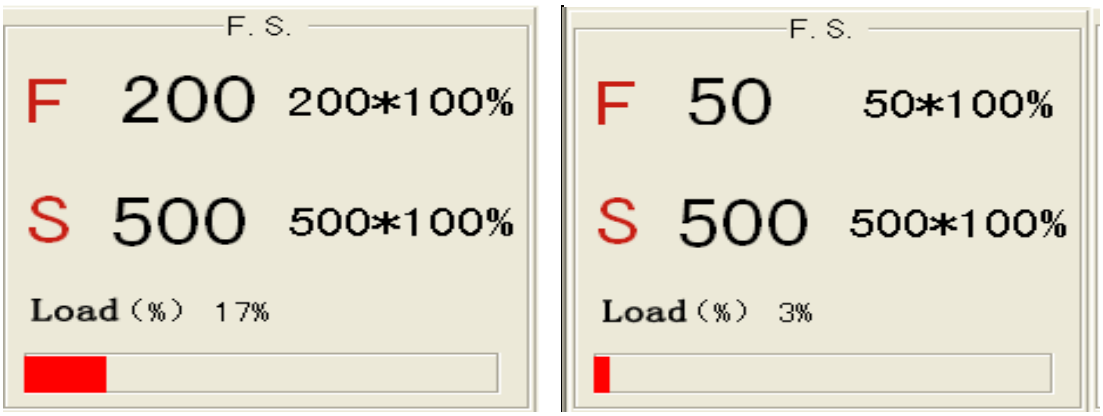

Fig. 3 Adaptive control process

4. Conclusion

The selection of NC cutting parameters is a key element in the machining process, which directly affects the efficiency and accuracy of processing. Based on the impact on the system brought from the different procedure and different parameter settings in the NC machining process, using the fuzzy control theory, the processing parameters adaptive control is achieved. Using the fuzzy adaptive control model is established for NC machining systems. And the intelligent control dynamic display of the process is achieved based on the visualization capability of VC. The results showed that the fuzzy adaptive control system could achieve the intelligent control requirements of high identification and control accuracy, reduced the machine impact brought from changing parameter, made the process more smoothly, improved the machining stability and accuracy.

Acknowledgment

The authors would like to thank the anonymous reviewers for their useful comments and suggestions. And this work was supported in part by National Natural Science Foundation of China (Grant No.50975193), and Doctoral Foundation of the Ministry of Education in 2010(Grant No.20100032110006),and Tianjin Science and Technology Project(Grant No.11zckfgx03400). Please communicate with the corresponding author Taiyong Wang, if there are any questions in this paper.

References

[1] S. Jiang. Research on NC Cutting Parameter Optimum Matching Expert System, *Tongji University Master's degree paper*, pp. 1-2, 2002.

[2] L. Gao, Y.Yang and X.Y Li. Research and Development of Optimization of NC Machining Parameters, *DIGITAL MANUFACTURING*, No. 22, pp. 48-51, 2010.

[3] Y.Z Zhang. Optimization of Cutting Parameters Based on Fuzzy Analysis Method, *Journal of Hunan University of Science &Technology (Natural Science Edition)*,Vol. 24, No. 4, pp. 39-43, 2009.

[4] H. Huang, A.P Li and X.K Lin. Fuzzy Control System for Milling Machining, *JOURNAL OF TONGJI UNIVERSITY(NATURAI， SCIENCE)*, Vol. 36, No. 7, pp. 956-961, 2008.

[5] Z. Kasirolvalad, M.R.Jahed Motlagh and M.A.Shadmani. An Intelligent Modular Modeling Approach for Quality Control of CNC Machines Product Using Adaptive Fuzzy Petri Nets, *8th International Conference on Control, Automation Robotics and Vision*, pp. 1342-1347, IEEE xplore, December 6-9, 2004, Kunming, China.

[6] S.N Huang, Kok Kiong Tan, Geok Soon Hong, et al. Cutting Force Control of Milling Machine, *Mechatronics*, Vol.17, No. 10, pp. 533-541,2007.

[7] P.C Tseng, A. Chou. The Intelligent On-line Monitoring of End Milling, *International Journal of Machine Tools & Manufacture*, Vol.42, No. 1, pp. 89-97, 2002.

[8] C.G Xu, X.Y Wang, J.S Xing, et al. Multi-Sensor Intelligent System for On-Line and Real-Time Monitoring Tool Cutting State in FMS, *Journal of Beijing Institute of Technology*, Vol. 6, No.3, pp. 258-266,1997.

[9] Q.S Pang, S.G Xiao and M.M Song. Model Reference Adaptive Control of Numerical Control Machine Tool Machining Process, *Machine Tool & Hydraulics*, Vol. 37, No. 3, pp. 53-55, 2009.

[10] DONG S. YUN and GI J. JEON. Feed Rate Control of CNC Machines by Inverse Mapping Method, *Proceedings of the 15th IEEE International Symposium on Intelligent Control*, pp. 279-284, July 17-19, 2000, University of Patras, Rio Patras, Greece.

[11] Kaan Erkorkmaz, Yusuf Altintas. High Speed CNC System Design, Part III: high speed tracking and contouring control of feed drives, *International Journal of Machine Tools & Manufacture*, No.41, 1637-1658, 2001.

[12] S.G Hu. Research on Technology of Building Open CNC System with Intelligent Characteristic, Tianjin University Doctor's degree paper, pp. 79-88, 2008.

[13] Y.S Tang, H.Y. Chuang and W.T. Hu. Intelligent Cross-coupled Fuzzy Feed Rate Controller Design for CNC Machine Tools based on Genetic Algorithms, *International Journal of Machine Tools & Manufacture*, No. 39, pp.1673-1692, 1999.

[14] Sungchul Jee a, Yoram Koren. Adaptive Fuzzy Logic Controller for Feed Drives of a CNC Machine Tool, *Mechatronics*, Vol. 14, No.3, 299-326, 2004.

[15] W.G Zhang. *The Theory and Application of Fuzzy Control*, Northwestern Polytechnic University Press, 1999.

[16] X.B Ma, Z.Y Han, Y.Z Wang, et al. Development of a PC-based Open Architecture Software-CNC System, *Chinese Journal of Aeronautics*, Vol.20, No.3,pp. 272-281, 2007.

International Journal of Comprehensive Engineering
Part B, 2(4), 300-309, 2013
Doi: 10.14270/IJCE2013.2.4.b300
Regular paper

ISSN 2186-2680
e-ISSN 2186-2656
www.iace-journal.org

Integrating Particle Swarm Optimization and Least Squares for Regression Rules Extraction from Neural Network

Jianguo Wang [1], Wenxing Zhang [1,#], Bin Yang [1], Wei Shi [1] and Bin Yang [2]

[1] School of Mechanical Engineering, Inner Mongolia University of Science and Technology, Baotou, 014010, China
[2] National Center for Materials Service Safety, University of Science and Technology Beijing, Beijing 100083, China

[#] Corresponding author: manifold@imust.cn; Tel.: +86-0472-5951574; Fax: +86-0472-5951574

Abstract: The issue of how to add transparency to artificial neural networks (ANNs) becomes more critical in machine learning. Rules extraction from neural network is well recognized to be an effective solution to dealing with this problem. This study focus on regression problems and aims to develop an algorithm to extract regression rules from ANNs. In order to extract a set of comprehensible and accurate regression rules, the intelligent algorithm of particle swarm optimization (PSO) is introduced in this paper. The main concepts are that use enough linear segments to approximate the nonlinear activation function of each hidden unit and replace them by integrating PSO and Least Squares (LS), where the PSO algorithm is applied to seek more linear segments and each linear segment is approximated by LS algorithm, then use the decision tree to generate regression rules from the approximated ANNs. The extracted linear regression rules not only ensure the accuracy but also enhance the explanation. Experiments on two benchmark datasets show that the proposed approach is more accurate than the existing approaches based on the decision tree or linear regression. Furthermore, the proposed algorithm can also be treated as an efficient algorithm for functions approximation with linear segments.

Keywords: Artificial Neural Networks, Rules Extraction, Particle Swarm Optimization, Least Squares, Linear Segments.

Received: May 3,2012 / Accepted: Aug. 12,2013 / Published: Nov. 15,2013

1. Introduction

Artificial neural network has been successfully applied to solve a variety of application problems including classification and regression thanks to its powerful capability of nonlinear mapping and knowledge generalizing. However, its further development is restricted by its characteristic of "black box" because the knowledge learned by ANN is a set of numerical weights and connections that provide no direct clues as to what the relationship is between inputs and outputs. It is difficult to give an explicit explanation for the reasoning process of trained neural networks [1-3]. Predictions from a multiple linear regression (MLR) equation are easy to understand but not accurate. Therefore many researchers are focusing on the issue of extracting knowledge from trained neural networks in order to gain a better understanding of the network's solution, where the most attractive solution is to extract symbolic rules from trained neural networks for classification [4]-[8], quite a few algorithms have been done to solve the regression problems which are widely exist in many applications.

The traditional approach of MLR in the form of $Y = f(x)$, where $f(x)$ is either a constant or a linear function of x, that have a good explanation, but cannot solve the nonlinear problems accurately. Recently, some approaches are proposed that apply the piecewise linear (PWL) function to solve the nonlinear problems, such as three-piece and five-piece linear functions. Setiono et al. have proposed two approaches of regression rules extraction from neural network take the form: if (conditions are satisfied), then predict $Y = f(x)$, where the conditions are described by input attributes [9,10]. The common ground of them is using the PWL function

to approximate the nonlinear hidden unit activation function and dividing the input space of the data into sub-regions, then applying C4.5 [11] to extract corresponding rules from the PWL function. In REFANN (Rule Extraction from function Approximating Neural Network) algorithm [9], the PWL function is approximated based on the maximum value of absolute weighted inputs, which is treated as the tangent point of linear segment, the other values are discarded. In algorithm [10], the PWL function is used to approximate the hidden unit activation function by minimizing the sum of squared errors computed from training data samples. However, the number of the linear segments is limited to less than five due to the cut-off points of PWL function are hard to find out in both algorithms, especially in the algorithm [10] where the PWL function consists of only three linear segments. Few linear segments mean poor approximation accuracy, which will affect the final accuracy of the regression rules. So the primary problem needs to be solved in regression rules extraction from neural network is how to improve the approximating accuracy with more linear segments currently.

In this paper, a novel algorithm of integrating PSO and LS for regression rules extraction from neural network called PSOLS is proposed. We will apply PSOLS to generate more linear segments to approximate the hidden unit activation function and present the results of our empirical study in financial dividend events by applying REFANN and algorithm [10]. PSO is an evolutionary computation technique developed by Kennedy and Eberhart in 1995 [12-13], it has already been used to solve many optimization problems. The underlying motivation for the development of PSO algorithm was the social behavior of animals such as bird flocking, fish schooling, and swarm theory [14]. The LS algorithm is a standard approach to the approximate solution of linear equations, often used to generate estimators and other statistics in linear regression analysis. In order to extract the regression rules, we first set up a PWL function with 3, 5, 7 or 2n+1 linear segments and treat the cut-off points as the optimization problem, then apply PSO to find the best cut-off points and apply LS to calculate the slopes and intercepts. Finally, the C4.5 approach [11] is applied to generate the regression rules.

The organization of this paper is as follows. The section II describes neural network training and pruning. In section Ⅲ, we describe how the PWL function is generated by approximating the hidden unit activation function. Section Ⅳ shows how the regression rules are extracted from neural network. In section Ⅴ, we carry out two experiments to illustrate the process of rules extraction from neural network in detail. Finally, we make discussion and conclusion of this paper in section Ⅵ.

2. Network Training and Pruning

A fully connected three-layer feed-forward network is the base of the method. In this section we describe the neural network topology and how to be trained and pruned. The hyperbolic tangent function $\tanh(\xi)$ is used as the hidden unit activation function and the linear function $f(\xi)$ as the output unit activation function. So we just only need to liberalize the hidden unit activation function.

$$\tanh(\xi) = \frac{e^{\xi} - e^{-\xi}}{e^{\xi} + e^{-\xi}} \tag{1}$$

$$f(\xi) = \xi \tag{2}$$

Given an *n*-dimensional sample $x_{i,l}$, $i \in \{1,2,...,\mathrm{k}\}$ as input, where *k* is the number of the samples. Let $w_{m,l}$ be the connection weight from input unit *l*, $l \in \{1,2,...,\mathrm{n}\}$ to hidden unit *m*, $m \in \{1,2,...,\mathrm{h}\}$, v_m be the weight from hidden unit *m* to output unit, b_2 be the bias of output unit and $b_{1,m}$ be the bias of hidden unit *m*, the output Y_i of the network for input sample $\mathbf{X}_i$ is obtained by computing the below equation:

$$Y_i = f\left(\sum_{m=1}^{\mathrm{h}} \phi_m \cdot v_m + b_2\right) \tag{3}$$

where

$$\phi_m = \tanh\left(\sum_{l=1}^{\mathrm{n}} x_{i,l} \cdot w_{m,l} + b_{1,m}\right). \tag{4}$$

The Levenbberg-Marquardt approach is used to train network, which is regarded as the faster learning approach and has higher precision approximation than other back-propagation approaches [15].

In order to reduce the complexity of rules generation process and improve the comprehensible of the regression rules, the cross-validation [16] approach is used to prune the redundant inputs and hidden units. This approach is regularly used in comparing two or more learning models to estimate which model performs the best on the problem, and it is successfully used in optimizing the neural networks architecture [17-18].

3. Approximating Hidden Unit Activation Function

After pruning, the structure of network will become simpler, but it is still difficult to explain how the problems are solved, because the knowledge which reserved in the form of connection weights and the nonlinearity activation function. Therefore, we attempt to apply the PWL function to approximate the hidden unit activation function based on LS, and to extract the regression rules with the consequences of the rules are linear functions.

We set up a PWL function $L(\xi)$ according to the origin symmetry of the activation function, such as 5-piece linear segments function is depicted as below:

$$L(\xi)=\begin{cases} b_2+\beta_2\cdot\xi & if \quad \xi>\xi_2 \\ b_1+\beta_1\cdot\xi & if \quad \xi_2\geq\xi>\xi_1 \\ \beta_0\cdot\xi & if \quad -\xi_1\leq\xi\leq\xi_1 \\ -b_1+\beta_1\cdot\xi & if \quad -\xi_2\leq\xi<-\xi_1 \\ -b_2+\beta_2\cdot\xi & if \quad \xi<-\xi_2 \end{cases} \tag{5}$$

where $\xi_m^i=\mathbf{X}_i\cdot\mathbf{W}_m+b_{1,m}$, ξ_m^i is the weighted input of the activation function of the hidden unit *m* corresponding to the sample $\mathbf{X}_i$.

For the sake of minimizing the root mean square error (RMSE) between activation function and PWL function, the importance of approximating process is to find the cut-off points ξ_1,ξ_2, the slopes β_0, β_1, β_2 and the intercepts b_1, b_2 of each of the linear segments of the PWL function . The RMSE is treated as the fitness function of each particle for PSO algorithm.

$$\mathrm{RMSE}(\xi)=\sqrt{\frac{\sum_{i=1}^{k}\left(\tanh(\xi^i)-L(\xi^i)\right)^2}{k}} \tag{6}$$

The detailed steps of approximating the hidden activation function are as follows:

(1) For each hidden unit, finding out the maximum absolute value $\xi^{\max}$ in the weighted inputs, $\xi^{\max}=\max\left|\xi^1,\ldots,\xi^k\right|$, and initializing the dimension *D* and the number of the particles *N*, maximum iterations $I_{\max}$ and velocity $v_{\max}$, convergence accuracy *E*, the number of the linear segments *s*, $s\geq 3$, where the dimension *D* is determined by the number of linear segments, *D*= (s-1)/2, and initializing the position $\mathbf{P}$ and velocity $\mathbf{V}$ of the particle swarm as follows:

$$\mathbf{P}(t)=\begin{bmatrix} \xi_{1,1},\xi_{1,2},\ldots,\xi_{1,D} \\ \vdots \quad \ddots \quad \vdots \\ \xi_{N,1},\xi_{N,2},\ldots,\xi_{N,D} \end{bmatrix}_{N\times D}, \qquad \mathbf{V}(t)=\begin{bmatrix} v_{1,1},v_{1,2},\ldots,v_{1,D} \\ \vdots \quad \ddots \quad \vdots \\ v_{N,1},v_{N,1},\ldots,v_{N,D} \end{bmatrix}_{N\times D} \tag{7}$$

where $\xi_{i,j}$ is the cut-off point of PWL function, $0<\xi_{i,1}<\xi_{i,2}<\ldots<\xi_{i,D}<\xi^{\max}$ and $-v_{\max}\leq v_{i,j}\leq v_{\max}$, $i=1,2,\ldots,N$, $j=1,2,\ldots,D$. Each particle $\mathbf{P}_i(t)=[\xi_{i,1},\xi_{i,2},\ldots,\xi_{i,D}]$ is corresponding to a PWL function and *t* is the present iteration, $t=1,2,\ldots,I_{\max}$.

(2) For each particle $\mathbf{P}_i(t)$, splitting the weighted inputs into *s* subintervals: $[-\xi^{\max},-\xi_{i,D})$, $[-\xi_{i,D},-\xi_{i,D-1})$, … , $[-\xi_{i,1},\xi_{i,1}]$, … , $(\xi_{i,D-1},\xi_{i,D}]$, $(\xi_{i,D},\xi^{\max}]$, then finding out their corresponding input samples denoted by $\mathbf{A}^i_{-D}$, $\mathbf{A}^i_{-(D-1)}$, …, $\mathbf{A}_0$, …, $\mathbf{A}^i_{D-1}$, $\mathbf{A}^i_D$ sets and output samples denoted by $\mathbf{B}^i_{-D}$, $\mathbf{B}^i_{-(D-1)}$, …, $\mathbf{B}^i_0$, …, $\mathbf{B}^i_{D-1}$, $\mathbf{B}^i_D$ sets;

(3) According to the characteristic of origin symmetry of the hidden unit activation function, applying the LS approach to calculate the slopes β^i and the intercepts b^i of the PWL function $L_i(\xi)$ for each particle $\mathbf{P}_i(t)$;

$$\begin{cases} \begin{bmatrix} b_D^i \\ \beta_D^i \end{bmatrix} = \left(\begin{bmatrix} \mathbf{I} \\ \mathbf{A}_{-D}^i, \mathbf{A}_D^i \end{bmatrix} \cdot \begin{bmatrix} \mathbf{I} \\ \mathbf{A}_{-D}^i, \mathbf{A}_D^i \end{bmatrix}^T \right)^{-1} \cdot \begin{bmatrix} \mathbf{I} \\ \mathbf{A}_{-D}^i, \mathbf{A}_D^i \end{bmatrix} \cdot \left[\mathbf{B}_{-D}^i, \mathbf{B}_D^i \right] \\ \begin{bmatrix} b_{D-1}^i \\ \beta_{D-1}^i \end{bmatrix} = \left(\begin{bmatrix} \mathbf{I} \\ \mathbf{A}_{-(D-1)}^i, \mathbf{A}_{D-1}^i \end{bmatrix} \cdot \begin{bmatrix} \mathbf{I} \\ \mathbf{A}_{-(D-1)}^i, \mathbf{A}_{D-1}^i \end{bmatrix}^T \right)^{-1} \cdot \begin{bmatrix} \mathbf{I} \\ \mathbf{A}_{-(D-1)}^i, \mathbf{A}_{D-1}^i \end{bmatrix} \cdot \left[\mathbf{B}_{-(D-1)}^i, \mathbf{B}_{D-1}^i \right] \\ \vdots \\ \beta_0^i = \left(\mathbf{A}_0^i \cdot \mathbf{A}_0^{iT} \right)^{-1} \cdot \mathbf{A}_0^i \cdot \mathbf{B}_0^i \end{cases} \tag{8}$$

where **I** is the matrix of ones, *T* denotes transpose operator.

(4) Calculating the $\text{fitness}(\mathbf{P}_i(t)) = \text{RMSE}_i(\xi)$, then finding out the global position $\mathbf{P}_g$ and the local position $\mathbf{P}_l$. If the minimum fitness is less than the convergence accuracy *E* ($\text{fitness}_{\min} < E$) or the present iteration *t* achieves the maximum iteration $I_{\max}$ ($t = I_{\max}$), stop iterating, and choose the global position $\mathbf{P}_g$ as the best cut-off point set, calculate the final PWL function. Otherwise, go to next step;

(5) Renewing the position **P** and velocity **V** as follows:

$$\mathbf{V}(t+1) = \mathbf{V}(t) + c_1 \times \text{rand}() \times (\mathbf{P}_g - \mathbf{P}(t)) + c_2 \times \text{rand}() \times (\mathbf{P}_l - \mathbf{P}(t)) \tag{9}$$

$$\mathbf{P}(t+1) = \mathbf{P}(t) + \mathbf{V}(t+1) \tag{10}$$

where c_1, c_2 are two positive constants, rand() is a random function in the range [0,1].

(6) Let $t = t+1$, go to step 2.

The main concepts are that apply PSO to find out the optimal cut-off points and apply LS to approximate the hidden activation function with the base of the optimal cut-off points. The crucial advantage of this algorithm is that the more cut-off points can be offered if the more linear segments are required.

We make experiments that apply PSOLS algorithm to approximate the $\tan(\xi)$ function for $\xi \in [-4, 4]$ with 3, 5, and 7 linear segments respectively. The approximation results are depicted in Fig.1 (a)-(c). In order to perform the advantage of PSOLS, we make comparisons with REFANN and algorithm [10]. The approximation results of REFANN and algorithm [10] are depicted in Fig.2 (a) – (b) and Fig.3 respectively. Table 1 shows the detailed approximation results.

The results showed in Table 1 demonstrate that the PSOLS algorithm not only has higher approximation accuracy than REFANN and algorithm [10] in the same condition of 3 linear segments, but also can generate arbitrary number linear segments if need, where the REFANN algorithm can only general 5 linear segments at the most, and the algorithm [10] can general just only 3 linear segments.

Table 1 The detailed approximation results

Item	PSOLS			REFANN		Algorithm [10]
Linear segments	3	5	7	3	5	3
Cut-off points	$\xi_1 = 1.0822$	$\xi_1 = 0.7246$ $\xi_2 = 1.6143$	$\xi_1 = 0.5681$ $\xi_2 = 1.1492$ $\xi_3 = 1.9354$	$\xi_1 = 0.9952$	$\xi_1 = 0.6208$ $\xi_2 = 1.6205$	$\xi_1 = 0.9299$
Accuracy (RMSE)	**0.0318**	**0.0123**	**0.0065**	0.0771	0.0260	0.0684

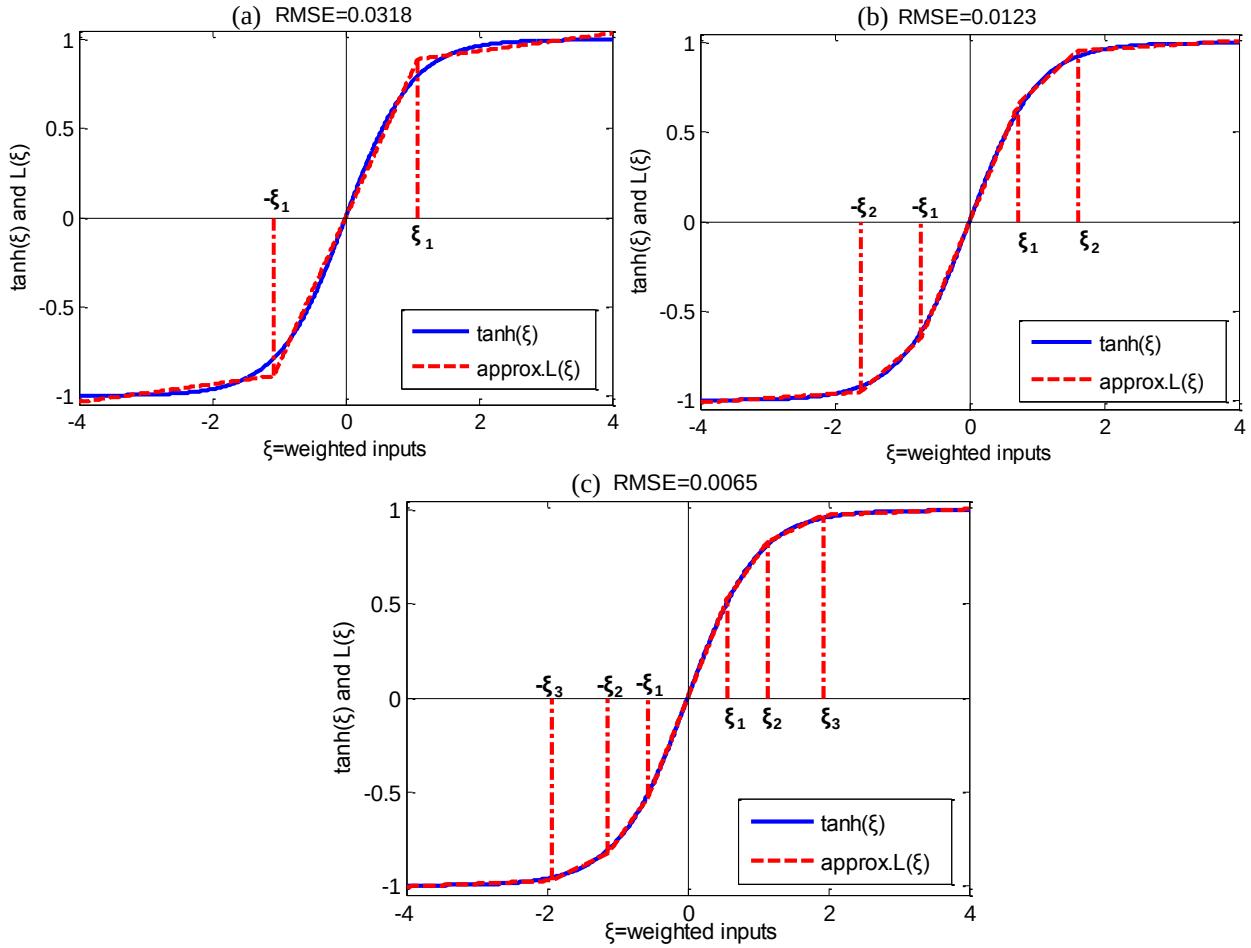

Fig. 1 Approximated by PSOLS with linear segments. (a) 3 linear segments and cut-off point $\xi_1 = 1.0822$. (b) 5 linear segments and cut-off point $\xi_1 = 0.7246$, $\xi_2 = 1.6143$. (c) 7 linear segments and cut-off point $\xi_1 = 0.5681$, $\xi_2 = 1.1492$, $\xi_3 = 1.9354$.

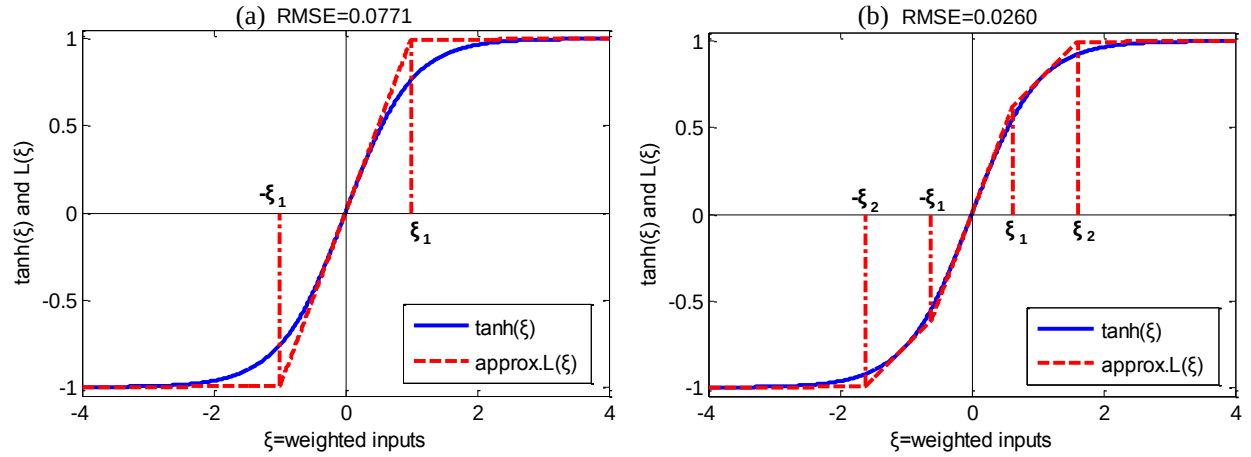

Fig. 2 Approximated by REFANN with linear segments. (a) 3 linear segments and the cut-off point $\xi_1 = 0.9952$. (b) 5 linear segments and the cut-off point $\xi_1 = 0.6208$, $\xi_2 = 1.6205$.

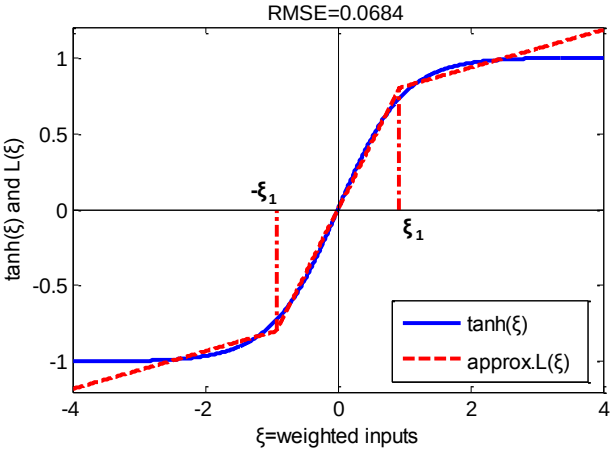

Fig. 3 Approximated by algorithm [10] with 3 linear segments and the cut-off point $\xi_1 = 0.9299$.

4. Extracting Regression Rules

For each hidden unit m, $m \in \{1,2,...,\mathrm{h}\}$, we apply $L_m(\xi)$ instead of $\tanh_m(\xi)$. Under this condition, the output Y_i of the network for input sample $\mathbf{X}_i$ can be calculated by the below Eq.(11) instead of Eq.(3):

$$Y_i = \sum_{m=1}^{\mathrm{h}} v_m \cdot L_m(\xi_m^i) + b_2 \tag{11}$$

For each PWL function $L_m(\xi)$, we use the cut-off points to divide the input space into several small sub-regions. Each linear segment corresponds to a sub-region, and is treated as a class label. Then the original input attributes of samples along with their corresponding class labels are given as input to C4.5 approach to generate a decision tree. Finally, the regression rules can be generated by tracing all paths from the root to the leaf nodes.

C4.5 builds decision trees from a set of training data, using the concept of information entropy. The training data is a set $S = s_1, s_2, \cdots$ of already classified samples. Each sample $s_i = x_1, x_2, \ldots$ is a vector where $x_1, x_2, \ldots$ represent attributes or features of the sample. The training data is augmented with a vector $C = c_1, c_2, \cdots$ where $c_1, c_2, \cdots$ represent the class to which each sample belongs. At each node of the tree, C4.5 chooses one attribute of the data that most effectively splits its set of samples into subsets enriched in one class or the other. Its criterion is the normalized information gain that results from choosing an attribute for splitting the data. The attribute with the highest normalized information gain is chosen to make the decision. The C4.5 algorithm then recurses on the smaller sublists.

5. Experiments and Comparisons

In this section, there present an experiment for testing PSOLS. The experimental data of Computer hardware come from the University of California at Irvine [19]. The parameters of the PSOLS are given as the following: the number of the linear segments $s = 7$, $c_1 = c_2 = 1.95$, the particles dimension *D*= (s-1)/2=3, the number of the particles $N = 30$, maximum iterations $I_{\max} = 200$, maximum velocity $v_{\max} = 3$, convergence accuracy $E = 0.001$. All the parameters are the best which determined by multiple tests.

Subsequently, in order to evaluate the experiment results and make comparisons with REFANN, algorithm[10] and MLR, the mean absolute error (MAE) and the relative mean absolute error (RMAE) are applied as follows:

$$\mathrm{MAE} = \frac{1}{\mathrm{k}} \sum_{i=1}^{\mathrm{k}} \left| T^i - Y^i \right| \tag{12}$$

$$\mathrm{RMAE} = \frac{1}{\mathrm{k}} \sum_{i=1}^{\mathrm{k}} \left| \left(T^i - Y^i \right) / \; T \right|^i \tag{13}$$

where T^i is the target value corresponding to the input sample $\mathbf{X}^i$.

We illuminate the process of regression rules extraction minutely in this experiment. The computer hardware dataset contains six continuous attributes described as: MYCT, MMIN, MMAX, CACH, CHMIN, and CHMAX. The goal is to predict the CPU's relative performance based on the other computer characteristics. We divided the total 209 samples into training set and testing set as the same as REFANN and Algorithm [10], where 188 samples are regarded as training set and the others as testing set.

First the samples are normalized to [0, 1], the normalization approach is adopted as follows:

$$\bar{x}_{ij} = \frac{x_{ij} - \min(X_i)}{\max(X_i) - \min(X_i)} \tag{14}$$

The original structure of the neural network of 6-3-1 style is constructed. We apply five-fold cross-validation approach to prune the network. All samples are randomly divided into five equal and mutually exclusive portions. Training samples will be conducted on any four of the five portions. Testing samples will then be performed on the remaining part. As a result, five overlapping training samples are constructed and testing samples are also performed five times. The average testing prediction accuracy over all five portions is treated as the present condition performance. After cross-validation, one of the smallest network structures of 3-1-1 style depicted in Fig.4 is obtained with three input attributes: MMIN, MMAX, CACH and one hidden unit [9].

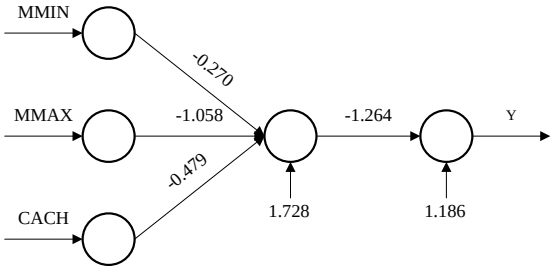

Fig.4 A pruned neural network structure.

In Fig.4, we can obtain the linear expression of the weighted input ξ of the hidden unit activation function as follows:

$$\xi = 1.728 - 0.270 \cdot MMIN - 1.058 \cdot MMAX \tag{15}$$

Meanwhile, we apply PSOLS to approximate the hidden unit activation function of the pruned network, and generate the slopes, intercepts and cut-off points as follows:

Slopes: $\beta_0 = 0.9531$, $\beta_1 = 0.5828$, $\beta_2 = 0.3213$, $\beta_3 = 0.1662$;

intercepts: $b_1 = 0.1877$, $b_2 = 0.4450$, $b_3 = 0.6547$;

cut-off points: $\xi_0 = -0.5153$, $\xi_1 = 0.9849$, $\xi_2 = 1.3308$.

Then the final approximated $L(\xi)$ can be obtained with 4 linear segments which are depicted in Eq.(16) (the other 3 linear segments contain no samples).

$$L(\xi) = \begin{cases} 0.9531\xi + 0.1877 & if \quad \xi \le -0.5153 \\ 0.5828\xi + 0.1877 & if \quad -0.5153 < \xi \le 0.9849 \\ 0.3213 \cdot \xi + 0.4450 & if \quad 0.9849 < \xi \le 1.3308 \\ 0.1662 \cdot \xi + 0.6547 & if \quad \xi > 1.3308 \end{cases} \tag{16}$$

The results of $L(\xi)$ approximating $\tanh(\xi)$ and the approximate errors $L(\xi) - \tanh(\xi)$ are depicted in Fig.5. In order to compare with REFANN and algorithm [10], we apply the two approaches to extract the regression rules from neural network, and the results of approximating are depicted in Fig.6 and Fig.7. The results of comparisons show that PSOLS has higher approximating accuracy with $\mathrm{RMSE} = 0.0018$.

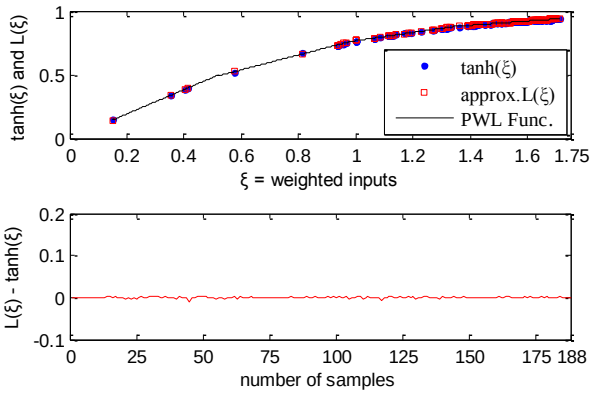

Fig.5 The approximating result of PSOLS.

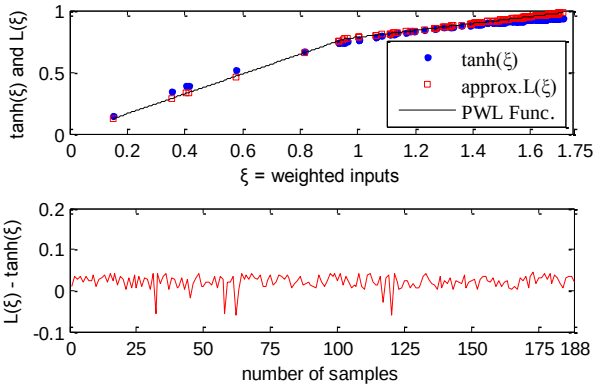

Fig.6 The approximating result of REFANN.

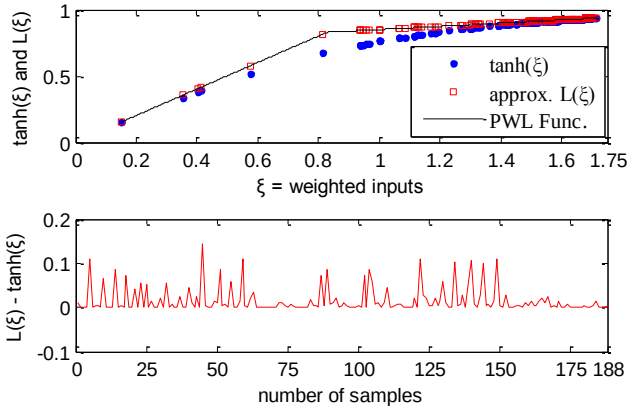

Fig. 7 The approximating result of Algorithm [10].

By applying $L(\xi)$ instead of $\tanh(\xi)$ approximately, we can obtain the linear expression of predicted output Y:

$$Y = -1.2641(\xi + 1) \quad (17)$$

Set ξ (Eq.(15)) and $L(\xi)$ (Eq.(16)) to Eq.(17), we can obtain a set of linear regression rules between input attributes and output attribute with the regions of ξ as the rule conditions:

Rule set A:
Rule 1: if $0 \le \xi \le 5153$, then $Y = y_1$
$y_1 = 3.2678 - 0.3252 \cdot \mathrm{MMIN} - 1.2746 \cdot \mathrm{MMAX} - 0.5770 \cdot \mathrm{CACH}$
Rule 2: if $0.5153 < \xi \le 0.9849$, then $Y = y_2$
$y_2 = 2.6962 - 0.1990 \cdot \mathrm{MMIN} - 0.7794 \cdot \mathrm{MMAX} - 0.3529 \cdot \mathrm{CACH}$
Rule 3: if $0.9849 < \xi \le 1.3308$, then $Y = y_3$
$y_3 = 2.4503 - 0.1097 \cdot \mathrm{MMIN} - 0.4296 \cdot \mathrm{MMAX} - 0.1945 \cdot \mathrm{CACH}$
Rule 4: if $\xi > 1.3308$, then $Y = y_4$
$y_4 = 2.3766 - 0.0568 \cdot \mathrm{MMIN} - 0.2222 \cdot \mathrm{MMAX} - 0.1006 \cdot \mathrm{CACH}$

According to the three regions of the weighted input ξ, we divide the input space into 4 subregions and treat each subregion as a class label. Then apply C4.5 approach to generate rules as below:

Rule set B:
Rule 1: If $\mathrm{MMAX} > 32000$, $\mathrm{MMIN} > 8000$, then $Y = y_1$
Rule 2: If $\mathrm{MMAX} > 32000$, $\mathrm{CACH} > 64$, $\mathrm{MMIN} \le 8000$, then $Y = y_1$
Rule 3: If $16000 < \mathrm{MMAX} \le 32000$, $\mathrm{CACH} > 64$, $\mathrm{MMIN} \le 8000$, then $Y = y_2$

Rule 4: If $16000 < \text{MMAX} \le 32000$, $\text{MMIN} > 8000$, then $Y = y_2$
Rule 5: If $\text{MMAX} \le 16000, \text{CACH} \le 32$, $\text{MMIN} > 8000$, then $Y = y_3$
Rule 6: If $\text{MMAX} \le 8000, \text{CACH} > 32$, $\text{MMIN} \le 256$, then $Y = y_3$
Rule 7: If $8000 < \text{MMAX} \le 16000, \text{CACH} > 32$, $\text{MMIN} \le 2000$, then $Y = y_3$
Rule 8: If $\text{MMAX} \le 16000, \text{CACH} > 32$, $\text{MMIN} > 2000$, then $Y = y_3$
Rule 9: If $\text{MMAX} > 16000, \text{CACH} \le 64$, $\text{MMIN} \le 8000$, then $Y = y_3$
Rule 10: If $\text{MMAX} \le 16000, \text{CACH} \le 32$, $\text{MMIN} \le 4000$, then $Y = y_4$
Rule 11: If $\text{MMAX} \le 8000, \text{CACH} > 32$, $256 < \text{MMIN} \le 2000$, then $Y = y_4$

In order to indicate the effectiveness of PSOLS, we make comparisons with REFANN, algorithm [10] and MLR in Table 2. The results show that the regression rules generated by our approach have higher predictive accuracy than the others.

Table 2 The detailed results of machine dataset

Algorithm		Training set			Testing set		
		RMSE	MAE	RMAE	RMSE	MAE	RMAE
Pruned network		0.0126	7.8666	0.0895	0.0071	6.9825	0.1005
PSOLS	Rule set A	0.0128	8.3193	0.1123	0.0024	7.3483	0.1272
	Rule set B	0.0128	8.3193	0.1123	0.0024	7.3483	0.1272
REFANN	Rule set A	0.0380	34.0599	1.1681	0.0299	29.9346	0.9859
	Rule set B	0.0411	34.6713	1.1956	0.0325	30.3521	1.0915
Algorithm [10]	Rule set A	0.0437	28.6795	0.1701	0.0479	26.6522	0.1878
	Rule set B	0.0462	29.1319	0.1796	0.0583	27.2230	0.1985
MLR		0.0453	36.314	0.6983	0.0314	32.879	0.6918

6. Discussion and Conclusions

Briefly, regression rules extraction can improve the transparency of neural network, the key problem of which is that apply the PWL function to approximate the hidden unit activation function and replace it. The approximation accuracy will affect the final regression rules accuracy greatly, so higher approximation accuracy is the pursuing goal in this paper. REFANN, algorithm [10] are as the earliest method, which can generate a set of comprehensible regression rules, but the accuracy of the regression rules is not good enough for prediction. The problem is lower approximating accuracy, which is restricted by the few linear segments and the approximation algorithms. The proposed PSOLS focuses on pursuing more linear segments and effective approximation algorithm in order to improve the approximation accuracy. According to the experiments in section III, we can find that the LS algorithm has higher approximation accuracy than REFANN, algorithm [10] in the same condition of 3 linear segments. Furthermore, integrating the swarm intelligent algorithm PSO, we can easily obtain more linear segments to improve the approximation accuracy. So it is helpful for obtaining higher accuracy regression rules than the two algorithms, experiments have demonstrated that our approach is effective and superior. In addition, The PSPLS is suitable for not only the hyperbolic tangent function $\tanh(\xi)$, but also other nonlinear functions.

Acknowledgment

Helpful suggestions of Professor Yang Jian-hong, Dr He Fei of University of Science and Technology Beijing are gratefully acknowledged. This research is supported in part by the National Natural Science Foundation of China (No. 51005014), Natural Science of Foundation Inner Mongolia (No.2011ZD08), Intramural Foundation of Inner Mongolia University of Science and Technology (No. 2010NC032), Inner Mongolia High School Research Foundation (No.NJZY11150).

References

[1] F. Y Tzeng and K. L Ma. Opening the Black Box-Data Driven Visualization of Neural Networks, *In Proc of IEEE Visualization '05 Conf*, pp. 383-390, IEEE xplore, Oct 23-28, 2005, Minneapolis, America.

[2] D. Olden and D. A Jackson. Illuminating the "Black Box": a Randomization Approach for Understanding Variable Contributions in Artificial Neural Networks, *Ecological Modelling*, Vol. 154, No. 1, pp. 135-150, 2002.

[3] S. H Yang, B. G Hu and P. H Courne`de. Structural Identifiability of Generalized Constraints Neural Network Models for Nonlinear Regression, *Neurocomputing*, Vol. 72, No. 1-3, pp. 392-400, 2008.

[4] R. Andrews , J. Diederich and A. B Tickle. Survey and Critique of Techniques for Extracting Rules from Trained Artificial Neural Networks, *Knowledge-Based Systems*, Vol. 8, No. 6, pp. 373-389, 1995.

[5] G. G Towell and J. W Shavlik. Knowledge-based Artificial Neural Networks, *Artificial Intelligence*, Vol. 70, No. 1-2, pp. 119-165, 1994.

[6] L. M Fu. Rule Generation from Neural Networks, *IEEE Transactions on Systems, Man and Cybernetics*, Vol. 24, No. 8, pp. 1114-1124, 1994.

[7] R. Setiono. Extracting Rules from Neural Networks by Pruning and Hidden-Unit Splitting, *Neural Computation*, Vol. 9, No. 1, pp. 205-225, 1997.

[8] J. G Wang, J. H Yang, W. X Zhang and J. W Xu. Rule Extraction from Artificial Neural Network with Optimized Activation Functions, *In Proc of Intelligent System & Knowledge Engineering '08 Conf*, pp. 873-879, IEEE xplore, Nov 17-19, 2008, Xiamen, China.

[9] R. Setiono, W. K Leow and J. M Zurada. Extraction of Rules from Artificial Neural Networks for Nonlinear Regression, *IEEE Transaction on Neural Networks*, Vol. 13, No. 3, pp. 564-577, 2002.

[10] R. Setiono and J. Y . L Thong. An Approach to Generate Rules from Neural Networks for Regression Problems, *European Journal of Operational Research*, Vol. 155, No. 1, pp. 239-250, 2004.

[11] Quinlan R. *C4.5: Programs of machine learning*, Morgan Kaufmann, 1993.

[12] J. Kennedy and R. Eberhart. Particle Swarm Optimization, *In Proc. IEEE Int. Conf. on Neural Networks*, pp. 1942-1948, IEEE xplore, Nov 27-Dec 01, 1995, Perth, Australia.

[13] R. Eberhart and J. Kennedy. A New Ooptimizer Using Particle Swarm Theory, *In Proc. 6th Int. Symposium on Micro Machine and Human Science*, pp. 39-43, IEEE xplore, Oct 4-6, 1995, Nagoya, Japan.

[14] Xie X F, et al. A Dissipative Particle Swarm Optimization, *In Proc. of the Evolutionary Computation*, pp.1456-1461, IEEE xplore, May 12-17, 2002, Honolulu, HI, America.

[15] M. T Hagan and M. B Menhaj. Training Feedforward Networks with the Marquardt Algorithm, *IEEE Transactions on Neural Networks*, Vol. 5, No. 6, pp. 989-993, 1994.

[16] M. Stone. Cross-Validatory Choice and Assessment of Statistical Predictions, *Journal of the Royal Statistical Society*, Vol. 36, No. 2, pp. 111-147, 1974.

[17] T. Andersen and T. Martinez. Cross Validation and MLP Architecture Selection, *In Proc of the International Joint Conf on Neural Networks*, pp. 1614-1619, IEEE xplore, July 10-16, 1991, Washington, DC, America.

[18] B. Schenker and M. Agarwal. Cross-Validated Structure Selection for Neural Networks, *Computers and Chemical Engineering*, Vol. 20, No. 2, pp. 175-186, 1996.

[19] University of California Irvine Machine Learning Repository, California Irvine. Available: http://archive.ics.uci.edu/ml/index.html

International Journal of Comprehensive Engineering
Part B, 2(4), 310-319, 2013
Doi: 10.14270/IJCE2013.2.4.b310
Regular paper

ISSN 2186-2680
e-ISSN 2186-2656
www.iace-journal.org

Study on Integral Method of Vibration Signal

Min Zhou [1], Liang Xu [2], Qingliang Zhao [2,#], Jianfeng Yang [2], Wenbin Liu [2], Huaqing Wang [2,#]

[1] China National Petroleum Corporation, Beijing, 100007, China
[2] Chemical Safety Engineering Research Center of the Ministry of Education, Beijing University of Chemical Technology, Beijing, 100029, China

Corresponding author: zhaoql@mail.buct.edu.cn, wanghq_buct@hotmail.com

Abstract: In metallurgy, chemical industry, machinery and other enterprises, the value of vibration in rotating machinery is measured by the acceleration sensor. Utilizing the integral and differential relation among displacement, velocity and acceleration, the velocity and displacement of the semaphore can be gotten through integral of the acceleration signal. The integral transform of the vibration signal can utilize hardware circuit integral, software numerical integral, and Fourier transform and Laplace transform differential theorem. Least square method can be used to eliminate trend term produced by integral transform, which could make the signal more accurate and reliable. The paper discusses the possibilities of using the least squares method to eliminate the trend term, design of hardware integral circuit, common methods of software numerical integral and Fourier transform methods. Finally, this paper analyzes various integral methods in detail by simulation and experiment, and provides an optimized design for vibration signal integration processing.

Keywords: Vibration Signal, Hardware Integral, Numerical Integral, Fourier Transform, Least Squares Method.

Received: May 23,2012 / Accepted: Aug. 12,2013 / Published: Nov. 15,2013

1. Introduction

In the metallurgical, chemical, mechanical and other enterprises, rotating machinery accounts for 80%. It includes generators, motors, turbines oxygen machine, blower, large rolling mills, etc. In numerous diagnostic techniques, vibration signal analysis provides a most profound understanding of machinery equipment. Moreover, since the rotating machinery equipment is prone to generating vibration forced by misalignment or external action, its size and installation quality have a direct relationship with the fault. Vibration analysis and measurement plays an important role in the diagnosis of rotating machinery.

Generally, acquisition of signal is often collected through vibration acceleration or speed sensor. In order to obtain the displacement of vibration signal, this paper should use the integral and differential relationship of acceleration, velocity and displacement. Namely, after integrating the acceleration signal once, we can acquire the velocity signal, the integral of which can derive the displacement signal. And then these signals can be converted among each other. In the actual measurement of signal, some minimal DC components often exist, which could cause trend items after integrating them. Therefore, this paper adopts the least squares method to eliminate trend items so as to calibrate the signals. This paper introduces integration methods of vibration signal, including hardware integral circuit, software numerical integral and conversion in time and frequency domain. Vibration signal integral issues are discussed, and the experiment of related method is simulated.

2. Integral Analysis of Vibration Signal

Vibration signal is popularly simplified as simple harmonic vibration in vibration test, which can be expressed as:

$$X(t) = A\sin(2\pi ft + \varphi) \tag{1}$$

Where, A represents the amplitude; f represents the vibration frequency, and φ represents the initial phase angle of vibration signal.

According to the value (amplitude, frequency, etc.) of vibration, it is necessary to use an appropriate measurement tool to measure the vibration signal in order to obtain more accurate information of the vibration signal. The vibration sensor is used to accurately measure the mechanical vibration (displacement, velocity, acceleration) of the object within the range of demand, converting them into electric signals, and outputting them to the corresponding processor (microcontroller, digital signal processor) for analysis and processing. Thereby, amplitude, phase and other parameters of the vibration can be obtained, which could provide the conditions for implementation of control. The units of measurement used in engineering practice and its application field include:

Displacement(P_k—P_k): for low frequency range, theoretically at 0.1 ~10000Hz, generally under 2kHz;

Velocity (R_{ms} , P_k): for middle frequency range, generally at 10~1000Hz;

Acceleration (P_k): for a wide range, at 10-20 KHz.

Using the differential and integral relationship of vibration displacement, speed and acceleration, these parameters can be measured. In order to facilitate understanding, this paper use the continuous function to represent the sampling signal, and it does not affect the analysis results. It supposes that $a(t)$ is acceleration measured by the acceleration sensor; therefore, after integrating the acceleration once, the velocity can be acquired:

$$v(t) = \int_0^t a(t)dt = v'(t) + v_0 \tag{2}$$

Through integrating the velocity once, the displacement could be acquired:

$$s(t) = \int_0^t v(t)dt = s'(t) + s_0 \tag{3}$$

Where, $a(t)$ is acceleration signal in continuous time domain; $v(t)$ is velocity signal in continuous time domain; $s(t)$ is continuous displacement signal; assuming that initial value $a_0=0$, $v_0=0$'; $v't$ is the original function of $v(t)$; v_0 is the initial velocity; $s'(t)$ is the original function of $s(t)$; s_0 is the initial displacement. Actual sampling acceleration vibration signal contains a certain DC component ε, i.e. $a(t)=a'(t)+\varepsilon$. Therefore, the above integral equation becomes:

$$v(t) = \int_0^t a(t)dt = v'(t) + (\varepsilon t + \delta) + v_0 \tag{4}$$

$$s(t) = \int_0^t v(t)dt = s'(t) + (\frac{1}{2}\varepsilon t^2 + (\delta + v_0)t + \eta) + s_0 \tag{5}$$

Where, δ and η are the primary and secondary integral constant of DC component ε contained in acceleration vibration signal.

Tiny DC component ε accumulates in the time domain integral, so that velocity vibration signal contains a linear trend item after integral at primary time.

$$\varepsilon t + (\delta + v_0) \tag{6}$$

Similarly, displacement vibration signal contains a quadratic trend item after integrating acceleration vibration signal at secondary time.

$$\frac{1}{2}\varepsilon t^2 + (\delta + v_0)t + (\eta + s_0) \tag{7}$$

As seen from above integral relation, when using acceleration (or velocity) sensor to measure the vibration signal, it is necessary to make integral transformation in order to obtain the amount of displacement, initial phase angle and other parameters of the vibration signal [1]. Common integration method includes hardware integral method, software methods with digital integral, and the method using the conversion between time and

frequency domain. Ultimately, we can obtain amplitude, phase and other parameters of the vibration signal. In order to eliminate the impact of trend terms, they require to be calibrated after making the integral transformation. The least square method is commonly used to eliminate the trend term.

3. Least Squares Method

In the process of signal integration, owing to the effect of the DC bias and the trend term, it is necessary to remove the DC component and filter the signals. Generally, using the average of the acceleration vibration removes the DC bias before and after the integral. The least square method is used to eliminate integral vibration signal trend items, and the principle is shown as follows [2]:

Suppose sampling value of the vibration signal measured actually as $\{x_k\}$ ($k=1,2,3,\cdots,n$), let the sampling time interval Δt=1, set the polynomial function:

$$x_k^{'} = b_0 + b_1 k + b_2 k^2 + ... + b_m k^m \tag{8}$$

Where, k=1,2,3,...,n, The undetermined coefficient, b_j (j=0,1,2,...,m) of the function $x_k^{'}$, can be determined to make the square error sum of the function $x_k^{'}$ and discrete data x_k minimum, which is seeking extreme value,

$$E = \sum_{k=1}^{n} (x'_k - x_k)^2 = \sum_{k=1}^{n} (\sum_{j=0}^{m} b_j k^j - x_k)^2 \tag{9}$$

Using partial derivative to get extreme, the conditions that E has an extreme are followed:

$$\frac{\partial E}{\partial b_i} = 2\sum_{k=1}^{n} k^i (\sum_{j=0}^{m} b_j k^j - x_k) = 0 \tag{10}$$

Where, i=0,1,2,...,m. Demanding E on b_i partial derivatives in turn, m +1 linear equations could be gotten:

$$\sum_{k=1}^{n} \sum_{j=0}^{m} b_j k^{j+1} - \sum_{k=1}^{n} x_k k^j = 0 \tag{11}$$

Solving the equations, (m+1) undetermined coefficients could be obtained. In the above formula, m is polynomial orders supposed, its value range is $0 \le j \le m$. In the above Eq.11, When m=0, the trend term is arithmetic mean of sampling data of signal. When m=1, it is linear trend term. When $m \ge 2$, it becomes curve trend term. In actual vibration data processing, the value of m is usually chosen according to actual situation. Then the sampled data is processed to eliminate the multinomial trend term.

4. Hardware integral

Hardware integral of vibration signal is a kind of integral transformation which realizes through hardware circuit. Based on the integrated operational amplifier with resistors and capacitors in the feed back loop, hardware circuit can be accomplished to finish integral transformation. Circuit diagrams of integrating circuit have been regularly used, as follows [3]:

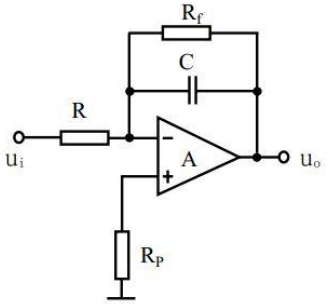

Fig. 1 Common integral circuit

4.1 Circuit Analysis

For the actual integrator, the gain and bandwidth of the operational amplifier is limited. By the circuit of Fig. 1, the transfer function of output voltage is as follows:

$$U_O = -\frac{U_i}{sT_1} \times \frac{1}{1+\frac{1}{sT_C}} \times \frac{1}{1+\frac{1}{sA_{uo}T_t}} \times \frac{1}{1+sT_1} \tag{12}$$

Where, $T_1 = RC$, $T_c = R_f C$, $T_t = \frac{1}{\omega_1}$, $\omega_1 = A_{uo}\omega_0$; T_1 is time constant of the integrating circuit; T_c is the time constant formed by current leakage current; ω_0 is angular frequency of the main pole in the operational amplifier; A_{uo} is the dc open-loop gain of the operational amplifier.

The above formula is the product of four factors. The first factor represents the relationship between output voltage and input voltage of the ideal integrator. The second and third factor represent low-frequency errors caused by leakage current and finite gain of the operational amplifier. The fourth factor represents high frequency error caused by finite bandwidth of operational amplifier.

Fig.1 shows that the output voltage U_o is the integration output of input voltage U_i. The relationship is as follows:

$$U_o = -\frac{1}{\tau}\int U_i dt \tag{13}$$

Where, $\tau=RC$ is a time constant, which is related to operational amplifier and integration time. When designing, τ is generally greater than 10 times pulse width.

R_f is the leak resistance of the integration drifting, which can prevent the saturation or cutoff phenomenon caused by integration drifting. For the purpose of reducing error, it requires $R_f \geq 10R$, and in order to reduce the influence of operational amplifier parameter on output voltage, we should choose: integrated operational amplifier with small input disorderly coupled parameter (U_{IO}, I_{IO}, I_B), large open loop gain A_{uo}, large gain-bandwidth product, and high input resistance.

4.2 Multisim Simulation

We make simulation by hardware integration circuit. The schematic of simulation circuit as follows [4]:

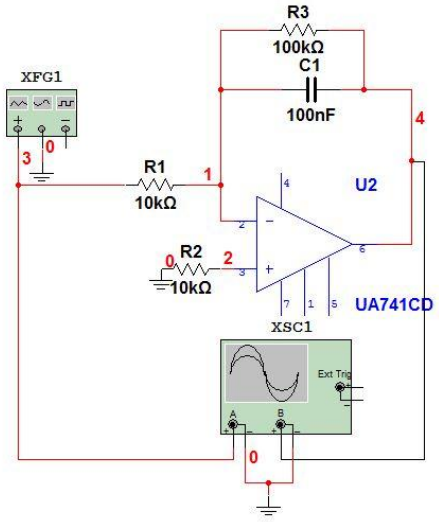

Fig. 2 Simulation schematic of hardware integration circuit

The input signal is the sinusoidal signal with amplitude 5V and 100Hz. From the circuit diagram, it can be seen that the time constant of the integrating circuit is $\tau = RC = 10K \times 100n = 1ms$. According to the integral calculation Eq.12, the circuit output signal is as follows:

$$U_O = -\frac{1}{1ms}\int 5\sin(628t)dt = 7.95\cos(628t)$$

The simulation waveform is shown in the following figure:

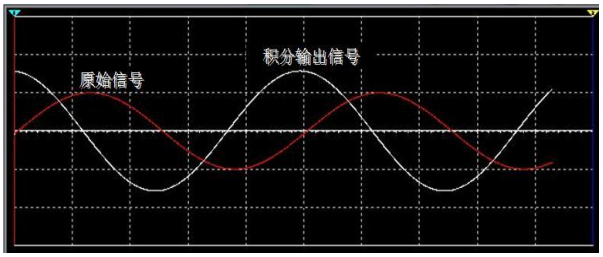

Fig. 3 Waveform of hardware integration circuit simulation

As can be seen from the integrator waveform, there is little difference between simulation results and theoretical calculations. The signal phase after integration shows about 90 °ahead and amplitude increases.

It will bring some error as a result of the integration operation used by hardware combinational circuit. When input voltage U_i is zero, the circuit will be under the influence of input offset voltage and input offset current of op amp. There will be zero-drift voltage in the output of integral circuit, and this voltage will change with time, which is called integral drift. The open-loop gain of an actual operational amplifier is not infinite, but a finite value. The input resistance R_{id} of operational amplifier is not infinite, which will also cause some error of output voltage. Input voltage reduces the open loop gain of an operational amplifier, and increases the relative error of the output voltage of integration circuit.

The effects of input resistance R_{id} can be ignored when $R_{id} \gg R$. The leakage resistance R_c of integration capacitor seriously influences the output voltage of integration circuit. Accordingly, it's necessary to choose capacitance with small leakage and good quality for the purpose of improving arithmetic accuracy of the integration circuit. The limited bandwidth of the operational amplifier will affect the transmission characteristics of the integrator circuit, which makes the output voltage of the integrating circuit produce a certain time lag. The narrower the bandwidth of the operational amplifier is, the more serious the phenomenon is. In order to reduce the times of time lag phenomena, it's necessary to choose the operational amplifier with larger gain bandwidth product.

As the above factors, there are some errors when used hardware integration circuit. Meantime, because measurement signal itself is not large, and hardware circuit elements have many errors, the accuracy of the measurement results will be seriously influenced. So it can reduce the amount of unnecessary errors to choose high-performance components when using hardware integration circuit.

5. Numerical Integration

From the above analysis, the result of hardware integration is subject to circuit constraints, whose flexibility is not high enough for signal analysis, and whose adaptation range is limited. Thus, if the integral environment is changed, the circuit component value is changed. In contrast, numerical integration has some great advantages in flexibility. Integration process to signal by software programming reduces the system volume and avoids the error from hardware circuit, which is more convenient for changing integration conditions. Therefore, numerical integration is a common integration method in the process of vibration signal. The common numerical integration methods are Trapezoidal formula Simpson formula, Cotes formula, compound trapezoidal formula, compound Simpson formula, and so on[5].

5.1 Trapezoidal Integration

The mathematical expression of the trapezoidal integration is:

$$y(k) = \Delta t \sum_{i=1}^{k} \frac{x(i-1) + x(i)}{2} \tag{14}$$

Where, $k=0,1,2,\ldots N$, is the sampling number; Δt is the sampling time. By using the trapezoidal integration, the velocity formula is expressed as follows:

$$v(i) = v(i-1) + \Delta t \frac{a(i-1) + a(i)}{2} \tag{15}$$

The displacement formula is:

$$s(i) = s(i-1) + \Delta t \frac{v(i-1) + v(i)}{2} \tag{16}$$

Where, a is acceleration signal; v is velocity signal; s is displacement signal; Δt is the sampling time; $i=0,1,2,...N-1$, When $i-1$ is negative, the value of $v(i-1)$ and $a(i-1)$ is zero.

The trapezoidal formula error is:

$$R_T[x] = -\frac{(N\Delta t)^3}{12} x^{(2)}(\eta), 0 < \eta < N\Delta t \tag{17}$$

From the above remainder term, we can know that the algebraic accuracy of the trapezoidal integration is one.

5.2 Simpson Integration

The mathematics expression of the Simpson Integration is expressed as follows:

$$y(j) = \frac{1}{6} \sum_{j=1}^{t} (x_{j-1} + 4x_j + x_{j+1}) \Delta t \tag{18}$$

With Simpson Integration formula, the velocity signal is expressed as follows:

$$v(i) = v(i-1) + \frac{a(i-1) + 4a(i) + a(i+1)}{6} \Delta t \tag{19}$$

The displacement formula is:

$$s(i) = s(i-1) + \frac{v(i-1) + 4v(i) + v(i+1)}{6} \Delta t \tag{20}$$

Where, a is acceleration signal; v is velocity signal; s is displacement signal; Δt is the sampling time; $i = 0,1,2,\cdots,N$. When $i-1$ is negative, the value of $v(i-1)$ and $a(i-1)$ is zero.

The Simpson formula error is:

$$R_T[x] = -\frac{1}{90} (\frac{N\Delta t}{2})^5 x^{(4)}(\eta), 0 < \eta < N\Delta t \tag{21}$$

From the above remainder term, we can know that the algebraic accuracy of the Simpson Integration is 3.

5.3 Cotes Integration

Cotes formula is also known as Boolean formula, whose mathematical expression is as follows:

$$y(i) = \frac{\Delta t}{90} \sum_{j=1}^{t} (7x(i-2) + 32x(i-1) + 12x(i) + 32x(i+1) + 7x(+2)) \tag{22}$$

With Cotes Integration formula, the velocity signal is expressed as follows:

$$v(i) = v(i-1) + \frac{7a(i-2) + 32a(i-1)}{90} \Delta t + \frac{12a(i) + 32a(i+1) + 7a(i+2)}{90} \Delta t \tag{23}$$

The displacement formula is:

$$s(i) = s(i-1) + \frac{7s(i-2) + 32s(i-1)}{90}\Delta t + \frac{12s(i) + 32s(i+1) + 7s(i+2)}{90}\Delta t \tag{24}$$

The Cotes formula remainder term is:

$$R_C[x] = -\frac{8}{945}(\frac{N\Delta t}{4})^7 x^{(6)}(\eta), 0 < \eta < N\Delta t \tag{25}$$

From the above, we can know that the algebraic precision of Cotes formula is 5.

The above integration conversion shows that weak signal of velocity (or displacement) can be obtained through numerical integration of the signal measured by the acceleration sensor (speed sensor).

Because the integration interval gradually become larger, which also means the sampling points are multiplied, the above three numerical integration methods that frequently used have gradually increased calculation accuracy.

When we need more precise calculus, for the purpose of avoiding high-level quadrature calculation, we can adopt multiple-trapezoid formula and multiple- Simpson formula, etc. It adopts low-level quadrature formula (trapezoidal or Simpson) in each inter-cell after dividing integration into several equal intervals, and then gets integral integration results by using the addition of the integration interval.

5.4 MATLAB Simulation

In order to simulation, the acceleration signal $x = 10 \times \sin(100\pi t) + 0.1$ is constructed. This signal contains a DC component, which is 0.1. The original signal diagram by Simpson numerical integral is as follows [6]:

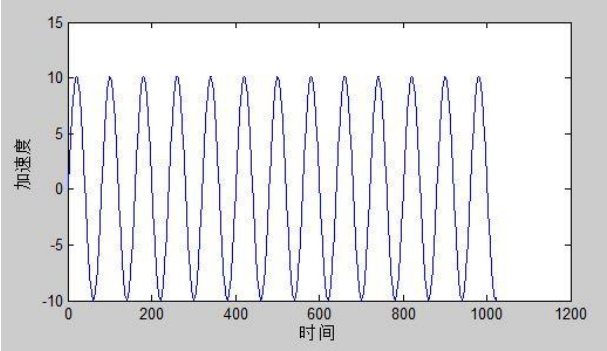

Fig. 4 Waveform of acceleration signal

The waveform of velocity signal after Simpson integration is as follows:

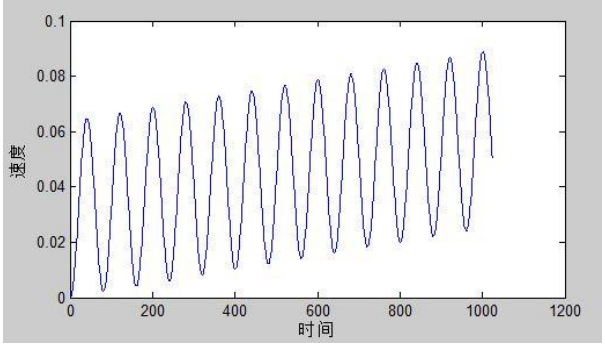

Fig. 5 Points after the speed signal

From the above chart, it could be seen that integrating the DC component produces a trend item. The main reason for contributing to the generation of the DC component is: first, the signal can't offset between the positive

and the negative after non-periodic sampling, and then we calculate the cumulative sum of the average after sampling, which results in error; second, it's because of the existence of the quantization and discrete error in A/D conversion process.

After the adoption of the method of least squares to eliminate the trend term of the speed signal, the velocity waveform is as follows:

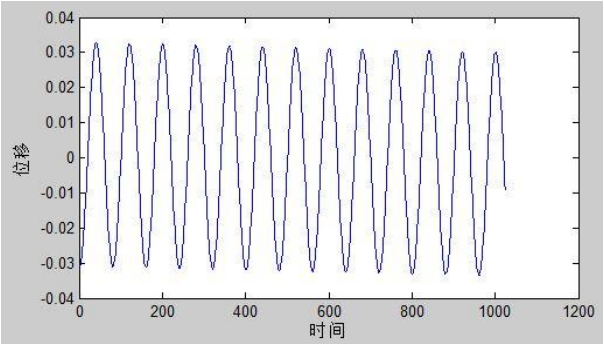

Fig. 6 Waveform after eliminate the DC component velocity

As shown in Fig.6, the waveform is offseted by using the least square method to eliminate time trend item. So it's feasible to use the least square method to eliminate time trend item in the signal.

6. Integration method based on the transformation between time domain and frequency domain

The Fourier analysis is a branch of mathematical analysis, which plays an important role not only in mathematics but also in engineering practice. Fourier analysis provides frequency domain analysis and combines time domain and frequency domain by transforming, which makes what the phenomenon and feature hidden in the time domain show in the frequency domain. FFT wins technician's favor because of its characteristics [7]. FFT evolves from the discrete Fourier transform (DFT), and solves the problem that the amount of computation of discrete Fourier transform (DFT) is huge.

Rotating machine vibration could be regarded as the stack of a series of harmonic vibration. According to formula (1), the vibration signal meets the conditions what a Fourier series require , and the Fourier series can be expressed as follows [8]:

$$X(t) = a_0 + \sum_{n=0}^{\infty}(a_n \cos \omega t + b_n \sin \omega t) \tag{26}$$

To discrete periodic vibration signal $x(t_k)$, $k = 0,1,\cdots,n-1$, the formulas of a_n, b_n are:

$$a_n = \frac{2}{N}\sum_{k=0}^{N-1} x(t_k)\cos\frac{2\pi nk}{N} \tag{27}$$

$$b_n = \frac{2}{N}\sum_{k=0}^{N-1} x(t_k)\sin\frac{2\pi nk}{N} \tag{28}$$

Where, *n=1,2,…,N/2*.

From the above equation, the amplitude and phase angle of measured vibration signal, gained by Fourier transform, are:

$$\text{Amplitude: } A_n = \sqrt{a_n^2 + b_n^2} \tag{29}$$

$$\text{Phase angle: } \varphi_n = \arctan\frac{b_n}{a_n} \tag{30}$$

This also means that the amplitude and phase angle of vibration signal can be gotten by the Fourier transform. When measuring the value of rotation mechanical vibration, its displacement signal is too weak to measure, and the signal value requires high in accuracy. So, in practice, we apply the relative relation of between derivation and integration among displacement, velocity and acceleration by measuring the acceleration signal or velocity of rotating machinery according to the rotating velocity and the strength of vibration signal, and then transform it from time domain to frequency domain to get vibration displacement.

The relative relation of between derivation and integral among displacement, velocity and acceleration is:

$$a(t) = \frac{dv(t)}{dt}, v(t) = \frac{dX(t)}{dt} \tag{31}$$

By differential nature of Laplace Transform, we could get: (assuming $v(0) = 0, X(0) = 0$)

$a(s) = sv(s)$

$v(s) = sX(s)$

And then, we can get:

$$v(s)\big|_{s=2j\pi f} = \frac{a(s)}{2j\pi f} = \frac{|a(2j\pi f)|}{2\pi f} \angle \arctan(a(2j\pi f)) - 90^{\circ} \tag{32}$$

$$X(s)\big|_{s=2j\pi f} = \frac{v(s)}{2j\pi f} = \frac{|v(2j\pi f)|}{2\pi f} \angle \arctan(v(2j\pi f)) - 90^{\circ} \tag{33}$$

Where, $s=j\omega=j2\pi f$, which is a complex parameters variable and named complex frequency. *a(s)* is an acceleration signal in frequency domain. *v(s)* is a velocity signal in frequency domain. *X(s)* is a displacement signal in frequency domain. *s* is a complex Laplace parameter

The value of acceleration *a(t)* could be gotten by measuring the vibration signal acceleration sensor, and get its amplitude and phase angle by the DFT / FFT. And then, the relevant parameters of displacement vibration signal could be obtained by use Eq. 30 and 31.

7. Conclusion

The acceleration (or velocity) signal needs integral transform in the practical measurement of vibration. This paper discusses three integral transform methods of the vibration signal and the need what the precise design to eliminate DC component of vibration signal and trend term in the process of soft integral such as numerical integration and Fourier transform requires. This paper proposes the detailed integral design method, so an appropriate method could be chosen to analyze and handle signals according to the actual situation of the project.

Acknowledgements

This project is supported by National Natural Science Foundation of China (Grant No.51075023), National Program on Key Basic Research Project (Grant No. 2012CB026000) and National Key Technologies R&D Program (Grant No. 2011BAK06B03-05).

References

[1] W. Z Chen, B. W Wang and X. Y Hu. Acceleration Signal Processing by Aumerical Integration, *Journal of Huazhong University of Science and Technology(Nature Science Edition)*, Vol. 38, No. 1, pp. 1-4, 2010.

[2] D. W LI, X. Y Xiong and B. Li. Research on the Processing of Vibration Acceleration Signal, *Mechanical & Electrical Engineering Technology*, Vol. 37, No. 07, pp. 50-52, 2008.

[3] Y. X Nie, X. G Yin and Z. Zhang. Some Discussions about Analogous Integrator Application, *Electronic Measurement Technology*, No. 3, pp. 3-6, 2000.

[4] X. X Zhang, J. Xu, X. Z Wang and Y. Y Yang. *Multisim10 Circuit Simulation and Applications*, Machinery Industry Press, 2010.

[5] C. F Ma, W. C Lin. *Modern Numerical Methods*, Science Press, 2011.

[6] H. D Liu, F. Zhu. *MATLAB Programming Fundamentals Typical Applications*, People's Posts and Telecommunications Press, 2008.

[7] J. Xu, X. J Yu. Vibration Signal Analysis Based FFT Algorithm, *Industrial Control Computer*, Vol.18, No. 12, pp. 8-9, 2005.

[8] P. Q Cheng. *Digital Signal Processing*, Tsinghua University Press , 2004.

International Journal of Comprehensive Engineering
Part C, 2(4), 320-325, 2013
Doi: 10.14270/IJCE2013.2.4.c320
Regular paper

ISSN 2186-2680
e-ISSN 2186-2656
www.iace-journal.org

Produce Bio-Boards Using Ulva Pertusa Kjellman and Zostera Marina

Hao Sun [1], Ke Li [2,#], Lixin Lu [1]

[1] School of Mechanical Engineering, Jiangnan University, 1800 Li Hu Avenue, Wuxi, Jiangsu Province, 214122, China

[2] Graduate School of Bioresources, Mie University, Tsu Kurimamachiya-cho 1577, 514-8507, Japan

[#] Corresponding author: dayanlv@live.cn; Tel.: +81-80-3672-1047; Fax: +81-592-319-592

Abstract: This study was carried out to investigate whether biomass materials which were produced using unused sea algae can substitute the oil-based plastic packaging material or wood material applied in packaging container. Three processes were carried to produce the biodegradable Ulva board which involves refining, compression molding and drying, and increased a process of defibrating to produce the biodegradable Zostera board. Mechanical properties evaluation of produced biodegradable bio-board show the rupture stress of Ulva board in the range of 15.56MPa to 49.55MPa, which is 1.3~4.1 times stronger in comparison with that of polystyrene plastic material used for food containers. Producing process of Zostera board is an appropriate technique and economizing on the producing time. Therefore, it is technically possible and propelling the packaging material forward.

Keywords: Biodegradable Packaging Materials, *Ulva pertusa Kjellman*, *Zostera Marina*, Bio-board, Rupture Stress.

Received: May 20,2012 / Accepted: Aug. 12,2013 / Published: Nov. 15,2013

1. Introduction

The eutrophication of seawater frequent mostly takes place in many seashores and estuaries along the outskirts of cities all over the world [1]. As a result, a huge amount of sea algae develop, and cause pollution and environmental degradation. One example of such Ulva pertusa Kjellman have been observed during summer and autumn in recent years. Unusual proliferation of such sea algae may induce the disruption of natural ecosystems, insufficient oxygen in the seabed, destruction of scenery and generation of an awful smell [2]. Shizuoka of Japan used a harvester to collect the algae for about 300,000 yen per ton, while salvaging it costs 100,000 ~ 200,000 yen [3, 4]. The other seaweed of Zostera Marina, which was proliferated 1332.8 g/m2 of dried Zostera every year [5]. The foliage of Zostera was withered in seawater, which returned the phosphorus, nitrogen and other eutrophic material back to the seawater. The Ulva pertusa Kjellman and Zostera develop and absorb of the eutrophic material, which were purified the sea water quality. So we need to collect the Ulva pertusa Kjellman and Zostera from seawater and found a using form for the unused algae. In recent years, this is an important subject in many countries.

Ulva pertusa Kjellman belongs to Chlorophyta. It attaches to submerged rocks, shells, pilings or other seaweed by a rhizoidal holdfast [6]. It is usually attached, but it is also found drifting with wide lobes of different lengths and a comparatively thin shoot. In detached specimens, it develops more holes, leading to a lacerated appearance [7]. Ulva pertusa Kjellman resource are now being used in food processing, fodder, fertilizers, soil improvement materials, cosmetics, seaweed glue, etc[8, 9].

Zostera marina, a monocot, is widespread and circumglobal in the Northern hemisphere, found throughout the north Atlantic and north Pacific and in the Mediterranean and Black Seas [10]. Zostera has long, bright green, ribbon-like leaves, about 1 cm wide [11]. The growth of Zostera could be purified the seawater quality, and dominate sandy and muddy sediments in coastal areas of low to moderate wave exposure [5]. However, Zostera

was withered in seawater by flowering and fruiting seasons, which returned the eutrophic materials back to the seawater. Stated thus, the best way is collect the Zostera by the life expectancy.

Ulva pertusa Kjellman is rich in fibers and it has fiber content similar to that of land plants, while the main substance is cellulose. There is a great deal of cellulose and hemicellulose in Ulva pertusa Kjellman, which are the main materials of this experiment. Zostera marina also contain fiber component similar to land plants, and the cellulose of Zostera is stronger than some land plants. The stalk and the leaf of Zostera marina are longer and contain rich high quality fiber [12]. The cellulose is hydrophilic, insoluble in water, highly resilient and impact resistant; hemicellulose has the function against deformed while used in material. It is highly adhesive and can be used in scientific research applications as well. At the same time, to strengthen the material, it dehydrates through pressurization and heating of the cellulose, and re-establishment of the connection between the cellulose caudal ends. Therefore, we can use the cellulose and hemicellulose contained in Ulva pertusa Kjellman or Zostera marina to re-connect the board materials.

The majority of culture media and food container in the present market are plastic. Due to the scarcity of petroleum resources and their poisonous effects on the environment, the substitute of the new environmentally friendly materials has lately attracted. The purpose of this study was to utilize Ulva pertusa Kjellman and Zostera to produce biodegradable boards. The process of producing biodegradable boards involves refining, defibrating, compression molding and drying. Self-bonding is the main factor of the algae. There is a possibility of using for culture media for plants, food and medical packaging, transportation packaging, culture pans, mulch film instead of petroleum plastic and wood materials. This study mainly focus on analyzing and compare the rupture stress of Ulva pertusa Kjellman and Zostera boards. The aims of this study are to determine the most optimum conditions of the bio-board production process with Ulva pertusa Kjellman and Zostera Marina.

2. Production of Bio-boards

Ulva pertusa Kjellman and Zostera Marina collected from the seaside of Ise Bay in Japan were used in experiment. The algae were repeatedly washed with pure water to remove mud, soils and other algae, dried in the shade at room temperature and the end stored in plastic bags. The moisture content of the dried algae in the experiment was approximately 10% w.b..

2.1 The Ulva pertusa Kjellman Bio-board

The flowcharts of the process for producing bio-boards of Ulva pertusa Kjellman are shown in Fig. 1. The dried Ulva was put in water for over 2 hours for restoration. Then the dried Ulva return to the same condition as the fresh Ulva. The restored Ulva and water were put into a mixer and refined for 1 min to make a piece of Ulva to a size within 6 mm. The long fibers were cut during refining, which made the macromolecule fibers into microfibers, exposed more active hydroxy groups and laid the foundation for physical adsorption. The compression mold is square with dimensions of 100 mm×100 mm×25 mm. In the case of difficult dehydration, there is an array of 7 mm×7 mm stomas 2 mm in diameter up and down both sides of the compression mold for dehydrate easily.

The mold is filled with Ulva pertusa Kjellman and a hot presser is used for compression. While preheating the mold and the material, pressure is gradually applied; when 0.2 MPa of pressure has been applied for 10 min, the preheating is done. During the hot compression, another connection opportunity is obtained since the moist Ulva pertusa Kjellman are primarily dehydrated, the water in the experimental material is pressed and the many exposed active hydroxyl groups in the cellulose are more active with the heat, which causes them to reunite with the hydroxy and hydro groups. After preheating, we dried and applied more pressure to the Ulva pertusa Kjellman, which took about 80 min to reach 4 MPa; the algae finally had a continuous compression in the highest press. This compression took about 100 min total. In the end, we dried the bio-board until the applicable moisture content about 7% [13]. With the above method, we made three kinds of bio-boards; each board was cut into six test pieces for the rupture stress experiment and one test piece for the shrinkage experiment.

2.2 The Zostera Marina Bio-board

The flowcharts of the process for producing bio-boards of *Zostera Marina* are shown in Fig. 2. First, the dried Zostera was put in water for over 24 hours for restoration. Then the cellulose of dried Zostera returned to the same condition as the fresh cellulose. The restored Zostera were cut to make each piece of within 2 cm. The cellulose of Zostera was refined by grinding in the electric buhrstone mill. Second, the refined Zostera and water were defibrated for 72 hours at 35℃ in a thermostat before compression molded. The stiff coarse fibers were grinded during refining, which made the macromolecule fibers into microfibers, and the defibration process made the microfibers were exposed more active hydroxy groups and laid the foundation for physical adsorption. The

treatments before compression molding are pretreatment. The compression mold is the same with the production of the Ulva bio-board.

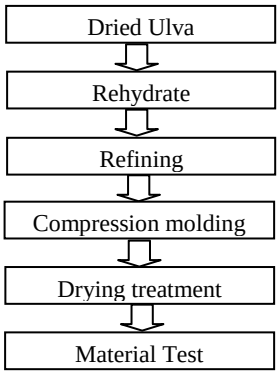

Fig. 1 Flowchart of the process for producing Ulva board

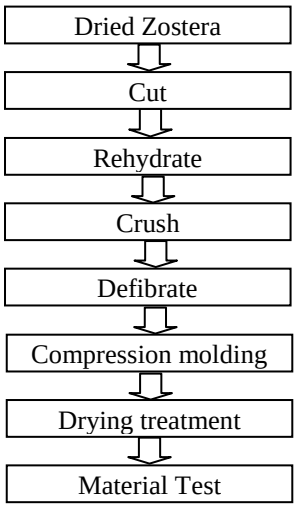

Fig. 2 Flowchart of the process for producing Zostera board

The mold is filled with Zostera Marina and a hot presser is used for compression. While preheating the mold and the material, pressure is gradually applied; when 0.2 MPa of pressure has been applied for 10 min, the preheating is done. During the hot compression, another connection opportunity is obtained since the moist Zostera are primarily dehydrated. The dehydrated process of Zostera material is faster than Ulva. After the preheating process we dried and pressure to the Zostera. It is only need 2 stages that Zostera was dehydrated, and only took about 20 min. The dehydration of Zostera is faster than Ulva. Finally, it was keep 15 min in the highest press. This compression took about 45 min total. With the above method, we made three kinds of Zostera bio-boards; each board was cut into six test pieces for the rupture stress experiment and one test piece for the shrinkage experiment.

2.3 Experimental Conditions

In order to make high strength bio-boards, in this study, the pressure of a hot presser at 4 MPa and 5 MPa; the drying temperature at 90℃ and 100℃; the materials are Ulva pertusa Kjellman and Zostera Marina. We made six kinds of bio-boards. Table 1 shows the experimental conditions for the bio-boards.

Table 1 Test condition for producing the bio-boards

Material	Defibrate	Pressure (MPa)	Temperature (℃)	Board No.
Ulva	Done not	4	90	A
		4	100	B
		5	100	C
Zostera	Done	4	90	D
		4	100	E
		5	100	F

（a）Board B

（b）Board E

Fig. 3 The photo of bio-boards B and E

2.4 Strength Test

To investigate the mechanical properties of bio-boards, six test pieces were cut from each bio-board for tensile testing. The test pieces were made according to the Japanese Industrial Standards (JIS) [14]. The strength standard of the bio-boards is in reference to the wood and plastic, the measured rupture stress and the elastic modulus [17]. The rupture stress is a specific limiting value for the tensile stress when the pieces are being pulled. The destruction stress is measured from the tensile load in the tensile test and is given by Eq. (1):

$$\sigma = \frac{P}{A} \tag{1}$$

where, σ is normal stress; P is the tensile load and A is the cross sectional area.

3. Results and Discussion

In this study six kinds of bio-boards were produced in different experimental condition. Photo 1 shows the bio-boards B and E. From the photo1, the board B produced by Ulva has a smooth and gleaming surface. It is the same with other boards which made from Ulva. However, the surface of the board E produced by Zostera is rough and there are many flinders of material which has not been crushed adequately.

3.1 Results of the Tensile Test

Fig. 4 shown two tensile stress-strain curves that were measured for the six test pieces from board B and E, which made of Ulva pertusa Kjellman and Zostera Marina materials for examples. The other results of the same materials were consistent with these results. In all of the tests pieces, the stress at the initiation of nonlinear behavior increased with increasing strain. The tensile stress also increased with increasing strain rate until the fracture stress decreased suddenly to zero. The maximum stress of the test pieces at rupture is the rupture stress. Each test piece has a slightly different slope and different rupture stress. This is because those are biomass materials and the distribution of the cellulose is irregular in a bio-board, which leads to an uneven strength. When we use bio-board as a material, it is very important that the stress generated by external force is less than the material stress allowed.

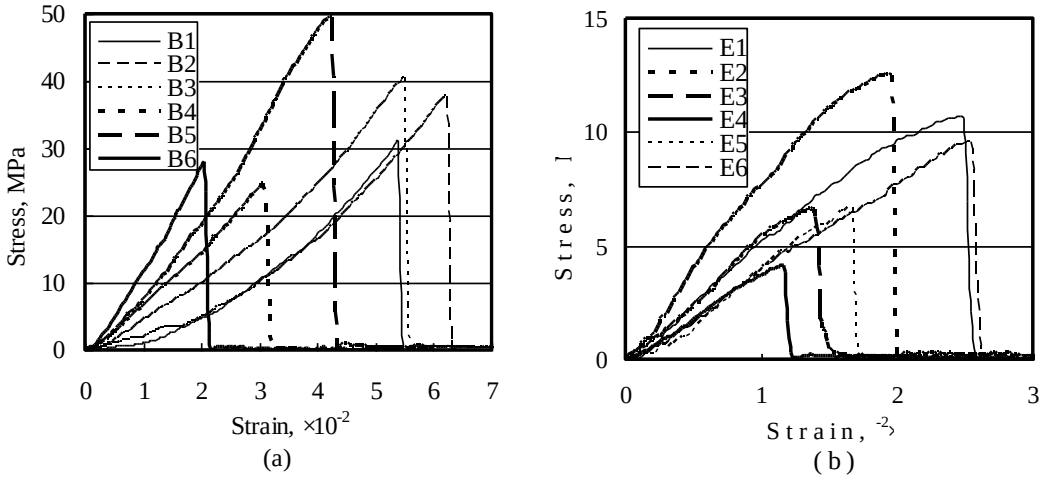

Fig. 4 The tensile stress-strain curve from board B and E

3.2 Rupture Stress

The results of the rupture stress for all of the Ulva bio-boards pieces are shown in Fig. 5, and the Zostera bio-boards pieces are shown in figure 5. It can be seen that the test pieces from the same board have a different value of rupture stress; the value of board A is 23.02 MPa-33.46 MPa, B is 24.79Mpa-49.55MPa, C is 15.56MP -26.44MPa. The value of board D is 3.77 MPa-6.62MPa, E is 4.12 Mpa-12.58MPa and F is between 3.74MPa and 5.05 MPa. Since the biomass material board is made of natural cellulose, the cellulose direction is non-homogeneous. Therefore, the intensity in one board is different from another place in the same board, which is different with metal materials. Additionally, density of bio-board influences the intensity of bio-board, but it is very difficult to specify the effect of the density on intensity of bio-board. Because the re-connect condition and distribution of fiber cellulose are very important factors which effect on the intensity of bio-board. The above results show that bio-boards could be produced under all of experimental conditions.

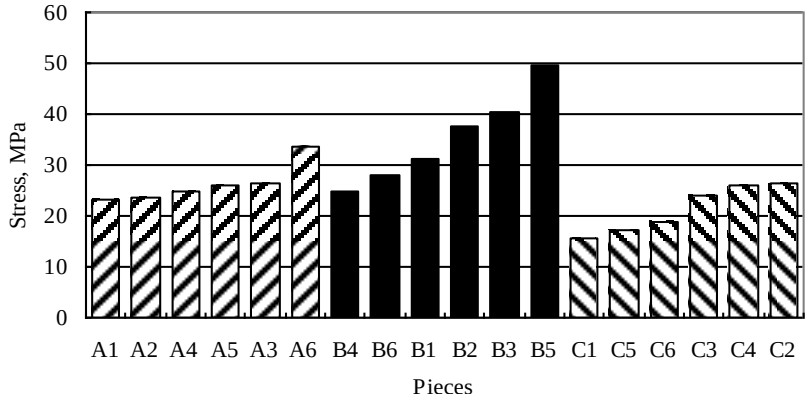

Fig. 5 The Stress of Ulva bio-boards

3.3 The effect of Processing Condition upon Strength

The average rupture stress of Ulva boards is 27.64 MPa, the average rupture stress of Zostera boards is 6.03 MPa. Therefore, the Ulva bio-boards have the higher rupture stress than Zostera bio-boards. It can be applied for the high strength material. The Ulva boards have the high strength, but the process time of Ulva is longer than Zostera. Therefore, composite board using the materials of Ulva and Zostera is necessary for producing the high strength and low cost board.

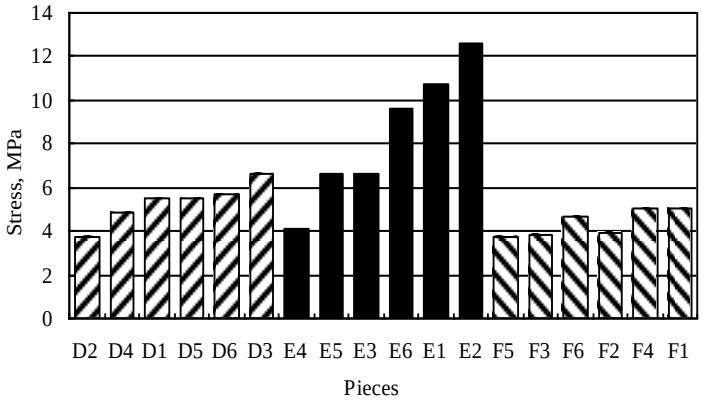

Fig. 6 The Stress of Zostera bio-boards

As shown in table 1, the bio-board A and bio-board B have produced in the same compression pressure of 4MPa, the value of board A is lower than board B in Fig. 6. The bio-board B and bio-board C have produced in the same temperature of 100℃, that the value of board C is lower than board B. Thus, the production of a dry temperature at 100℃ and compression pressure at 4MPa is applicable in Ulva bio-board. In Fig 5, that is the same with Ulva board, that board E has the higher strength than board D and board F. Thus, the production of a dry temperature at 100℃ and compression pressure at 4MPa is applicable too. Therefore, the production of a dry temperature at 100℃ and compression pressure at 4MPa is applicable in algae bio-board.

Since the biomass material board is made of natural cellulose, the cellulose direction is non-homogeneous. Therefore, the intensity in one board is different from another place in the same board, which is different with metal materials. Additionally, density of bio-board influences the intensity of bio-board, but it is very difficult to specify the effect of the density on intensity of bio-board. Because the re-connect condition and distribution of fiber cellulose are very important factors which effect on the intensity of bio-board. The above results show that bio-boards could be produced under all of experimental conditions, the producing process of bio-board is an appropriate technique.

4. Conclusions

In the present study, by using Ulva pertusa Kjellman and Zostera marina as a raw material, we processed Ulva pertusa Kjellman bio-board by refining, compression molding and drying treatment and processed Zostera marina bio-board by refining, defibrating, compression molding and drying treatment. The results are as follows:

1) Using Ulva pertusa Kjellman and Zostera as a raw material, we successfully processed the bio-board. The pressure was 4 MPa and 5 MPa; the drying temperature was 90℃ and 100℃; and non-defibrating or defibrateing

production pretreatments were used to produce high density bio-board material. To produce high strength bio-board with Ulva and Zostera, the experimental conditions are as follows: Pressure: 4 MPa; Drying temperature: 100℃.

2) The bio-board produced with Ulva has high strength and smooth surface, and it is about 3 times stronger than polystyrene plastic material. Because Zostera contain little hemicellulose, in the compression process water can be quickly disengage from Zostera, and the producing time is shortened. Thus, it is necessary to add Zostera in Ulva board in actual production, so processing cost can be effectively reduced and the production efficiency can be improved.

3) This study showed that biomass material has many potential applications in packaging material. The biomass materials is biodegradable materials, has green environmental-protective quality for substitute the food and medical packaging, transportation packaging, etc. From now on the biomass material will propel the packaging material forward.

Acknowledgment

This work was supported by the Self-determined Research Program of Jiangnan University, the Supported No. is JUSRP11209.

References

[1] S. Nabata. *Utilization and classification of seaweed*, Hokusuishi Dayori, No. 69 , pp. 1-6, 2005.

[2] M. Uchimura, G. Yoshida, M. Hiraoka, T. Komatsu, S. Arai and T. Terawaki. Ecological studies of green tide, Ulva spp. (Chlorophyta) in Hiroshima Bay, the Seto Inland Sea, *The Japanese Journal of Phycology*, Vol. 52, pp. 17-22, 2004.

[3] T. Nakanishi, Y. Shibata and A. Yoshino. Wise Use of Ulva to establish the Recycle-Based Society in GAMAGORI, *The Japan society of naval architects and ocean engineers*, No. 2K, pp. 119-122, 2006.

[4] K. Otsuka. State of the Green Tide and Its Countermeasure, *The Japan society of naval architects and ocean engineers*, No. 2K, pp. 95-98, 2006.

[5] Abe M., et al.. Estimation of production in Zostera marina Population by Biomass Method, *Aquaculture Sci.*, Vol. 56, No. 4, pp. 567-572, 2008.

[6] C. J. Hillson. *Seaweeds*, Keystone Books, 1977.

[7] T. Yoshimura, K. Shimuta, et al. Attempted Preparation and Characterization of Superabsorbent Hydrogels from Extracts of Sea lettuce, *Bulletin of Faculty of Human Environmental Science*, Vol. 38, pp. 19-23, 2007.

[8] M. Notoya., *Restoration of environment and utilization of seaweed*, Seizando-Shoten Publishing Co., Ltd., 2001.

[9] Report of investigation on utilization of sea lettuce, *MIKAWAWAN environmental challenge executive committee*, Vol. 3, pp. 37-39, 2005.

[10] Wikipedia. Zostera marina.

[11] T. Fujiwara and O. Kurita. Utilization of the Unused Seaweed to Food (Part 1), *Research Paper of Mie Prefecture Industrial Research Institute*, Vol. 31, pp. 90-93, 2007.

[12] Isogai A. *Material Science of Cellulose*, University of Tokyo Press, 2001.

[13] H. Sun, X. L. Wang, K. Kito, et al.. Development of Biomass Materials Using Algae, *Journal of Information*, Vol.10, No. 4, pp. 481-490, 2010.

[14] Japanese Industrial Standard Committee. *Testing method for tensile Properties of Glass Fiber Reinforced Plastics*, 1987.

International Journal of Comprehensive Engineering
Part C, 2(4), 326-331, 2013
Doi: 10.14270/IJCE2013.2.4.c326
Regular paper

ISSN 2186-2680
e-ISSN 2186-2656
www.iace-journal.org

Design and Fault Diagnosis Symptom Parameters on Gears

Hongwu Chen [1, #], Can Wang [1] and Feng Wang [1]

[1] Engineering College, Shanghai Ocean University, Shanghai, 201306, China

[#] Corresponding author: hwchen@shou.edu.cn; Tel.:+86-21-61900817; Fax: +86-21-61900805

Abstract: The form of gear failure and other commonly used diagnostic methods and gear fault diagnosis based on the vibration mechanism of research is given a number of gear fault diagnosis of the characteristics of commonly used parameters. Vibration through the gear mechanism of failure can help us understand the nature of gear failure and features. In this paper, the symptom parameters are defined definitely and extracted through an example experiment. Moreover the experimental process is described in detail. The method proposed in this article does not apply only to gear fault diagnosis, but also to promote the application of other rotating machinery fault diagnosis.

Keywords: Gears, Fault Diagnosis, Symptom Parameters.

Received: May 25,2012 / Accepted: Aug. 12,2013 / Published: Nov. 15,2013

1. Introduction

Condition monitoring of rotating machinery is important in terms of system maintenance and process automation at ocean engineering and ship equipments. One of the most common failures in rotating machines is the gear failure. In industrial applications, gears are considered as critical mechanical components and a defect in such a gear would cause malfunction and may even lead to catastrophic failure of the machinery. Gears are the heart of almost every rotating machine. Gears failures are one of the foremost causes of failures in rotating machinery. Gear failures can sometimes cause both personal damage and economic loss, if the incipient fault symptoms cannot be detected and diagnosed well in advance. Therefore they have received much attention in the field of vibration analysis as they represent an area where much can be gained from the early detection of faults.

Different methods have been studied in the last two decades, such as vibration measurements, acoustic measurements, and temperature measurements, among these methods, vibration measurements and analysis are widely applied. Consequently, a lot of work has been done on vibration analysis of gears. In most gear fault diagnosis and prognosis systems, vibration signals are acquired from accelerometers mounted on the outer surface of gear housing. The signals consist of vibrations from shafts, gears, hell, and other neighboring components. The useful information is corrupted and it is difficult to diagnose the fault from such vibration signals. Some techniques use the stator currents of the electrical motor as the input signals for fault detection [1]. Fault signal detection and recognition are often accomplished by pattern recognition using a neural network [2, 3], RBF network [4], Gaussian mixture model network [5, 6], fuzzy logic network [5], Bayesian classifier [7], vector correlation or vector distance measure [8]. Commonly used feature generation methods include the short-time Fourier transform (STFT) [2], wavelet time-scale decomposition [2, 9, 10], cumulant spectrum [8], etc.

In this paper, the symptom parameters are defined definitely and extracted through an example experiment. Moreover the experimental process is described in detail.

2. Symptom Parameter for Condition Diagnosis

For automatic diagnosis, symptom parameters are needed that can sensitively distinguish the fault types. A large set of symptom parameters has been defined in the pattern recognition field. Here, many kinds of symptom parameters in the amplitude domain, commonly used for the fault diagnosis of plant machinery, are considered [11].

$$p_1 = \frac{\sigma}{\overline{X}} \quad ; \quad \text{Here,} \quad \overline{X} = \frac{\sum_{i=1}^{N} |x_i|}{N} \tag{1}$$

$$p_2 = \frac{\sum_{i=1}^{N} (|x_i| - \overline{X})^3}{\sigma^3} \quad ; \quad \text{Here,} \quad \sigma = \sqrt{\frac{\sum_{i=1}^{N} (|x_i| - \overline{X})^2}{N-1}} \tag{2}$$

$$p_3 = \frac{\sum_{i=1}^{N} (|x_i| - \overline{X})^4}{\sigma^4} \tag{3}$$

$$p_4 = \frac{\overline{X}_p}{\overline{X}} \tag{4}$$

Here, $\overline{X}_p$ is the mean value of peak values of $|x_i|$ (i=1 to N).

$$p_5 = \frac{|\overline{X}_{\max}|}{\overline{X}_p} \tag{5}$$

Here, $|\overline{X}_{\max}|$ is the mean value of 10 peak values (from maximum peak value to tenth value).

$$p_6 = \frac{\overline{X}_p}{\sigma_p} \tag{6}$$

Here, σ_p is the standard deviation of peak values of $|x_i|$ (i=1 to N).

$$p_7 = \frac{\overline{X}_L}{\sigma_L} \tag{7}$$

Here, X_L and σ_L are the mean value and the standard deviation of valley values of x_i respectively.

$$p_8 = \frac{\sum_{i=1}^{N} \sqrt{|X_i|}}{\sqrt{\sigma}} \tag{8}$$

$$p_9 = \frac{\sum_{i=1}^{N} X_i^{\,2}}{\sigma^2} \tag{9}$$

$$p_{10} = \frac{\sum_{i=1}^{N} \log(|x_i| + 1)}{\log(\sigma)} \quad ; \quad x_i \neq 0 \tag{10}$$

Here, DI (Distinction Index) is calculated by

$$DI = \frac{|\mu_{2-}\mu_1|}{\sqrt{\sigma_1^{\ 2} + \sigma_2^{\ 2}}} \quad \text{or} \quad = \frac{|\overline{X}_2 - \overline{X}_1|}{\sqrt{\sigma_1^{\ 2} + \sigma_2^{\ 2}}} \tag{11}$$

The DR is defined as $DR = 1 - P_0$, here $P_0 = \frac{1}{\sqrt{2\pi}} \int_{\infty}^{DI} \exp\left(-\frac{\mu^2}{2}\right) d\mu$

It is obvious that the larger the value of DI, the larger the value of DR, and therefore the better the symptom parameter. Therefore, DI can be used to evaluate the distinguishing sensitivity of symptom parameter

3. Experimental System

The vibration-based diagnosis has become the well-accepted detection technique because of ease of measurement. When gear fault occurs, the vibration signals always display non-stationary behavior. In fact, the vibration of normal gears is usually complex and nonlinear due to the compliance vibration and the effect of lubrication, which mainly come from the varying compliance of the structure, internal excitations and external disturbance. The former two vibrations are intrinsic to gears while the latter vibration is noise and could be removed. Therefore how to extract the fault characteristic information from the non-stationary vibration signals is the crux of the gear fault diagnosis.

So a gear fault diagnosis experiment system is given as fig.1.

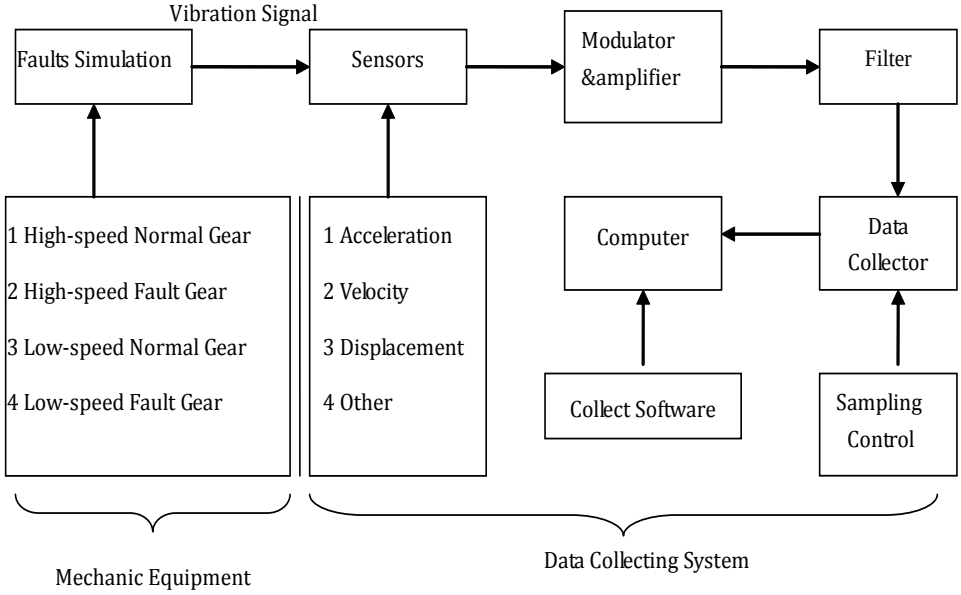

Fig.1 Gear Fault Diagnosis Experiment System

Fig. 2 The gears for tests

Fig.2 shows a normal gear, and a fault gear with broken tooth for the tests. Vibration signals were measured suing the acceleration sensor fixed the gears house. The inertia moment of the load is 0.04 kgm2. Here we consider two gears condition that are gear with normal, gear with broken tooth, in which the crack fault is introduced by cutting slot with laser in the root of tooth. The KD1001L accelerometer sensor is mounted on the gears house to capture the gear vibration data. The location of the sensor data acquisition is shown in Fig.3.

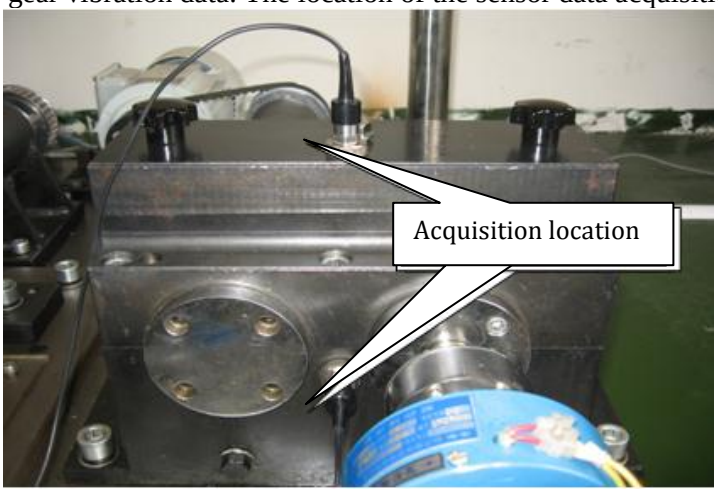

Fig.3 The location of the sensor data acquisition

4. Case Study

A gears fault experimental platform is given as Fig.4. The experimental program follows as Fig.5.

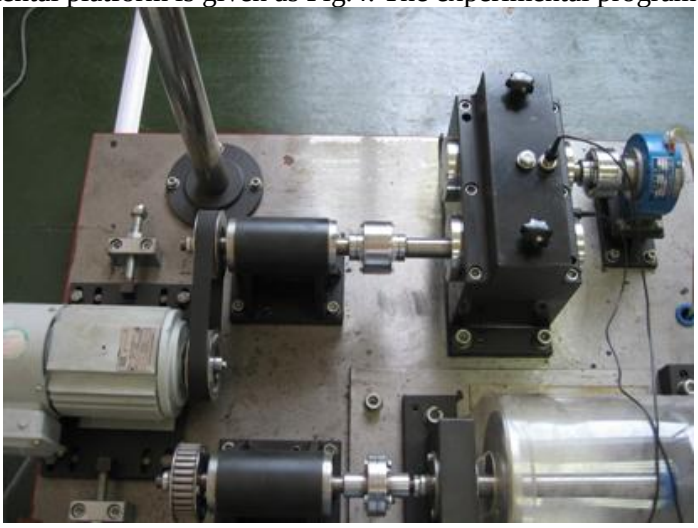

Fig.4 A gears fault experimental platform

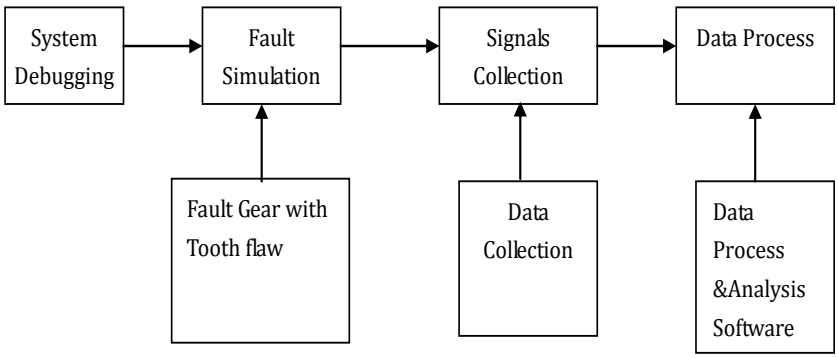

Fig. 5 Experimental program chart

After a series of experiment and computation according to symptom parameters formula, we can get the result as Table 1. Here H stands for high-speed fualt gear and L for low-speed fault gear.

Table 1 Characteristic parameters of DI, DR value table

	H		L	
	DI	DR	DI	DR
P1	0	0.5	0.7385	0.7699
P2	0	0.5	0.2062	0.5817
P3	0.1794	0.5712	0.6408	0.7392
P4	0.1748	0.5694	0.1694	0.5673
P5	0.1688	0.567	1.4843	0.9311
P6	0.31	0.6217	1.7328	0.9584
P7	0.1599	0.5935	1.4086	0.9205
P8	0.3814	0.6485	1.0855	0.8611
P9	0.1596	0.5634	0.5491	0.7085
P10	0.1675	0.5665	1.6622	0.9518

So we can choose the larger value of symptom parameters to diagnose gear failure and features. As for high-speed fualt gear, the symptom parameter P8's DI is 0.3814; and P8's DR is 0.6485. As to low-speed fault gear, the symptom parameter P6's DI is 1.7328; and P6's DR is 0.9583. So the data and corresponding parameters are selected in the Table 2.

Table 2 The characteristic parameters of the largest of DI and DR

Condition	DI	DR	Symptom parameter
H	0.3814	0.6485	P8
L	1.7328	0.9583	P6

5. Conclusion

Machinery diagnosis depends largely on the feature extraction of machinery signals, so it is important that the extracted features should be both sensitive to fault occurrence and reliable against disturbances. In order to effectively diagnose faults, this paper proposes a diagnosis method with the symptom parameters. The experiment result shows these symptom parameters can reflect the characteristics of the signal measured of the condition diagnosis of gears. The method proposed in this article does not apply only to gears fault diagnosis, but also to promote the application of other rotating machinery fault diagnosis.

Acknowledgement

This work was supported by National Natural Science Foundation of China (No. 51075258, No. 51005145), Shanghai Natural Science Foundation (No. 09ZR1421800, No. 09ZR1421600). Their support is gratefully acknowledged.

References

[1] Y. Yang, Y. G He, J. S Cheng and D. J Yu. A Gear Fault Diagnosis Using Hilbert Spectrum Based on MODWPT and a Comparison with EMD Approach, *Measurement*, Vol. 42, pp. 542-551, 2009

[2] T.B. Brotherton and T. Pollard. Applications of Time-Frequency and Time-Scale Representations to Fault Detection and Classification, *Proceedings of the IEEE Signal Processing International Symposium on Time-Frequency and Time-Scale Analysis*, Vol. 2242, pp. 95-98, 1992.

[3] D. M. Yang, A. F. Stronach and P. MacConnel. Third-Order Spectral Techniques For The Diagnosis Of Motor Bearing Condition Using Artificial Neural Network, *Mechanical Systems and Signal Processing*, Vol. 16, pp. 391-411, 2002.

[4] J. A. Leonard and M.A. Kramer. Radial Basis Function Networks for Classifying Process Faults, *IEEE Control Systems magazine*, pp. 31-38, 1991.

[5] M. Chow, R. N. Sharpe and J. Hung. On the Application and Design of Artificial Neural Network for Motor Fault Detection, *IEEE Transactions on Industrial Electronics*, Vol. 40, No. 2, pp. 189-196, 1993.

[6] L. P. Heck and K. C. Chou. Gaussian Mixture Model Classifier for Machine Monitoring, Proceedings of the *IEEE world Congress on Computational Neural Network and International Conference on Intelligence*, Vol. 7, pp. 4493-4496, 1994.

[7] E. Meyer and T. Tuthill. Bayesian Classification of Ultrasound Signals Using Wavelet Coefficients, *Proceedings of the IEEE National Aerospace and Electronics Conference*, Vol. 1, pp. 240-243, 1995.

[8] K. W. Baugh. On Parametrically Phase-Coupled Random Harmonic Processes, *Proceedings of the IEEE Signal Processing Workshop on Higher-Order Statics*, pp. 346-350, 1993.

[9] H. C. Choe, C. E. Poole, A. M. Yu and H. H. Szu. Novel Identification of Intercepted Signals from Unknown Radio Transmitters, *Proceedings of the SPIE Wavelet Applications*, pp. 504-517, 1995.

[10] T. Pend, W. Gui, M. Wu and Y. Xie. A Fusion Diagnosis Approach to Bearing Faults, *Proceedings of the International Conference on Modeling and simulation in Distributed Applications*, pp. 759-766, 2001.

[11] P. Chen, M. Taniguchi, T. Toyota and Z. He. Fault Diagnosis Method for Machinery in Unsteady Operating Condition by Instantaneous Power Spectrum and Genetic Programming, *Mechanical systems and signal processing*, Vol. 19, pp. 175-194, 2005.

International Journal of Comprehensive Engineering
Part C, 2(4), 332-340, 2013
Doi: 10.14270/IJCE2013.2.4.c332
Regular paper

ISSN 2186-2680
e-ISSN 2186-2656
www.iace-journal.org

A New Model for the Indentation Depth of a Particle into the Wafer Surface in Chemical Mechanical Polishing Process

Jianzhong Jiang [1, #], Yongwu Zhao [2]

[1] Food Engineering & Machinery Group, School of Mechanical Engineering, Jiangnan University, Wuxi, Jiangsu, 214122, China
[2] Mechanical Engineering & Machinery Group, School of Mechanical Engineering, Jiangnan University, Wuxi, Jiangsu, 214122, P. R. China

[#] Corresponding author: jjzwxjn @163.com; Tel.: +86-510-85912082; Fax: +86-510-85912082

Abstract: In accordance with the hypothesis of the equivalent beam bending for a three-body contact among pad/wafer/particles, a more precise and reasonable mathematical model for the indentation depth of a particle into wafer surface in chemical mechanical polishing process is developed. The model comprehensively considers the influence of most valuables in chemical mechanical polishing process including pad elastic modulus, wafer surface hardness, particle diameter, poisson' s ratio of pad material, standard deviation of the pad asperity height distribution σ, average radius of curvature of the tip of the pad asperities β, pad surface topology feature constant C, particle density ,particle concentration. Among these valuables, particle diameter, particle density and pad surface topology feature parameters C, σ, β are often omitted in former models, which will lead to theoretical deviation. Finally, by means of numerical calculation, it is found that the new model is more reliable and correct than the models of Luo, Qin and L. Chang.

Keywords: Chemical Mechanical Polishing, Abrasive, Particle, Modeling, Wafer.

Received: May 25,2012 / Accepted: Aug. 12,2013 / Published: Nov. 15,2013

1. Introduction

Chemical mechanical polishing(CMP) as a compound ultra-precision polishing technology based on the synergy of chemical and mechanical action, is widely used in integrated circuit (IC) manufacturing process at all stages of silicon wafer planarization. It is the most effective and practical technology to realize nano-scale ultra-smooth surface processing without damage and the only way to achieve global planarization. The precise control of the CMP process depends on understanding its mechanism of material removal. Modeling for the indentation depth of a particle into wafer surface is an important part of modeling for the material removal rate of CMP. It is directly related to the success or failure of material removal model of CMP.

In chemical mechanical polishing process, the abrasive particle is pressed into the contact area of pad /wafer under the external force, which forms a three-body contact. Pad is so soft that after wafer is pressed to contact pad asperities, pad asperities will wrap abrasive particles. In this case, the work pressure p is sustained by the pad asperities and the abrasive particle together [1]. The schematic diagram of a three-body contact of pad /wafer/particle is shown in Fig. 1.

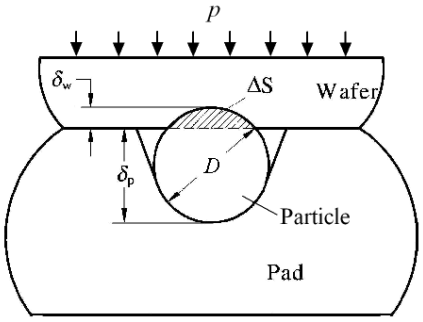

Fig. 1 Schematic of pad/wafer/particle three-body contact.

In Fig.1 the applied forces exerted on abrasive particle include the external force F_Z conveyed by pad asperities, anti-force F_a by wafer surface, abrasive particle gravity. As the abrasive particle diameter is in nanometer scale, taking Al_2O_3 abrasive whose density is larger in CMP as an example to calculate its gravity gives 1.88×10^{-9} nN, while the scale of the external force acting on abrasive particle generally can reach tens to hundreds of nN [2], the abrasive gravity can be ignored. When a particle is in equilibrium state, the force balance equation is shown as follows:

$$F_a = F_Z \tag{1}$$

The contact between wafer and particle is small deformation, as its indentation depth into wafer δ_W is far less the particle diameter D， The whole process is considered as an completely plastic deformation [1], and the total plastic contact stress between wafer/ particle F_a is given as

$$F_a = H_W \pi D \delta_W \tag{2}$$

here H_W is the wafer surface hardness.

Influence factors of the external force conveyed by pad asperities to a single abrasive F_Z are very complicated, if the specific analytical formula of F_Z can be got, combined with the particle force balance equation shown as Eq.(1) , Eq. (2) and the geometric relationship equation in Fig. 1 given as

$$\delta_P + \delta_W = D \tag{3}$$

The indentation depth of particle into wafer δ_W and indentation depth of particle into pad δ_p can be obtained by numerical methods.

Luo [3] and Qin [4] calculated F_Z as

$$F_z = \frac{1}{4}\pi D^2 p_r \tag{4}$$

where p_r is the average stress of the actual contact area between pad/wafer.

Jongwon Seok [5] amended Eq.(4) and introduced a stress concentration factor k in it, then got the following equation:

$$F_z = \frac{1}{4}\pi D^2 k p_r \tag{5}$$

In fact, Luo and Jongwon's equations which did not consider enough influence factors are too simplistic.

YongsongXie [6] assumed that it both occurred to be the plastic deformation when particle contacted with pad and wafer. Hence, the external force applied on a single particle is given as

$$F_z = \pi D \delta_W H_W = \pi D \delta_P H_P \tag{6}$$

Here H_P is pad surface hardness.

Zhao [1] thought that it occurs to be the plastic deformation between wafer/particle contact surface , the elastic deformation between pad/particle contact surface. And then F_Z is shown as

$$F_z = \pi D \delta_W H_W = \frac{4}{3} E_{PS} \delta_P^{\frac{3}{2}} \left(\frac{D}{2} \right)^{\frac{1}{2}} \tag{7}$$

Here E_{PS} is the equivalent elasticity modulus of pad and particle.

On the basis of Zhao's Eq.(7), L. Chang [7] derived the equation of the indentation depth of particle into wafer δ_W as below

$$\delta_W \approx 0.25 \frac{E_P}{H_W} D \tag{8}$$

Cook [8] and Brown [9] suggested that it should adopt the following Eq.(9) to calculate F_Z

$$F_z = \frac{2\sqrt{3} p D^2}{4 k_3} \tag{9}$$

where k_3 is a factor which describes the ability of particles to fill wafer surface. In a typical CMP，k_3<<1[2].

From the above analysis, these above researchers have ignored the fact that the indentation depth of particle into pad δ_p is nearly close to particle diameter owing to such soft material property of polyurethane pad[1]. Besides, it is large deformation of hyper-elastic contact during the whole indentation progress, so the classic Hertz contact theory and plastic contact theory are not applicable in CMP. Aforementioned models are not comprehensive and consider too less influence factors.

2. The theoretical analysis of the new model

The former models for the indentation depth of particle into wafer δ_W are built on classic Hertz contact theory, elastic-plastic micro-contact mechanics which neglected the super-elastic and big deformation feature of the three-body contact of wafer/pad/particle in CMP. Hence, many very important factors such as particle concentration, particle density and pad surface topology feature parameters are not involved in these models, which will inevitably affect the accuracy of the subsequent CMP material removal model. In this paper, a new approach based on the hypothesis of the equivalent beam bending for a three-body contact among pad/wafer/particles is presented to model the indentation depth of particle into wafer δ_W.

2.1 The hypothesis of the equivalent beam bending

Shown in Fig. 2, Guang-hui Fu [10] used a creative equivalent beam bending model to calculate the external force F_Z on a particle during CMP.

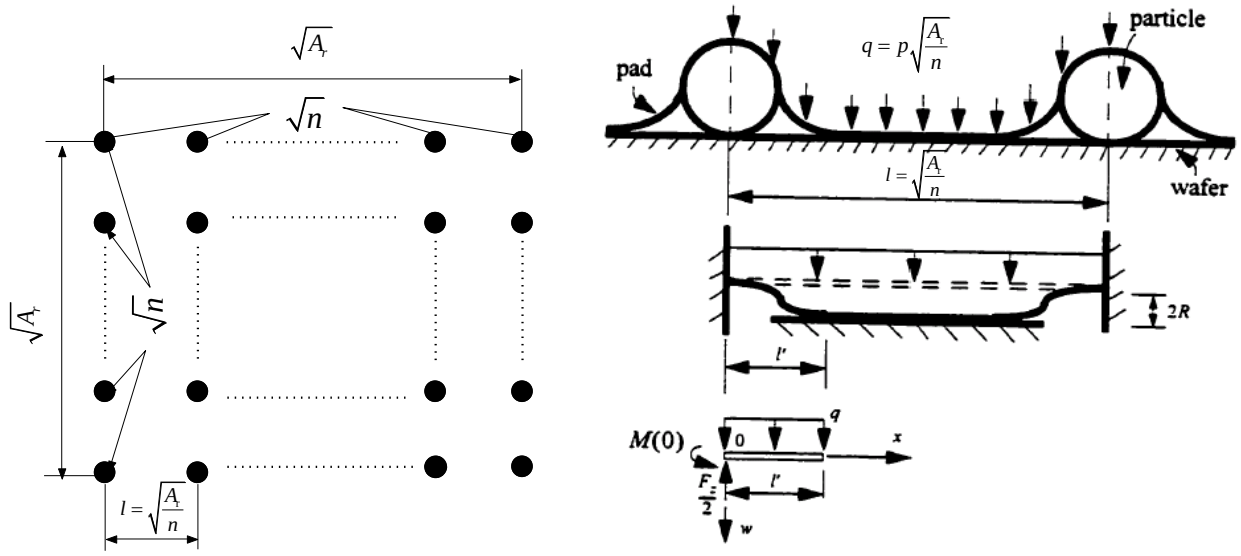

Fig. 2 The equivalent beam bending model of CMP.

In his model, the particles are assumed to be distributed uniformly in the contact area between pad and wafer. The distance l between two neighboring particles can be written as

$$l = \sqrt{\frac{A_r}{n}} \tag{10}$$

Where A_r is the effect contact areas between pad/wafer, n is the number of effective particles embedded into the contact areas between pad/ wafer.

The part of the pad between two particles is reduced to a fixed-fixed bending beam with a distributed load q shown as [10]

$$q = p\sqrt{\frac{A_r}{n}} \tag{11}$$

Using beam theory of mechanics of materials, the applied force on per particle can be expressed as

$$F_Z = \frac{4}{3}ql' = \left(\frac{4^5}{3^3}\right)^{1/4}\left[E_P t_p^{\,3}\frac{D}{2}\left(\frac{A_r}{n}\right)^2 p^3\right]^{1/4} \tag{12}$$

Here l', E_P, t_P represent ,respectively, the length of free beam ,the young's modulus of pad , the equivalent beam thickness.

According to Zhao's model [1], the number of effective particles embedded into the contact areas between pad/ wafer n can be calculated by

$$n = A_r\left(\frac{6\chi}{\pi D^3}\right)^{\frac{2}{3}} = A_r\left(\frac{6C_a\rho_f}{\pi D^3\rho_s}\right)^{\frac{2}{3}} \tag{13}$$

In Eq.(13), χ is abrasive particle volume concentration, C_a is abrasive particle mass concentration, ρ_f is slurry density, ρ_s is abrasive particle density.

In accordance with Eq. (1) , combined with Eq. (3), Eq.(12)and Eq.(13), we have the following result

$$\delta_W = 0.664\frac{E_P^{1/4}p^{\frac{3}{4}}}{H_W}\left(\frac{6C_a\rho_f}{\pi\rho_s}\right)^{-\frac{1}{3}} D^{\frac{1}{4}}t_p^{\frac{3}{4}} \tag{14}$$

Factors affecting the thickness of equivalent beam t_P include particle diameter D, the elastic modulus of pad E_P, the working pressure p. Based on the theory of dimensionless unit analysis of the four variables, we have

$$\frac{t_p}{D} = k_2\left(\frac{E_P}{p}\right)^{k_1} \tag{15}$$

where k_2、k_1 are dimensionless constants.

Substituting Eq. (15) into Eq. (14), we obtain

$$\delta_W = 0.664k_2^{\frac{3}{4}}E_P^{\left(\frac{1}{4}+\frac{3}{4}k_1\right)}p^{\left(\frac{3}{4}-\frac{3}{4}k_1\right)}\frac{1}{H_W}D\left(\frac{6C_a\rho_f}{\pi\rho_s}\right)^{-\frac{1}{3}} \tag{16}$$

2.2 Determination of constant k_1

According to Qin's analysis [4], in the range of the working pressure p in a typical CMP , the average stress of the actual contact area between pad/wafer p_r approximately changes very slowly with the increase of the working pressure p. Thus, we can make such an assumption that with the pressing of a wafer into a polishing pad the actual average contact pressure p_r has nothing to do with the working pressure p and the increased working pressure is totally assumed by the increased abrasive particles embedded into the contact area between pad asperities and wafer ,i.e., p_r can be considered to be a constant. As a single particle is concerned, the applied force of pad on it F_z keep unchanged, so the indentation depth of the particle into the wafer δ_W is unchanged. This point view is substantiated by Zhao and L.Chang [1], Qin [11],Jeng [12]. If the working pressure p doesn't affect the indentation depth δ_W , we can obtain k_1=1 in Eq. (16). And then rearranging yields

$$\delta_W = 0.664k_2^{\frac{3}{4}}\frac{E_P}{H_W}D\left(\frac{6C_a\rho_f}{\pi\rho_s}\right)^{-\frac{1}{3}} \tag{17}$$

2.3 Determination of constant k_2

In Eq.(17) k_2 is a dimensionless constant and has no relation to variety of the pad/wafer/particle and operating parameters during the course of CMP. If k_2 is obtained in a specific formula, Eq. (17) can be applied to every case of CMP.

As visualized in Fig.(3), it is assumed that the pressure of contact between pad / wafer is p_D, and the number of the abrasive particles embedded into the contact area between pad/wafer is n . Thus, the total area of contact between abrasive particles and wafer surface A_P is shown as

$$A_P = n\pi\left(\frac{D}{2}\right)^2 = A_r\left(\frac{6\chi}{\pi D^3}\right)^{\frac{2}{3}}\pi\left(\frac{D}{2}\right)^2 \tag{18}$$

Associated with Eq.(1),(2),(13), the total applied force of all effective particles on wafer surface F_P is given as

$$F_P = nF_Z = A_r\left(\frac{6\chi}{\pi D^3}\right)^{\frac{2}{3}}H_W\pi D\delta_W \tag{19}$$

Then the force equilibrium of the wafer gives

$$F_P + \left(A_r - A_P\right)p_D = pA_0 = p_rA_r \tag{20}$$

where A_0 represents the total area of the wafer surface.

Substituting Eq.(18),(19) into Eq.(20) gives

$$\left(\frac{6\chi}{\pi D^3}\right)^{\frac{2}{3}}H_W\pi D\delta_W + \left(1-\left(\frac{6\chi}{\pi D^3}\right)^{\frac{2}{3}}\pi\left(\frac{D}{2}\right)^2\right)p_D = p_r \tag{21}$$

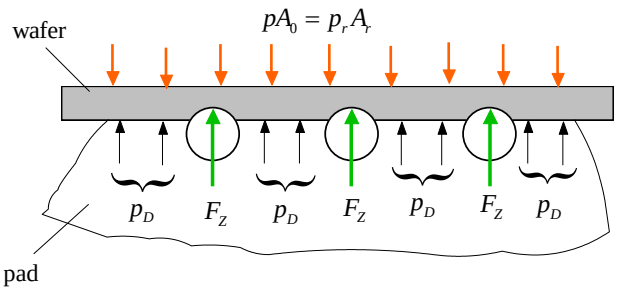

Fig. 3 Force applied on the wafer.

Shown in Fig. 4, it is an case that the effective contact area of wafer/pad is studded with abrasive particles and there is no vacant space among neighboring particles. When in such extreme case, from Eq.(21), we have

$$1=(\frac{6\chi}{\pi D^3})^{\frac{2}{3}}\pi\left(\frac{D}{2}\right)^2=(\frac{6\chi}{\pi})^{\frac{2}{3}}\pi\frac{1}{4} \tag{22}$$

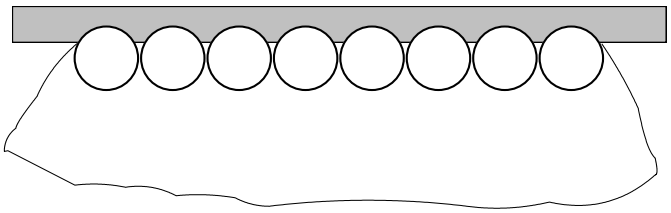

Fig. 4 Extreme list view of abrasives.

Calculating Eq.(22) gives χ=0.75 which is a extreme concentration. In the extreme case, the working pressure p is all undertaken by abrasive particles, which means

$$(\frac{6\times 0.75}{\pi D^3})^{\frac{2}{3}} H_{\mathrm{W}}\pi D\delta_{\mathrm{W}} = p_r \tag{23}$$

Qin [4] found that the average stress of the actual contact area between pad/wafer p_{r} is indicated as

$$p_r = c\left(\frac{\sigma}{\beta}\right)^{1/2}\frac{E_{\mathrm{P}}}{1-\upsilon_P{}^2} \tag{24}$$

$$c=\frac{4}{3\pi\sigma^{0.5}}\frac{\int_h^{+\infty}(z-h)^{3/2}\varphi(z)dz}{\int_h^{+\infty}(z-h)\varphi(z)dz} \tag{25}$$

here C is pad surface topology feature constant, σ is Standard deviation of the pad asperity height distribution, z is the height of an pad asperity measured from the mean of asperity heights, h is mean separation between pad and wafer based on asperity heights, $\varphi(z)$ is standard normal probability density function of asperity heights, β is average radius of curvature of the tip of the pad asperities. In Eq.(24) , by numerical calculating methods, Qin [4] found that as h/σ varies from 0.5 to 3.0, C varies from 0.3 to 0.4. In a typical CMP process , the h/σ value of the pad surface is within the range from 0.5 to 3.0 and the value of C varying from 0.3 to 0.4 hardly influences p_{r}. Thus, in order to reduce calculation, C can be taken as a constant.

In conjunction with Eq.(17), (24), substituting χ=0.75 into Eq.(23) gives

$$0.664k_2^{\frac{3}{4}}=0.28C(\frac{\sigma}{\beta})^{1/2}\frac{1}{1-\nu_P{}^2} \tag{26}$$

Substituting Eq.(26) into Eq.(17) , we have

$$\delta_{\mathrm{W}}=0.28C(\frac{\sigma}{\beta})^{1/2}\frac{1}{1-\nu_P{}^2}\frac{E_P}{H_W}D\left(\frac{6C_a\rho_f}{\pi\rho_s}\right)^{-\frac{1}{3}} \tag{27}$$

In a typical CMP，the various parameters are shown in Tab. 1. Substituting the values of parameters listed in Tab. 1 into Eq.(27) and simplifying gives

$$\delta_{\mathrm{W}} = 0.27 \frac{E_P}{H_W} D \tag{28}$$

Eq.(28) is almost the same as Eq.(8) of L. Chang [7] in the form, the calculating values from the two equations are in the same order.

3. Evalution and discussion of the model

In order to substantiate the rationality of the new model, through investigating the changing law of the pressure of contact between pad/wafer p_{D} with the increase of the volume concentration of the abrasive particles in polishing slurry χ , the new model is compared with the models of Luo [3], Qin [4] and L. Chang [7].

From Eq.(21), we obtain

$$p_{\mathrm{D}} = \frac{p_r - (\frac{6\chi}{\pi D^3})^{\frac{2}{3}} H_{\mathrm{W}} \pi D \delta_{\mathrm{W}}}{\left(1 - (\frac{6\chi}{\pi})^{\frac{2}{3}} \pi \frac{1}{4}\right)} \tag{29}$$

Substituting Eq.(27) into Eq.(29) , we have

$$p_{\mathrm{D}} = \frac{p_r - (\frac{6\chi}{\pi})^{\frac{1}{3}} \pi 0.28 C (\frac{\sigma}{\beta})^{1/2} \frac{1}{1-\nu_{\mathrm{P}}^{\ 2}} E_P}{\left(1 - (\frac{6\chi}{\pi})^{\frac{2}{3}} \pi \frac{1}{4}\right)} \tag{30}$$

Luo[3] and Qin[4] thought the external force conveyed by pad asperities to a single abrasive F_{Z} is given by

$$F_Z = H_{\mathrm{W}} \pi D \delta_{\mathrm{W}} = 0.25 \pi D^2 p_r \tag{31}$$

From Eq.(31), we have

$$\delta_{\mathrm{W}} = 0.25 D p_r / H_W \tag{32}$$

Substituting Eq.(32) into Eq.(29) gives

$$p_{\mathrm{D}} = \frac{p_r - (\frac{6\chi}{\pi})^{\frac{2}{3}} \pi 0.25 p_r}{\left(1 - (\frac{6\chi}{\pi})^{\frac{2}{3}} \pi \frac{1}{4}\right)} = p_r \tag{33}$$

Substituting Eq.(8) of L. Chang[7] into Eq.(29) gives

$$p_{\mathrm{D}} = \frac{p_r - (\frac{6\chi}{\pi})^{\frac{2}{3}} \pi 0.25 E_P}{\left(1 - (\frac{6\chi}{\pi})^{\frac{2}{3}} \pi \frac{1}{4}\right)} \tag{34}$$

According to Eq.(30),(33),(34)，the influencing curve of the volume concentration of the abrasive particles in polishing slurry χ on the pressure of contact between pad/wafer p_{D} is shown in Fig. 5. The parameters in Eq.(30),(32),(33) are from Tab. 1.

Table 1 Variables of δ_{W}

Parameter	Value	Unit	reference
standard deviation of the pad asperity	25	μm	[13]

height distribution σ			
average radius of curvature of the tip of the pad asperities β	30	μm	[13]
pad surface topology feature constant C	0.35		[4]
poisson's ratio of pad v_P	0.5		[11]
the elastic modulus of pad E_P	50	MPa	[4]
abrasive particle density ρ_s	2270	kg/m^3	[4]
slurry density ρ_f	1000	kg/m^3	[4]
mass concentration of particles C_a	0.1		[4]

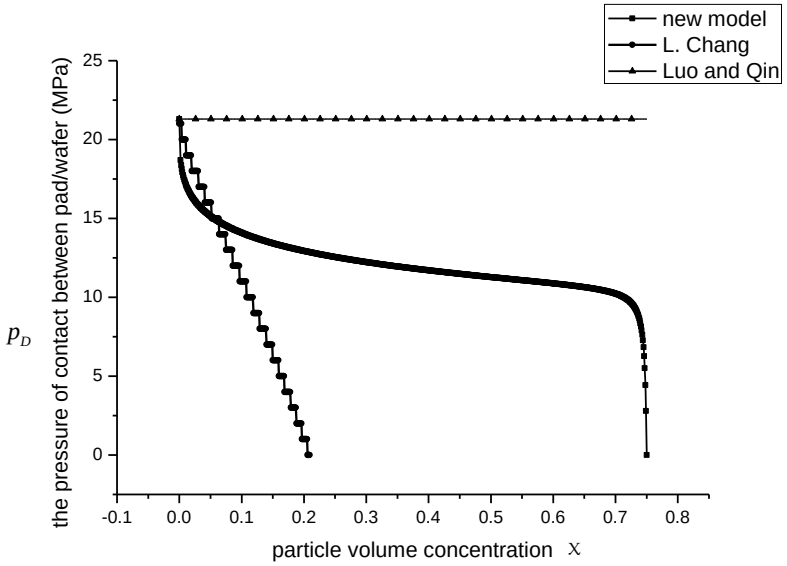

Fig. 5 Comparision of p_D.

From Fig. 5, we find in the model of Luo and Qin the pressure of contact between pad/wafer p_D is equal to the average stress of the actual contact area between pad/wafer p_r for ever and does not relate to the volume concentration of the abrasive particles χ. According to Eq.(19), it is found that only when the actual contact area between pad/wafer A_r is all covered with abrasive particles, i.e., the working force pA_0 (p_rA_r) is borne entirely by abrasive particles, the applied force exerted on every particle F_Z is given as

$$F_Z = \frac{p_r A_r}{n} = \frac{p_r A_r}{A_r / 0.25\pi D^2} = 0.25\pi D^2 p_r = H_W \pi D \delta_W \tag{35}$$

Substituting Eq.(35) into Eq.(29) can give p_D=p_r . Luo and Qin just considered the extreme case in which such extreme abrasive particles concentration is almost impossible to achieve.

In the model of L. Chang, when the abrasive particles concentration χ is 0.07，the pressure of contact between pad/wafer p_D reaches 0，which does not conform to the actual situation. In the new model, when the abrasive particles concentration χ is 0，without abrasive particles participating in polishing, the working force pA_0 is hold entirely by polishing pad, so the pressure of contact between pad/wafer p_D is p_r, with the increase of the abrasive particles concentration χ, the abrasive particles sustain part of the working force, and then the pressure of contact between pad/wafer p_D decreases, when the abrasive particles concentration χ reaches extreme value 0.75, the working force pA_0 is sustained entirely by abrasive particles, and therefore the pressure of contact between pad/wafer p_D tends to 0, which conforms to the actual situation of CMP. Hence, based on the above analysis, it is confirmed that the new model is more reliable and correct, while the abrasive particles concentration χ in the models of Luo [3],Qin [4]and L. Chang [7] is ignored, which will cause some errors.

Eq.(27) suggests that the indentation depth of particle into wafer δ_W is proportional to the particle diameter and the elastic modulus of pad, and inversely proportional to the wafer surface hardness, which is in accordance with the models of Luo [3] and Qin [4],L. Chang [7]. Under same external force, larger particle diameter causes larger indentation depth of particle into wafer. Elastic modulus can be taken as a indicator measuring the degree of elastic deformation of a material. The larger its value is, the larger the stress causing the material to elastically deform is, i.e., the larger the material rigidity is. Under same external force, with the increase of the

elastic modulus of pad, the material rigidity of pad increases and the indentation depth of particle into wafer increases correspondingly. Under same external force, with the increase of the hardness of wafer, the indentation depth of particle into wafer decreases. Furthermore, the new model indicated by Eq.(27) also suggests that the indentation depth of particle into wafer δ_W is related to particle concentration, particle density, slurry density, poisson's ratio of pad and pad surface topology property. The indentation depth of particle into wafer decreases with the increase of the particle mass concentration of the particle Ca and increases with the increase of the particle density. With the increase of the concentration of abrasive particles, the more particles per unit contact area between pad/wafer has, the less the external force exerted on per particle is, the less the indentation depth of particle into wafer is. The new model contains more parameters in which the particle concentration and particle density are the most important parameters which can not be ignored in the modeling progress. By means of computer simulation of finite elements, Yan Bo got the same conclusion [13].

4. Conclusion

On the basis of the analysis of the equivalent beam bending model for a three-body contact among pad/wafer/particles, a new approach for the indentation depth of particle into wafer surface in CMP process is put forward in this paper. Meanwhile, in accordance with this approach, a new mathematical model about the indentation depth of particle into wafer surface in CMP process is developed. The model comprehensively considers the influence of most valuables in CMP process including pad properties (modulus, poisson's ratio, asperity sizes and distribution, pad surface topology feature constant), abrasive particle characteristics (particle density, particle concentration, particle diameter), slurry density and wafer surface hardness. Especially, particle concentration, particle density and pad surface topology feature parameters C、σ、β are often omitted in the former models. The new model is more rational, scientific, more in line with the actual situation of CMP and will provide a new platform to further investigate CMP mechanism and offer a direction to control the CMP process more accurately.

Acknowledgment

The authors thank Yong-guang Wang and Guang Chen for their useful discussions. Financial support of this research work was provided in part by the Natural Science Foundation of Jiangsu Province in China (Grant No. BK2004020) and Tribology Science Foundation of the state key laboratory of Tribology in Tsinghua University in China (Grant No. SKLT04-06).

References

[1] Y. W Zhao, L. Chang. A Micro-Contact and Wear Model for Chemical–Mechanical Polishing of Silicon Wafers, *Wear,* Vol. 252, pp. 220-226, 2002.
[2] F. Zhang. Submicron *Particle Adhension and Removal in Chemical-Mechanical Polishing and Wafer Cleaning Process*, Ph.D.Thesis, Clarksom University , 2002.
[3] J. F Luo. *Integrated Modeling of Chemical Mechanical Planarization/Polishing (CMP) for Integrated Circuit Fabrication: From Particle Scale to Die and Wafer Scales*, Ph.D. Thesis, University of California, Berkeley, 2003.
[4] K. D Qin. *Multi-Scale Modeling of the Slurry Flow And the Material Removal In Chemical Mechanical Polishing*, Ph.D. Thesis, University of Florida, 2003.
[5] Jongwon Seok and Cyriaque P. Material Removal Model for Chemical-Mechanical Polishing Considering Wafer Flexibility and Edge Effects, *Wear*, Vol. 257, pp. 496-508, 2004.
[6] Y. S Xie and Bharat Bhushan. Effects of Particle Size ,Polishing Pad and Contact Pressure in Free Abrasive Polishing, *Wear*, Vol. 200, pp. 281-295, 1996.
[7] L. Chang. On the Cmp Material Removal at the Molecular Scale, *Journal of Tribology-Transactions of the ASME*, Vol. 129, pp. 436-437, 2007.
[8] L.M. Cook. Chemical Processes in Glass Polishing, *Journal of Non-Crystalline Solids*, Vol. 120, pp. 152-171, 1990.
[9] N. Brown, P. Baker and R. Parks. Polishing to Figuring Transition in Turned Optics, *Proceedings of SPIE*, Vol. 58, pp. 306-307, 1981.
[10] G. H Fu. *Modeling of chemical mechanical polishing at multiple scales*, Ph.D. Thesis, Iowa State University, Ames, 2002.
[11] Q. Kuide, M. Brij and W. P Chang. A Chemical Mechanical Polishing Model Incorporating Both the Chemical and Mechanical Effects, *Thin Solid Films*, Vol. 446, pp. 277-286, 2004.

[12] Y. R Jeng and P. Y Huang. A Material Removal Rate Model Considering Interfacial Micro-Contact Wear Behavior for Chemical Mechanical Polishing, *Journal of Tribology-Transactions of the ASME*, Vol. 127 , No. 1, pp. 190-197, 2005.
[13] Andrew Kim. A Soft Elastohydrodynamic Contact Model for Chemical Mechanical Planarization, Ph.D. Thesis, Rensselaer Polytechnic Institute ,Troy, New York, 2001.
[14] Y. Bo, X. M Zhang, X. Lu. A Model of Material Removal Rate During Chemical Mechanical Planarization of Microelectronic Materials, *Engineering Mechanics*, Vol. 21 , No. 5, pp. 126-131, 2004.

International Journal of Comprehensive Engineering
Part C, 2(4), 342-345, 2013
Doi: 10.14270/IJCE2013.2.4.c342
Regular paper

ISSN 2186-2680
e-ISSN 2186-2656
www.iace-journal.org

Design and Research for Lower Computer System of Wave Buoy Based on GPRS Communication Technology

Ziyue Wu, Jinfeng Geng, Yaoyao Huang

[1] College of Engineering Science & Technology, Shanghai Ocean University, Shanghai, 201306, China

[#] Corresponding author: zywu@shou.edu.cn

Abstract: Wave buoy has been more wildly applied in the ocean surveying field, and the bidirectional communication between the upper system and the lower system has become the focus of current researches, which transmits signal securely and effectively to upper system for reference and accurately executes commands from upper system on lower computer system,. This paper based on the GPRS wireless technology and took SCM as the core of whole system designs the lower computer system and completes the bidirectional communication. For that SCM not only sends the digital voltage data acquired and packaged after A/D conversion, but also accepts the commands from upper system to control and set the mode of current working, the bidirectional communication with wireless technology has been proposed. By system analysis on the design, this solution possesses a good feasibility, low cost, high stability and transmission efficiency, and little professional maintain.

Keywords: Wave Buoy, GPRS, Wave Direction, Wave Height.

Received: May 31,2012 / Accepted: Aug. 12,2013 / Published: Nov. 15,2013

1. Introduction

In the field of ocean engineering, wave is a most important and most complex natural phenomenon, and the size of its force and direction provides an important reference to our engineering activities. Wave buoy is an unattended measurement system, which continuously and automatically collects wave parameter data at the fixed time and location [1]. When the signal is transmitted, taking the size of data and the pattern of transmission into account, there are two key problems: one that the data must be transmitted timely and securely to data center, and the other that all setting commands can be carried to respond positively on the lower computer system. There are several traditional methods for data transmission, such as radio transmission, telephone dial, satellite communications, but these methods provide some problems, such as poor real-time and reliability, high investment and operation costs and limited range of transmission. Currently the GPRS (General Packet Radio Service) communication as a bidirectional wireless communication technology can overcome shortcomings and be regarded as a professional data transmission in some aspects compared with traditional modes. Combined with the development trends of wave buoy technology, this paper does research into the design of the lower computer system based on the GPRS wireless communication technology for driving the blossom of ocean engineering.

2. The Features and Functions of Lower Computer System

The hardware for designing lower computer system includes sensors, A/D (Analog-To-Digital) converter, SCM (Single Chip Microcomputer), SIM300 chip and so on. This solution mainly relies on SCM to put the bidirectional communication into practice, which has a simple structure, high reliability, low cost, fast processing speed. The lower computer system has the following functions: 1) the lower computer system carried the function of bidirectional communication with upper system not only can convey digital signal collected to upper system, but also accept and deal with the commands from upper system.2) The lower computer system

can display the IP address, port number, working condition, operation mode, sampling time, physical parameters, data sent and the commands from upper system, which achieves the visualization of lower computer system.

In order to adapt to current working specialties of wave buoy, the design for the lower computer system has the following features:

1) Good feasibility: As a very mature technology, the hardware to detect signal is wave height tilt sensor and direction senor. It has the following advantages: simple structure, convenient installation, high accuracy, coincidence with wave measurement principle. To get high reliability for the system, the other hardware is also selected chiefly according to the principle of high stability.

2) Good visualization: The system can timely show currently working condition including the physical parameters measured, sampling time of the system and so on, which can help staff to see the condition of operation of the system and carry a high visualization.

3. Design of Lower Computer System

3.1 Design Theory

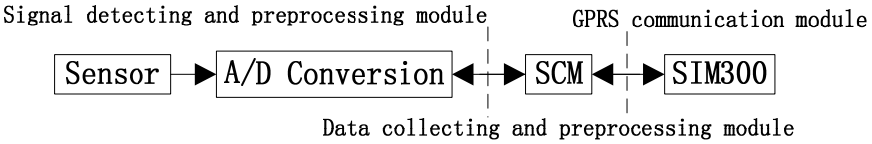

Fig. 1 Block diagram of lower computer system

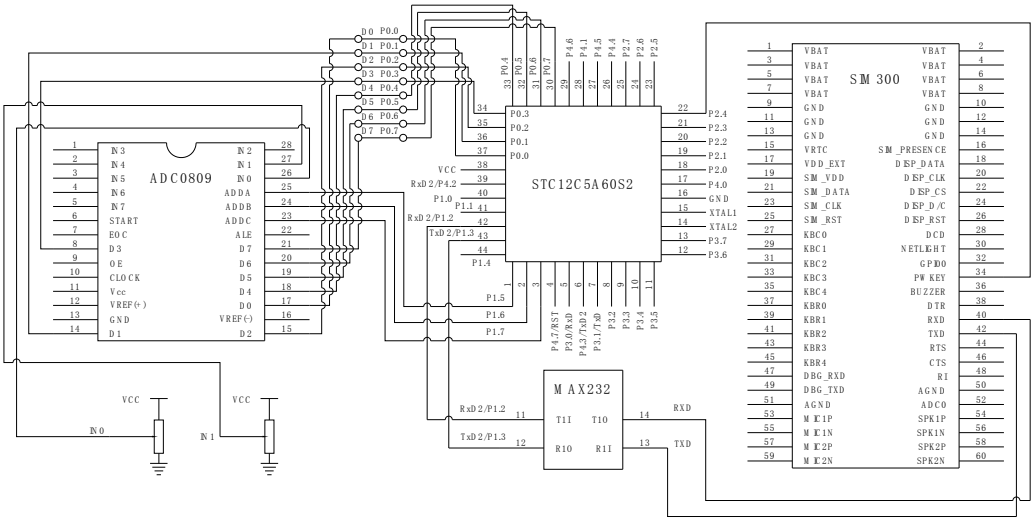

Fig. 2 Circuit diagram

As the block diagram of lower computer system based on GPRS technology shown in figure1, the signal of wave height and wave direction detected by sensors respectively is translated into analog voltage signal, then putted into the A/D converter ADC0809 for getting 8-bit digital signal, and inputted into the SCM, so the task of signal detecting and preprocessing module is over. Data is preprocessed and packaged by the SCM, and transmitted through the serial port to the GPRS communication module, but before that, SCM should finish the operation of starting the GPRS module, and initializing it [2].

3.2 Circuit Design

As the following figure 2, the circuit is designed based on the need of functions and working principles of lower computer system. About the module of detecting and preprocessing signal, wave height tilt sensor and direction senor are used to acquire the analog signal of height, direction and the cycle of wave. ADC0809 completes the timeshare analog-to-digital conversion on the 8-bit voltage signal directly [3].

Taken SCM STC12C5A60S2 as the core, data collecting and preprocessing module to control the bidirectional communication concretely include:1) the port P1.5、P1.6、P1.7 of SCM contacted with ADDA、ADDB、ADDC of ADC0809 select the physical parameters by controlling the IN ports. 2) the port P0.0～P0.7 of SCM receive digital signal from D0～D7 of ADC0809, and SCM processes the data simply. 3) to accomplish

the data bidirectional conveying successfully between P1.2、P1.3 of SCM and the SIM300 chip of GPRS communication module is completed under the control of SCM. SIM 300 chip is the main part of GPRS communication module, which can finish the bidirectional communication with wireless technology. In the circuit, MAX232 is specially used for RS-232, which offers a standard port for electrical level shifter.

3.3 Module Design

3.3.1 Signal Detecting and Preprocessing Module

For the measurement of wave height and direction, wave height tilt sensor adopts a vertical pendulum structure. Above it, direction sensor integrated with wave height tilt sensor is for getting the references of wave angle. All kinds of sensors are selected suitably to meet the need of actual ocean activities as a signal detection unit.

After the wave signal detected, data is converted to the port IN of ADC0809, the chip unit automatically converts analog voltage signal to digital signal as the following formula (1), the electric potentials from high to low respectively are : D7、D6、D5、D4、D3、D2、D1、D0，which are connected with the port P0 of SCM .

$$U = \frac{D7 \times 2^7 + D6 \times 2^6 + \cdots + D0 \times 2^0}{2^8 - 1} \times 5(V) \tag{1}$$

3.3.2 Data Collecting and Preprocessing Module

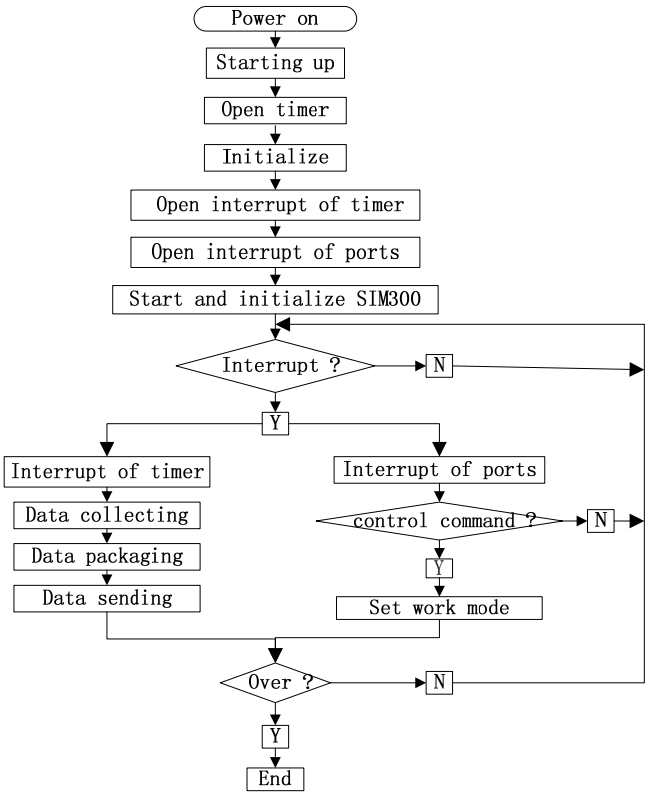

Fig. 3 Flow chart of data acquisition system

As the pivot of the whole data collecting and preprocessing module, the SCM controls the running of circuit for collecting data and completing the bidirectional communication with upper system, above figure 3 showing the flow chart of this processing [4]. Besides opening timer and interrupts, opening ports and their interrupts, opening and initializing the SIM300 chip, and setting the mode of working. Including as following:

1) After acquiring the signal data of P0.0～P0.7, those digital data is successively passed on the character string strVoltage0.

2) On the signal data of character string strVoltage0, median filter is putted. In a period of time, N numbers sampled (usually N is odd) is sorted, the median or center of which as the last value after filtering. Generally N should be determined suitably by our need and conditions, because that the computation time and quantity will be directly affected by number N as more values to sort as N grows bigger, and the size of N also determines the

amount of details that can be filtered out. Filter can make the digital signal smooth and reduce the data processing work of upper system.

3) Since the UDP (User Datagram protocol) agreement adopted in this system, the character string strVoltage0 should be defined by layer of application, packaged and carried to upper system for analysis.

4) The control commands to read for setting the mode of acquiring signal are conveyed from the upper system and received by the pattern of serial interrupt.

3.3.3 GPRS Communication Module

The SIM300 chip embedded powerful TCP/IP protocol stack mainly provides wireless high-speed transmission for voice, SMS (Short Messaging Service) and date services. After powering on, this module automatically attaches to the GPRS network and establishes the joint with the data processing center, and gets ready to send and receive data from remote terminal and controller timely. The link between the serial port RXD and TXD of SIM300 and the serial port TXD and RXD of SCM bears the work of receiving and sending data. But before that, the communication protocol of local PC has to be set, and the port numbers of PC are opened. At the same time, the IP address and port numbers of target host machine should be determined for confirming the specific network application of host machine. As the following figure 4, when the messages of remote site user's device status information are transmitted, the SCM control SIM300 chip by sending AT commands. When the upper system sends messages to control lower computer system, this terminal can directly send messages under the control of PC [5] [6]. The SCM can decompose messages as soon as getting the commands from upper system.

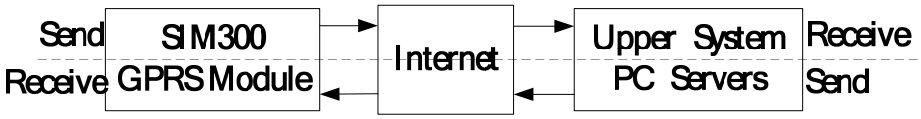

Fig. 4 Block diagram of GPRS communication module

4. Conclusions

This design and research for lower computer system of wave buoy based on GPRS wireless technology in the field of ocean wave buoy applies to the bidirectional communication for data transmission. There are some advantages including reasonable cost, high transmission speed, high speed of service network, permanent online, supporting the TCP/IP protocol, and full integration into internet. It is suitable for applications, such as intermittent sending and connection, low flow, the frequent need for data transmission, for which not only reduces the cost of building receiver, but also saves some procedures for maintaining and improves stability and reliability of the whole system. But inevitably, some shortcomings, such as measurement accuracy and security factors in the procedure of data transmission without consideration, will bring many unexpected problems and should be improved actively.

References

[1] Y. G Tang and J. P Wang. Model SZF wave Buoy System, *Ocean Technology*, Vol. 27, No. 2, pp. 31-33, 2008.

[2] P. J Li and J. Shen, MCU Connected to Internet Through GPRS, *Microelectronics and Computer*, Vol. 23, No. 3, pp. 34-39, 2006.

[3] L. H Wu and L. Li. Design and Development of Remote Ecg Monitoring System Based on Sim300, *Journal of Harbin University of Science and Technology*, Vol. 15, No. 1, pp. 113-115, 2010.

[4] Y. T Chen and J. Q Yang. Design and Implementation of a SMS Transmission System Based on SIM300, *Computer Engineering &Science*, Vol. 30, No. 3, 156-158, 2008.

[5] C. X Xie and H. Zhang. Development of SMS terminal based on GSM/GPRS, *Computer Engineering and Design*, Vol. 28, No. 7, pp. 1680-1682, 2007.

[6] X. G Che, Hamalainen, S, Ryynanen, J and Moisio, Martti. GPRS Radio Network Performance Simulation and Optimization with Dynamic Simulator. *Proc of the Int'l Conf on Communication Technology*, Vol. 2, pp. 935-939, 2003.

International Journal of Comprehensive Engineering
Part C, 2(4), 346-351, 2013
Doi: 10.14270/IJCE2013.2.4.c346
Regular paper

ISSN 2186-2680
e-ISSN 2186-2656
www.iace-journal.org

Research on Balance Pressure Proportioning Set for Oil Tanker Based on Axiomatic Design

Can Wang [1], Hongwu Chen [1,#], Jia Huan [2], Ming Li [3]

[1]College of Engineering & Technology, Shanghai Ocean University, Shanghai 201306, China
[2]School of Electrical Engineering, Shandong University, Jinan 250061, China
[3]School of Petroleum Engineering, China University of Petroleum(Beijing), Beijing 102249, China

[#]Corresponding author: hwchen@shou.edu.cn; Tel.: +86-21-61900817; Fax: +86-21-61900805

Abstract: Axiomatic Design is one of the most widely used design method at present, and it is a structural design method. This design method is highly valued by designers. Axiomatic Design can form a rational design scheme and provide criteria and assessment methods. There are two basic axioms: independence axiom and information axiom. With the rapid development of shipping, ship security has becomes the focus of concern. Oil tanker safety is even more important. Balance pressure proportioning set is one of the most popular products in its class. It's advantages are high reliability, high flow range, big foam liquid storage capacity. These advantages make it a ideal fire-fighting equipment for oil tanker. Based on Axiomatic Design, it is given that a rational design method for balance pressure proportioning set. This activity will have a profound impact on fire-fighting equipment research.

Keywords: Axiomatic Design, Oil Tanker, Balance Pressure Proportioning Set.

Received: May 25,2012 / Accepted: Aug. 12,2013 / Published: Nov. 15,2013

1. Introduction

Axiomatic Design was put forward for the first time by Nam Pyo Suh in the 1970s, when he worked at Massachusetts Institute of Technology. Axiomatic design theory was formally introduced in the book The Principle of Design in1990 [1-2]. Axiomatic design is one of the axiomatic design methods, which have wide range of applications. Experts and scholars at home and abroad have studied this theory, and achieved some results [3]. But it is still in the primary stage [4].

With the rapid economic development, shipping as a main tool for marine traffic is playing a more and more important role. The function of oil tanker in oil transportation is vital. So, the security issues were paid more attention. In recent years, oil tanker fire accident occurred one after another, causing a series of tragic accidents. For its specificity, oil tanker navigates far away from the land, and it is difficult to get assistance. Fire spreads fast, and oil tanker is prone to explosion, even both ship and oil are damaged, bringing huge economic losses and ecological disaster.

Foam fire extinguishing system is appropriate for controlling and extinguishing oil fires. The advantages are efficient and economic. In addition, water damage is small. These advantages make Foam fire extinguishing system apply to fire extinguishing on oil tanker.

The core part of foam fire extinguishing system is proportioning unit, and its reliability and performance have has a big effect on the performance of the entire system. Pressure proportioning set is most advanced

product of its kind. Its advantages are high reliability, high flow range, big foam liquid storage capacity. So it is the best choice. This article will present the design rationality of Balance Pressure Proportioning Set Based on Axiomatic Design. This could play a guiding role on practical design of fire-fighting equipment.

2. Fundamental Concepts of Axiomatic Design

2.1 Concepts of Field

In design activities, "What we want to achieve" usually interacts with "How we choose to achieve it". Fig1 shows that the design world consists of four distinct domains, such as the "consumer domain", "functional domains", "physical domain" and "process domain". The elements of the four domains are "Customer

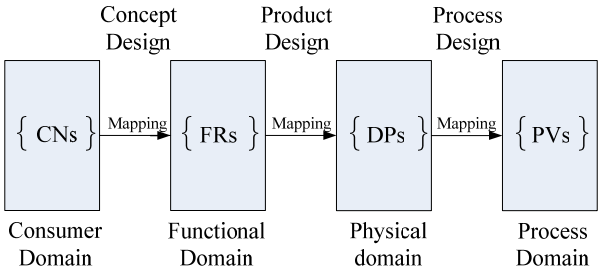

Fig. 1 Four domains of the design world

Attributes", "Functional Requirements", "Design Parameters", "Process Variables" respectively. The design process involves three mappings between adjacent domains [2] showed in Fig 1.

Axiomatic design is a kind of structural design method, and the top-down design process. The high level decision-making will affect the low level design solution condition directly [5]. Each domain is defined by a characteristic vector which could be decomposed by zigzagging between the domains, as shown in Fig2. The mapping process fully reflects the close relationship fully between adjacent fields.

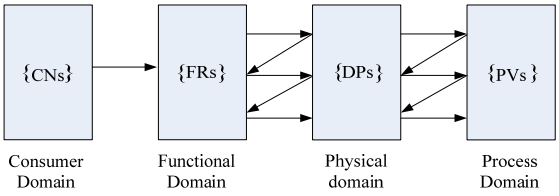

Fig. 2 The mapping process

2.2 Basic Principles of Axiomatic Design

2.2.1 Independent axiom

Axiom 1. Independent axiom: Maintain the independence of functional requirement [2].

We must note that the independence required by Independent Axiom is between designed function not physical structures.

Axiomatic Design analyzes product function structure by using Independent Axiom. The relationship between two function requirements is represented indirectly by using the relationship between function requirement and design parameter. The mapping relationship between them is as follows:

$$\{FRs\} = [A]\{DPs\} \tag{1}$$

where $\{FRs\} = \begin{bmatrix} FR_1 \\ FR_2 \\ \vdots \\ FR_n \end{bmatrix}$, $\{DPs\} = \begin{bmatrix} DP_1 \\ DP_2 \\ \vdots \\ DP_n \end{bmatrix}$ and design matrix $[A] = \begin{bmatrix} A_{1,1} & A_{1,2} & \cdots & A_{1,n} \\ A_{2,1} & A_{2,2} & \cdots & A_{2,n} \\ \vdots & \vdots & & \vdots \\ A_{n,1} & A_{n,2} & \cdots & A_{n,n} \end{bmatrix}$, where $a_{i,j} = \dfrac{\partial FR_i}{\partial DP_j}$. For a

linear design, $A_{i,j}$ is the constant; For a nonlinear design, $A_{i,j}$ is a function of DPs. The design matrix has two kind of special situations, diagonal matrix and triangular matrix, as shown in the Fig 3. If one design matrix is neither diagonal matrix nor triangular matrix, now we get a coupled design and this lead to a failed design. But in design activities, it is very difficult to get an uncoupled design, so we make sure that the design matrix is triangular matrix, i.e. the design is uncouples design [6].

$$\begin{bmatrix} X & 0 & 0 \\ 0 & X & 0 \\ 0 & 0 & X \end{bmatrix} \qquad \begin{bmatrix} X & 0 & 0 \\ X & X & 0 \\ X & X & X \end{bmatrix}$$

Uncoupled Decoupled

X – significant dependence

Fig. 3 Special situations of design matrix

2.2.2 Information axiom

Axiom 2. Information axiom: Minimize the information content [2].

The information axiom states that all designs that satisfy the Independence Axiom, the design that has the smallest information content is the best design. Information is defined in terms of the information content, I_i, that is the probability of satisfying the given FRs. I_i is defined as follows:

$$I_i = -\log_2 P_i = \log_2 \frac{1}{P_i} \tag{2}$$

If the system has m PFs, then the total information content I_{sys} is defined as follows:

$$I_{sys} = -\sum_{i=1}^{m} \log_2 P_i \tag{3}$$

where P_i is defined as $P_i = \frac{Common\ \ range}{System\ \ range}$, as showed in Fig 4.

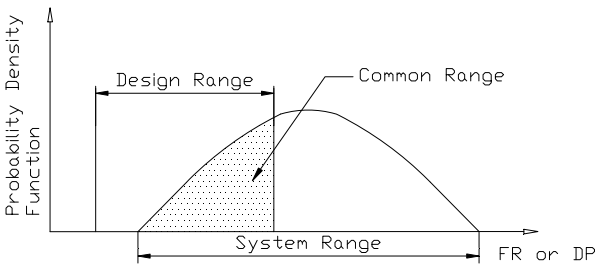

Fig. 4 Common range between design and system range

In short, Axiomatic Design theory provides a set of reasonable design ideas and methods for the designers, and it is applied at early stage of the design, which determining the most final value of most products. Axiomatic Design standardizes comprehensive analysis process of design, and guide designers make proper design decisions.

3. Application example of Axiomatic design

Now, we discuss the design of Balance Pressure Proportioning Set based on Axiomatic Design. Fig 5 states

that the Functional Requirements are divided into 3 levels. Similarly, Fig 5 states that Design parameters are also divided into 3 levels.

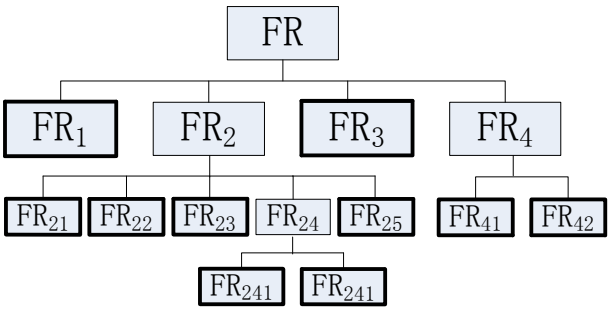

Fig. 5 Functional decomposition hierarchy diagram

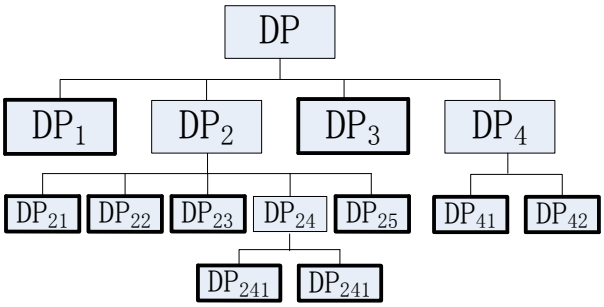

Fig. 6 Design parameters decomposition hierarchy diagram

3.1 The first level decomposition

FR_1 = High pressure fire water (0.6-1.2MPa[7]), DP_1 =Fire water pipe; FR_2 = Foam concentrate supply, DP_2 = Foam concentrate supply set; FR_3 = concentration control, DP_3 = Integration proportional regulator; FR_4 = Backflush function, DP_4 = Backflush module. Now, we get a decoupling design, and the design matrix is as the follows:

$$\begin{bmatrix} FR_1 \\ FR_2 \\ FR_3 \\ FR_4 \end{bmatrix} = \begin{bmatrix} X & 0 & 0 & 0 \\ 0 & X & 0 & 0 \\ X & X & X & 0 \\ 0 & X & 0 & X \end{bmatrix} \begin{bmatrix} DP_1 \\ DP_2 \\ DP_3 \\ DP_4 \end{bmatrix} \tag{4}$$

3.2 The Second level decomposition

3.2.1 The decomposition of FR_2

FR_{21} =Storage of foam concentrate, DP_{21} = Atmospheric pressure foam concentrate storage tank; FR_{22} =The make-and-break of foam concentrate pipeline, DP_{22}= Electric control valve; FR_{23}= Filtering foam concentrate, DP_{23} = Filter; FR_{24} = Elevating foam fluid pressure, DP_{24} = Pressure components; FR_{25} = Prevents the foam concentrate backflow, DP_{25}= Check valve. Now, we We get a decoupling design, and the design matrix is as the follows:

$$\begin{bmatrix} FR_{21} \\ FR_{22} \\ FR_{23} \\ FR_{24} \\ FR_{25} \end{bmatrix} = \begin{bmatrix} X & 0 & 0 & 0 & 0 \\ 0 & X & 0 & 0 & 0 \\ X & X & X & 0 & 0 \\ X & X & 0 & X & 0 \\ X & X & 0 & X & X \end{bmatrix} \begin{bmatrix} DP_{21} \\ DP_{22} \\ DP_{23} \\ DP_{24} \\ DP_{25} \end{bmatrix} \tag{5}$$

3.*2.2 The decomposition of* FR_4

FR_{41}= Drawing part of fire water, DP_{41} = The conduit; FR_{42} = The make-and-break of the conduit DP_{42}= Ball valve. Now, we get a decoupling design, and the design matrix is as the follows:

$$\begin{bmatrix} FR_{41} \\ FR_{42} \end{bmatrix} = \begin{bmatrix} X & 0 \\ X & X \end{bmatrix} \begin{bmatrix} DP_{41} \\ DP_{42} \end{bmatrix} \tag{6}$$

3.3 The third level decomposition

FR_{241}= Increasing foam concentrate pressure, DP_{241}= Foam concentrate pump; FR_{242}= Power supply, DP_{242}= Motor. Now, we adjust the order between design parameters and functional requirements, and we get a decoupling design, and the design matrix is as the follows:

$$\begin{bmatrix} FR_{242} \\ FR_{241} \end{bmatrix} = \begin{bmatrix} X & 0 \\ X & X \end{bmatrix} \begin{bmatrix} DP_{242} \\ DP_{241} \end{bmatrix} \tag{8}$$

All above is the functional decomposition process of Balance Pressure Proportioning Set based on Axiomatic Design. And we get a decoupled design. Table 1 shows the relational table between design parameters and functional requirements.

Table 1 The relational table between design parameters and functional requirements

Items	DP_1	DP_{21}	DP_{22}	DP_{23}	DP_{242}	DP_{241}	DP_{25}	DP_3	DP_{41}	DP_{42}
FR_1	*X*	*0*	*0*	*0*	*0*	*0*	*0*	*0*	*0*	*0*
FR_{21}	*0*	*X*	*0*	*0*	*0*	*0*	*0*	*0*	*0*	*0*
FR_{22}	*0*	*0*	*X*	*0*	*0*	*0*	*0*	*0*	*0*	*0*
FR_{23}	*0*	*X*	*X*	*X*	*0*	*0*	*0*	*0*	*0*	*0*
FR_{242}	*0*	*0*	*0*	*0*	*X*	*0*	*0*	*0*	*0*	*0*
FR_{241}	*0*	*X*	*X*	*0*	*X*	*X*	*0*	*0*	*0*	*0*
FR_{25}	*0*	*X*	*X*	*0*	*0*	*0*	*X*	*0*	*0*	*0*
FR_3	*X*	*X*	*X*	*0*	*0*	*X*	*0*	*X*	*0*	*0*
FR_{41}	*0*	*0*	*X*	*0*	*0*	*X*	*X*	*0*	*X*	*0*
FR_{42}	*0*	*0*	*0*	*0*	*0*	*0*	*0*	*0*	*X*	*X*

4. Summary

Balance Pressure Proportioning Set is the key unit, having an big impact on the performance of the whole fire-fighting system. This article presents a kind of design method for Balance Pressure Proportioning Set on Axiomatic Design. In the design activity, the relationship between all parts ware taked into account fully, and we get a rational design. This has great guiding significance on the actual design activities.

Acknowledgements

This work was supported by National Natural Science Foundation of China (No. 51075258), Shanghai Natural Science Foundation (No. 09ZR1421800). Their supports are gratefully acknowledged.

References

[1] N. P Suh. *The principle of design*. Oxford University Press, 1990.

[2] N. P Suh. *Axiomatic Design: Advances and Applications*, Oxford University Press, 2001.

[3] K. Osman, S. Cebi and C. Kahraman. Applications of Axiomatic Design Principles:a Literature Review, Expert systems *with Applications*, Vol. 37, No. 9, 2010.

[4] S. H Song, Y. Gao and R. Q Li. The Design of Three-dimensional garage transmission system Based on the Axiomatic Design, *Journal of Sichuan Ordnance*, Vol. 32, No. 7, 2011.

[5] J. H Wu, Z. C Du and Z. Q Yao. The Development of Punching Unit for Automobile Profile Based on the Axiomatic Design, *Machine Design and manufacturing Engineering*, Vol. 31, No. 5, 2002.

[6] P Jiang, R. H Tan, R. H Zhang and S. J Lu. Structure Analysis of Valve Based on Axiomatic Design, *Computer integrated Manufacturing Systems*, Vol. 9, No. 3, 2003.

[7] GB50151-2010. *Code of design for form extinguishing system*.